

The inverse problem of Magnetocardiography

Activation time imaging with the Extended Kalman Filter and the
Unscented Kalman Filter

Der Technischen Fakultät der
Christian-Albrechts-Universität zu Kiel
zur Erlangung des akademischen Grades
Dr.-Ing.

eingereichte
Dissertation

von
Henning Ahrens
aus
Kiel

2015

Referent: Prof. Dr.-Ing. Ludger Klinkenbusch
Koreferent: Prof. Dr. med. Norbert Frey

Tag der mündlichen Prüfung: 20.09.2016

zum Druck genehmigt

Diese Arbeit ist meiner Schwester Birthe gewidmet.

Danksagungen

Diese Arbeit ist unter tatkräftiger Unterstützung zahlreicher Mitarbeiter der Arbeitsgruppe Numerische Feldberechnung des Instituts für Elektrotechnik und Informationstechnik der Christian-Albrechts-Universität zu Kiel entstanden: Ich möchte mich an dieser Stelle bedanken bei Herrn Fatih Argin für die fachliche Hilfe im Rahmen des Sonderforschungsbereichs 855 der Deutschen Forschungsgemeinschaft, bei Herrn Kai Körber und Herrn Hendrik Brüns für die Hilfe in Bezug auf schwierige Fragen in der Programmierung, bei Herrn Catalin Victor Motrescu für die Hilfe bei der kardiologischen Modellierung, bei Herrn Alwin Reinhardt für das Korrekturlesen, sowie bei der studentischen Hilfskraft Andreas Gocht für die Hilfe bei der Erstellung von Grafiken sowie auch bei der Programmierung. Nicht zuletzt gilt großer Dank Herrn Prof. Ludger Klinkenbusch für das Einbringen neuer Ideenvorschläge für meine Arbeit aber auch für die volle Unterstützung eigens entwickelter Ideen.

Zusammenfassung

In dieser Arbeit wird die Berechnung elektrischer Aktivität im Herzen aus mit Hilfe magnetokardiographischer Sensoren gemessenen Magnetfeldern und der Lösung des zugehörigen inversen Problems untersucht. Mögliche Anwendungen des Formalismus sind etwa die Lokalisierung akzessorischer Leitungsbahnen im Wolff-Parkinson-White Syndrom oder die Lokalisierung fokaler ventrikulärer Tachykardie.

In dieser Arbeit wird zur Rekonstruktion der elektrischen Aktivität des Herzens die Methode *activation time imaging* untersucht. Hierbei werden zunächst die primären Stromdipole in einem kubischen ventrikulären Gitter aus den Signalen der Sensoren berechnet. Hierfür werden Standardverfahren zur Lösung des inversen Problems verwendet, wie die Multiple Signal Classification (MUSIC) oder das Tichonov regularisierte Weighted Minimum Norm (WMN) Verfahren. Aus dem Maximum des Primärstroms einer ventrikulären Zelle kann dann die Aktivierungszeit/Depolarisierungszeit der Zelle abgeschätzt werden. Die so berechneten Aktivierungszeiten dienen als Anfangszustände für die in der Arbeit verwendeten Kalman Filter. Aufgrund der im Vergleich zur Anzahl der Quellen des Magnetfelds sehr kleinen Anzahl an Sensoren ist das inverse Problem für die primären Stromdipole stark unterbestimmt und nicht eindeutig lösbar. Die mit den Methoden MUSIC und WMN berechneten Aktivierungszeiten weichen daher stark von den tatsächlichen Aktivierungszeiten ab. Es wird daher in einem Zustandsmodell eine Prozessfunktion eingeführt, die eine zusätzliche Nebenbedingung für das inverse Problem darstellt, die Aktivierungszeiten glättet und damit zu einer Verringerung des Fehlers für die Aktivierungszeiten führt. Der mittlere Lokalisierungsfehler für akzessorische Leitungsbahnen wird dabei ebenso verringert, da er aus dem Ort des Minimums der Aktivierungszeiten berechnet werden kann. Da die verwendete Prozessfunktion sowie die Signalfunktion nichtlineare Funktionen der Aktivierungszeiten sind, werden zur Lösung des Zustandsmodells die für nichtlineare Zustandsmodelle optimierten Algorithmen EKF (Extended Kalman Filter) und UKF (Unscented Kalman Filter) verwendet.

In Kapitel 6 der Arbeit werden mit Hilfe des EKF und des UKF Aktivierungszeiten für 12 verschiedene Ausgangspunkte der Aktivität in den Ventrikeln berechnet und die Fehler über die 12 Ausgangspunkte gemittelt. Zusätzlich werden die Aktivierungszeiten berechnet für 7 Paare von Ausgangspunkten der Aktivität sowie für den Fall, dass der Aktivität der 12 einzelnen Ausgangspunkte die Aktivität eines gesunden Herzmodells überlagert wird (Fusionsmodell). Sowohl im Fall der 12 einzelnen Ausgangspunkte als auch im Fall der 7 Paare von Ausgangspunkten und im Fusionsmodell liefert der UKF eine bessere Abschätzung der tatsächlichen Aktivität als der EKF. Im Fall der 12 einzelnen Ausgangspunkte und im Fusionsmodell erhält man die beste Abschätzung der Aktivität und den kleinsten mittleren Lokalisierungsfehler für die Kombination aus Anfangszustand MUSIC und Kalman Filter UKF. Im Fall der 7 Paare von Ausgangspunkten liefert eine Abschätzung der Aktivierungszeiten mit dem Einzel-Dipol-Verfahren MUSIC jedoch größere Fehler als das Verfahren WMN.

Es wird vermutet, dass der UKF eine bessere Abschätzung der Aktivierungszeiten als der EKF liefert, da die glättende Prozessfunktion eine nichtlineare und sogar unstetige Funktion der Aktivierungszeiten ist, der EKF jedoch nur ein Verfahren erster Ordnung Taylor ist. Der UKF ist dagegen ein Verfahren dritter Ordnung.

Im Vorhinein wurden in Kapitel 5 der Arbeit verschiedene geometrische Anordnungen von Magnetokardiographie-Sensoren untersucht. Dabei wurden einzelne primäre Stromdipole im Herzen mit Hilfe des Verfahrens MUSIC lokalisiert. Für die Dipole wurden Lokalisierungsfehler berechnet für Sensor-Doppellagen auf der Vorderseite des Torsos, Sensor-Doppellagen auf der Rückseite des Torsos und gleichzeitig auf der Vorder- und Rückseite angebrachte Sensoren. Der mittlere Lokalisierungsfehler war hierbei sowohl für ein kommerzielles Magnetokardiographie-System mit 64 auf einer Kreisfläche angeordneten Sensoren als auch für eine quadratische Anordnung mit (6×6) Sensoren am kleinsten im Fall der gleichzeitig auf der Vorder- und Rückseite angebrachten Sensoren, so dass die Anordnung mit (6×6) Sensoren vorderseitig und (6×6) Sensoren rückseitig auch für oben genannte Kalman Filter Simulationen verwendet wurde.

Dass die gleichzeitige Anordnung der Sensoren auf der Vorder- und Rückseite des Torsos die kleinsten Lokalisierungsfehler liefert, wurde darüber hinaus anhand einer experimentellen Studie an herzgesunden Probanden mit einem kommerziellen Magnetokardiographie-System bestätigt.

Abstract

In this thesis the reconstruction of electrical activity in the heart with the help of noninvasive magnetic field measurements and the solution of the corresponding magnetocardiographic (MCG) inverse problem is investigated. Possible applications of the formalism are the localization of accessory pathways in Wolff-Parkinson-White syndrome or the localization of focal defects in focal ventricular tachycardia.

In order to reconstruct the electrical activity in the heart this work employs the method *activation time imaging*. In the method first the primary current dipoles distributed on a cubic ventricular grid with a lattice constant of 1.5 mm are calculated from the measured magnetocardiographic signal using standard algorithms for the inverse problem, namely the Tikhonov regularized Weighted Minimum Norm (WMN) or the Multiple Signal Classification (MUSIC). In the next step the depolarization/activation time of the cubic ventricular cell can be estimated from the maximum of the primary current in the cell. These WMN- and MUSIC-generated activation times act as initial states for the Kalman Filters investigated in this work. Because the number of magnetocardiographic sensors is several orders smaller than the number of primary current dipoles in the heart, the inverse problem for the primary current dipoles doesn't have a unique solution and is highly ill-posed. Consequently, there is a large error between the true simulated activation times and the WMN- and MUSIC-generated activation times. In order to reduce the error between the activation times, in a state-space model a process function is introduced that smoothes the activation time map and states an additional constraint for the activation times. Because the location of the accessory pathway can be found from the minimum of the activation time map, also the localization error for accessory pathways is reduced by the application of the process function. Because both the process function and the MCG signal function are nonlinear and even nonsmooth functions of the activation times, the Extended Kalman Filter (EKF) and the Unscented Kalman Filter (UKF), that are optimized for nonlinear state-space models, are applied to the WMN- and MUSIC-generated initial states.

In the central chapter 6 the EKF and the UKF are used for the calculation of the activation times for 12 single pacer locations uniformly distributed over the ventricles, for 7 pairs of pacers in the ventricles and for 12 fusion beats, that consist of the activation times of the 12 single pacer locations superimposed by the activation times of a healthy heart model. The localization errors and relative errors for the activation times are averaged over all tested pacer locations. The result is that in all the three cases, single pacers, pairs of pacers and fusion beats, the UKF provides a better estimation for the true activation times than the EKF. Both in the cases of the single pacers and the fusion beats the combination of initial state MUSIC with the Kalman Filter UKF results in the best activation times. In contrast in case of the 7 pairs of pacers the single dipole technique MUSIC results in larger errors than the initial state WMN.

The reason for this result might be the fact, that the process function and MCG signal function are nonlinear and even nonsmooth functions of the activation times,

and the EKF is just an algorithm of *1st* order Taylor series, while the UKF estimates the mean and covariance of the activation times to the *3rd* order Taylor series.

Prior to the Kalman Filter investigations there have been made several investigations in chapter 5 to optimize the geometry of the MCG sensor array: several sensor arrays have been compared with respect to the localization accuracy for single primary current dipoles using the technique MUSIC. Localization errors have been calculated for the case of double layer arrays on the anterior side of the torso, double layer arrays on the posterior side of the torso and an array with sensors both on the anterior side and on the posterior side of the torso. The averaged localization error was smallest in case of the sensor array with sensors both on the anterior side and on the posterior side of the torso. This has been validated both for a commercial MCG system with 64 sensors uniformly distributed on the area of a circle and for a square (6×6) sensor array. Consequently, an array with (6×6) sensors on the anterior side of the torso and (6×6) sensors on the posterior side of the torso has been used for the Kalman Filter calculations in chapter 6.

Additionally, it has been validated in a clinical study with heart-healthy subjects and a commercial circular MCG system, that the sensor array with sensors placed both on the anterior side of the torso and on the posterior side of the torso results in the smallest localization errors for single primary current dipoles.

Contents

Abbreviations	iii
Symbols	iii
1 Introduction	3
1.1 Motivation and medical applications	3
1.2 Non-uniqueness of the inverse problem and imaging approaches for ECG/MCG	5
1.3 Structure of the Thesis	6
2 Biological and medical foundations	9
2.1 Anatomy of the heart	9
2.2 Electrophysiology of the heart	9
2.3 Muscle fiber directions in the heart	12
3 Heart and torso model	15
3.1 Anatomical model	15
3.2 Cellular automaton model	16
4 Forward problem of Magnetocardiography	21
4.1 Bidomain model	21
4.2 From primary current dipoles to MCG signal	23
4.3 From activation times to primary current dipoles	26
4.4 The MCG signal function $\mathbf{h}(\mathbf{x})$ of the activation times	28
5 Investigated geometries of the MCG sensor arrays	31
5.1 MCG system CS-MAG of Biomagnetik Park	31
5.1.1 Theoretical model investigations	31
5.1.2 Comparison with experimental results	42
5.2 (6×6) -array simulations	54
6 Inverse problem of Magnetocardiography	59
6.1 Generation of initial states	59
6.1.1 Weighted Minimum Norm (WMN)	60
6.1.2 Multiple Signal Classification (MUSIC)	63
6.1.3 WMN-MUSIC hybrid technique	65
6.1.4 Comparison of the reconstructed activation times for single pacers	67
6.1.5 Comparison of the reconstructed activation times for 2 pacers	72

6.2	Kalman Filters	79
6.2.1	Nonlinear state-space model	79
6.2.2	Extended Kalman Filter (EKF)	79
6.2.3	Unscented Kalman Filter (UKF)	80
6.2.4	Results: Comparison of EKF and UKF for single pacers	82
6.2.5	Results: Comparison of EKF and UKF for 2 pacers	90
6.3	Healthy heart and fusion beats	93
6.3.1	Healthy heart depolarization times	93
6.3.2	Definition of a fusion beat	93
6.3.3	Calculation of the initial states for the fusion beats	94
6.3.4	Results: Comparison of EKF and UKF for fusion beats	96
7	Discussion and outlook	105
A	Noise simulation	107
B	Smoothing the WMN activation time maps	109
C	Kalman Filter parameter tests	111

Abbreviations

2D	2-dimensional
3D	3-dimensional
AP	Action Potential
AV node	AtrioVentricular node
BLW-AP	pacer locations Basal-Left-Wall and Apical-Posterior
BLW	pacer location Basal-Left-Wall
BRW	pacer location Basal-Right-Wall
CS-MAG	Magnetocardiography system of the company Biomagnetik Park [1]
CT	Computed Tomography
ECG	Electrocardiography
EKF	Extended Kalman Filter
EM	Expectation-Maximization
E	Excited state in the cellular automaton model
FEM	Finite Element Method
MCG	Magnetocardiography
MRI	Magnetic Resonance Imaging
MUSIC	Multiple Signal Classification
R	Resting state in the cellular automaton model
SA node	SinoAtrial node or Sinus node
SNR	Signal to Noise Ratio
SQUID	Superconducting QUantum Interference Device
SVD	Singular Value Decomposition
TSVD	Truncated Singular Value Decomposition
UKF	Unscented Kalman Filter
WMN	Weighted Minimum Norm
WPW syndrome	Wolff-Parkinson-White syndrome
W	Wavefront state in the cellular automaton model
fMCG	fetal Magnetocardiography

More abbreviations for the pacer locations (BLW, BRW, etc.) can be found in figure 6.1.

Symbols

\vec{B}	Magnetic field
D	Distance between the layers in a double layer sensor array
\vec{E}	Electric field

\vec{E}_{ext}	Extracellular electric field
\vec{E}_{int}	Intracellular electric field
\mathbf{F}_k	Jacobi matrix of \mathbf{f} for the k -th EKF iteration step
\mathbf{H}_k	Jacobi matrix of \mathbf{h} for the k -th EKF iteration step
$\mathbf{H}(\lambda)$	WMN kernel matrix for the regularization parameter λ
\mathbf{I}	Unity matrix
$\hat{\mathbf{J}}$	WMN solution for the primary current dipoles $\hat{\mathbf{J}} = (\hat{\mathbf{J}}_p(t_1), \dots, \hat{\mathbf{J}}_p(t_N))$
$\mathbf{J}_p(t)$	$(3n \times 1)$ vector including the $3n$ components of all primary current dipoles at time t
\mathbf{K}_k	Kalman gain matrix for the k -th iteration step (definitions different for EKF and UKF)
LE	Localization Error (definition corresponding to context)
\overline{LE}	Localization Error averaged over several pacer locations in the heart
\mathbf{L}_i	$(m \times 3)$ leadfield matrix corresponding to the i -th primary current dipole
\mathbf{L}	$(m \times 3n)$ leadfield matrix for m sensors and n primary current dipoles
$M(i)$	MUSIC amplitude for the i -th cubic ventricular cell
N	Number of time instants in the data time series t_1, \dots, t_N
$\partial\Omega$	Boundary of the torso volume
Ω	Torso volume
\mathbf{P}_k	Error covariance matrix $\mathbf{P}_k = \langle (\mathbf{x}_k - \mathbf{x}_{true})(\mathbf{x}_k - \mathbf{x}_{true})^T \rangle$ for the k -th iteration step
\mathbf{P}^\perp	Orthogonal projection matrix of the MUSIC method
\mathbf{Q}	Process noise covariance matrix
RE_{signal}	Relative Error of the MCG signal $RE_{signal} = \ \mathbf{h}(\mathbf{x}) - \phi\ / \ \phi\ $
RE	Relative Error for activation times $RE = \ \mathbf{x} - \mathbf{x}_{true}\ / \ \mathbf{x}_{true}\ $
\mathbf{R}	Measurement noise covariance matrix
$\boldsymbol{\chi}_k$	Sigma points of the k -th UKF iteration step
V_m	Transmembrane or action potential of a cell
$W_i^{(c)}$	UKF weighting coefficients
$W_i^{(m)}$	UKF weighting coefficients
\mathbf{W}	WMN weighting matrix
α	UKF parameter controlling the spread of the sigma points

$a(t - \tau(\vec{r}))$	Action potential of a cell at position \vec{r} and time t
$d^3\vec{r}$	Volume element for 3D integrals
$\Delta\tau_{ij}$	Difference between the activation times of the cells i and j
δt	Time interval for the calculation of the difference quotients in the Jacobi matrices
Δt	Time interval for the calculation of LE from the activation times
$\overline{\Delta t}$	Initial time interval in the MUSIC technique the data matrix is restricted to
d_{ij}	Length of the transition $i \rightarrow j$ in the cellular automaton model
\bar{d}	Maximal next neighbor distance in the process function $\mathbf{f}(\mathbf{x})$
dt	Time interval of the action potential upstroke
d	Edge length of a cubic ventricular cell
\mathbf{e}_i	$(3n \times 1)$ unit vector parallel to i -th axis
ε	Smoothing parameter in the process function $\mathbf{f}(\mathbf{x})$
$\varphi_{B,i}(t)$	Magnetic flux through the area of the i -th MCG sensor
$\varphi(t)$	$(m \times 1)$ MCG signal vector at time t
ϕ	$(m \cdot N \times 1)$ MCG data vector $\phi = (\varphi(t_1)^T, \dots, \varphi(t_N)^T)^T$
Φ	$(m \times N)$ MCG data matrix $\Phi = (\varphi(t_1), \dots, \varphi(t_N))$
φ_{ext}	Extracellular electric potential
φ_{int}	Intracellular electric potential
$\mathbf{f}(\mathbf{x})$	Smoothing process function
$\mathbf{h}(\mathbf{x})$	$(m \cdot N \times 1)$ MCG signal function $\mathbf{h}(\mathbf{x}) = ((\mathbf{L}\mathbf{J}_p(t_1, \mathbf{x}))^T, \dots, (\mathbf{L}\mathbf{J}_p(t_N, \mathbf{x}))^T)^T$
\vec{j}_p	Primary current dipole
\vec{j}_{ext}	Extracellular current density
\vec{j}_{int}	Intracellular current density
\vec{j}_p	Primary current density
\vec{j}_V	Volume or secondary current density
\vec{j}	Total current density
κ	Condition number of the leadfield matrix $\kappa = \text{cond}(\mathbf{L})$
m	Number of MCG sensors
n	Number of primary current dipoles = number of cubic cells in the ventricles
ψ	Angle of the electric axis of the MCG signal map
ρ	Charge density

\vec{r}_k	Position of the k -th primary current dipole/cubic cell in the ventricular model
\vec{r}_{apex}	Location of the apex of the heart
$\vec{r}_{min,center}(\mathbf{x})$	Location of the center-of-mass minimum of the activation times \mathbf{x}
$\vec{r}_{min}(\mathbf{x})$	Location of the minimum of the activation times \mathbf{x}
σ_{ext}	Extracellular electrical conductivity
σ_{int}	Intracellular electrical conductivity
σ	Total electrical conductivity
$\tau(\vec{r})$	Activation/depolarization time of a cell at position \vec{r}
ϑ	Angle between the muscle fiber direction and the direction of the transition $i \rightarrow j$ in the cellular automaton model
v_{\parallel}	Excitation conduction velocity in the ventricles parallel to the muscle fibers
v_{\perp}	Excitation conduction velocity in the ventricles perpendicular to the muscle fibers
w_i	Weighting coefficient for the calculation of the magnetic flux through a sensor
\mathbf{x}	$(n \times 1)$ vector including the activation times $\tau(\vec{r}_1), \dots, \tau(\vec{r}_n)$ of the n cubic ventricular cells
\mathbf{x}_{true}	true=simulated activation times

Common notations for the symbols are vectors in 3 dimensions with arrows, vectors or matrices in higher dimensions with boldfat letters and matrices with capital letters.

Chapter 1

Introduction

1.1 Motivation and medical applications

Heart diseases are the main causes of death in the industry nations. The focus of this work is the imaging of the electrical activity of the heart with Magnetocardiography (MCG). While in Electrocardiography (ECG) the electric potential at the body surface is measured with electrodes on the skin, in MCG the magnetic field of the heart currents is measured contactless with magnetic field sensors. One advantage of MCG over ECG is that the primary currents flowing in the heart have a direct contribution to the MCG signal while in ECG only the secondary currents propagating through the torso can be measured directly. Therefore the ECG signal on the posterior side of the body is stronger reduced by the low conductivity of the lungs than the MCG signal. Furthermore, because of an insulating fat layer around the fetus, this feature also motivates the application of MCG in the diagnosis of the fetal heart (fMCG).

Several types of cardiac arrhythmia are caused by focal abnormalities in the electrical conduction system of the heart. Patients with focal ventricular tachycardia have an abnormal fast heart beat due to a focal defect in the ventricular tissue pulsating faster than the sinus node, which in the worst case can end in life-threatening ventricular fibrillation. In Wolff-Parkinson-White (WPW) syndrome [2] accessory pathways that pathologically connect the atria with the ventricles parallel to the atrioventricular node can cause supraventricular¹ tachycardia (figure 1.1). The common medical therapy is the invasive removal of the accessory pathway with a catheter ablation (figure 1.2). MCG enables a noninvasive, radiation-free and fast localization of the accessory pathways in a presurgical investigation thus it can shorten the invasive and often X-ray based localization with a mapping catheter. For the purpose of localization with MCG an inverse problem need to be solved: The reconstruction of the electrical sources, i. e. ionic currents in the heart, from the measurement with a finite number m of sensors. The inverse problem of MCG is a non-unique mathematical problem, which is proved in the next section.

¹While in ventricular tachycardia the fast heart beat originates in a defect in the ventricular tissue, in supraventricular tachycardia it originates from the atrioventricular node or atrioventricular ring.

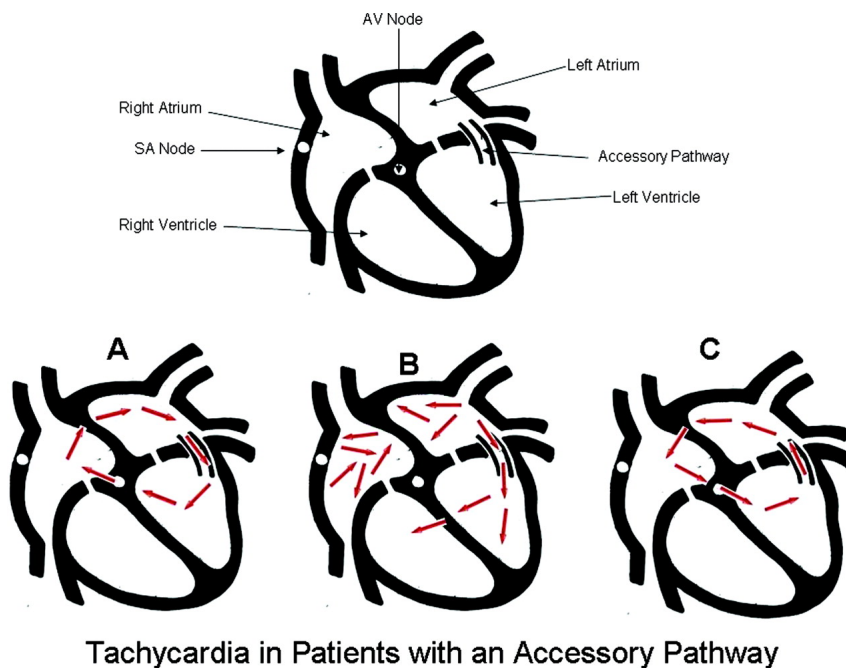


Figure 1.1: Accessory pathway causing 3 different types of tachycardia in Wolff-Parkinson-White syndrome. A: AV reentrant tachycardia (backward type), B: patient with accessory pathway *and* atrial fibrillation, C: AV reentrant tachycardia (forward type) (red arrows: movement of the depolarization wavefront) [3].

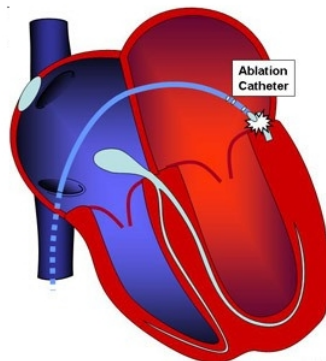


Figure 1.2: Transseptal catheter ablation of an accessory pathway in Wolff-Parkinson-White syndrome [4].

1.2 Non-uniqueness of the inverse problem and imaging approaches for ECG/MCG

Consider a finite number m of sensors. The number n of primary current dipoles, representing the ionic currents in the heart, can always be chosen to be greater than $n = (m + 1)/3$. By means of the superposition principle the signal vector at time t can be written as a system of linear equations

$$\boldsymbol{\varphi}(t) = \mathbf{L}\mathbf{J}_p(t) \quad (1.1)$$

with the $(m \times 3n)$ leadfield matrix \mathbf{L} where the $(3n \times 1)$ -vector

$$\mathbf{J}_p(t) = (\vec{j}_p(\vec{r}_1, t), \dots, \vec{j}_p(\vec{r}_n, t))^T \quad (1.2)$$

includes the components of all primary current dipoles. The system of linear equations 1.1, with $n \geq (m + 1)/3$ as described above, has more columns than rows, so a unique solution is not possible.

The inherent non-uniqueness of the inverse problem can produce large localization errors. A reduction of the localization error can be achieved by introducing additional information about the source configuration and thereby reducing the degrees of freedom of the current sources. The first information to be included should be the patient specific geometry of the body surface, heart, lungs and possibly other organs. In medical practice this patient specific anatomy is typically provided by Computed Tomography (CT) or Magnetic Resonance Imaging (MRI).

For the purpose of the solution of the inverse problem in this work the depolarization/activation times of the heart muscle cells are calculated on a 3D model of the ventricular myocardium which is called activation time imaging. Then in the framework of WPW syndrome the location of the accessory pathway can be determined as the site of earliest myocardial activation. Activation time imaging includes information of the cellular action potential during depolarization: the time a cell needs to depolarize and the slope of the action potential during depolarization which is sufficient to calculate the ionic primary currents in the depolarization wavefront. One advantage of activation time imaging is the reduction of the number of source parameters: Consider a model with n dipoles in the heart and a data time series with N time instants. Then the total number of dipole components in current dipole imaging would be $3n \cdot N$ ($3n$ at every single time instant) while the total number of activation times would be n .

Although the number of sources can be further reduced if the activation is restricted to the epicardial and endocardial surfaces, this work employs a 3D heart model because pathological defects, e. g. ectopic foci in ventricular tachycardia, can also be located in the transmural midmyocardial regions. For 2D epicardial source models it has been shown [5] that activation time imaging is more stable with respect to measurement noise than the imaging of the transmembrane potential. For this reason the imaging of the transmembrane potential will not be investigated in

this work. Although the 2D wavefront-based imaging of [6] is another improvement of the 2D transmembrane potential imaging on the epicardial surface, it will not be investigated in this work too, because of the above mentioned problem with 2D source models. An experimental validation of activation time imaging was reported in [7] using invasive epicardial electrograms and ECG for the noninvasive investigations.

In WPW syndrome it is also possible to localize the accessory pathway with a single dipole model if the ECG/MCG data is restricted to the delta wave which provides an average localization error of $\sim 1\text{ cm}$ [2]. A simulation study using the Extended Kalman Filter (EKF) for the reconstruction of activation times on a 3D myocardium shows an average localization error of about $\sim 3\text{ mm}$ [8] which is smaller than the single dipole localization result. The simulation study employs a nonlinear state-space model that includes temporal information as an additional source constraint: the smoothness of the activation time map. The EKF uses a 1st order Taylor series approximation of the nonlinear state-space model. The Unscented Kalman Filter (UKF) estimates the mean and covariance of the activation time state-vector to the 3rd order Taylor series [9]. In fact some applications have shown that due to the higher order the UKF is superior to the EKF in the solution of highly nonlinear state-space models [10]. Because the state-space model used in the simulation studies [8] is highly nonlinear, a regular linear Kalman Filter approach is not possible, so this work investigates and compares the use of the EKF and the UKF for the solution of the nonlinear state-space model of activation time imaging.

1.3 Structure of the Thesis

In this section the structure of the contents of the different chapters in this thesis will be summarized. The following chapter 2 explains the biological and medical basics of the human heart: anatomical and electrophysiological details of the human heart, e.g. the muscle fiber directions or the electrical conduction system of the heart, are shortly summarized from the literature.

In chapter 3 the anatomical and electrophysiological information of chapter 2 is used to develop simplified models for the electrical conductivities of the torso tissues, the propagation of electrical activation in the heart (cellular automaton model) and the muscle fiber directions in the heart that are used for the simulations of the activation times in this work.

The chapter 4 explains how the MCG signal is calculated by the solution of the forward problem. The MCG forward problem in this work includes the calculation of the primary currents from the activation times in the ventricles, the solution of the volume conduction problem in the bidomain model and finally the calculation of the magnetic flux through the MCG sensors via the Biot-Savart law. The final achievement of the chapter 4 is the MCG signal as a function of the activation times in the heart.

In chapter 5 some investigations concerning the geometrical positions of the MCG sensors are made in order to find out the best sensor positions for a fixed number of sensors. Chapter 5 also includes some applications of MCG sensor arrays to experimental MCG measurement results.

The chapter 6 is the central chapter of this work: it presents different techniques of calculating the activation times in the heart from the measured MCG signal, i.e. the solution of the inverse problem. The algorithms of the Extended Kalman Filter (EKF) and Unscented Kalman Filter (UKF) are summarized and combined with initial state generators. The developed inverse techniques are compared for single pacemaker simulations (1 accessory pathway), double pacemaker simulations (2 accessory pathways), healthy activation times and fusion beats (accessory pathway + healthy activation times) by calculating Localization Errors (LE) for the accessory pathways and Relative Errors (RE) for the activation times.

Chapter 2

Biological and medical foundations

2.1 Anatomy of the heart

The heart is one of the most vital organs of the human body. It is a hollow organ filled with blood and its main constituent is muscular tissue also called myocardium. The function of the heart is to pump blood through the circulatory system of the entire body by rhythmic contractions. It is located in the middle of the torso underneath the sternum with its center about 1.5 cm displaced to the left side of the midsagittal plane. The weight of a typical human heart is $250 - 300\text{ g}$ [11] and its typical size is more or less the size of a human fist. The anatomy of the human heart is shown in figure 2.1. It is divided into four chambers: the right atrium, the left atrium, the right ventricle and the left ventricle. The ventricles and the atria as well as the atria and the vessels are separated by valves to ensure a blood flow in the desired direction.

In the following the circulatory system of the human body will be summarized: Deoxygenated blood from the entire body enters the right atrium through the superior and inferior vena cava. Subsequently, during the contraction of the atria, the blood flows through the tricuspid valve into the right ventricle. Afterwards the right ventricle pumps the blood through the pulmonary valve into the pulmonary circulatory system where the blood is oxygenated by the lungs. The oxygenated blood returns from the lungs through the pulmonary veins and enters the left atrium. Afterwards, during the contraction of the atria, the blood flows through the mitral valve into the left ventricle. After the contraction of the left ventricle the oxygenated blood flows into the aorta and finally into the entire body to close the systemic circulatory system. Because in the systemic circulatory system the blood flows through the entire body and the pressure in the aorta is higher than in the pulmonary artery, the left ventricular muscle is thicker than the right ventricular muscle.

2.2 Electrophysiology of the heart

Heart muscle cells are capable of generating an action potential, the electrostatic potential difference between the inside and the outside of the cell membrane. Changes of the action potential are controlled by ion channels and ion pumps in the cell

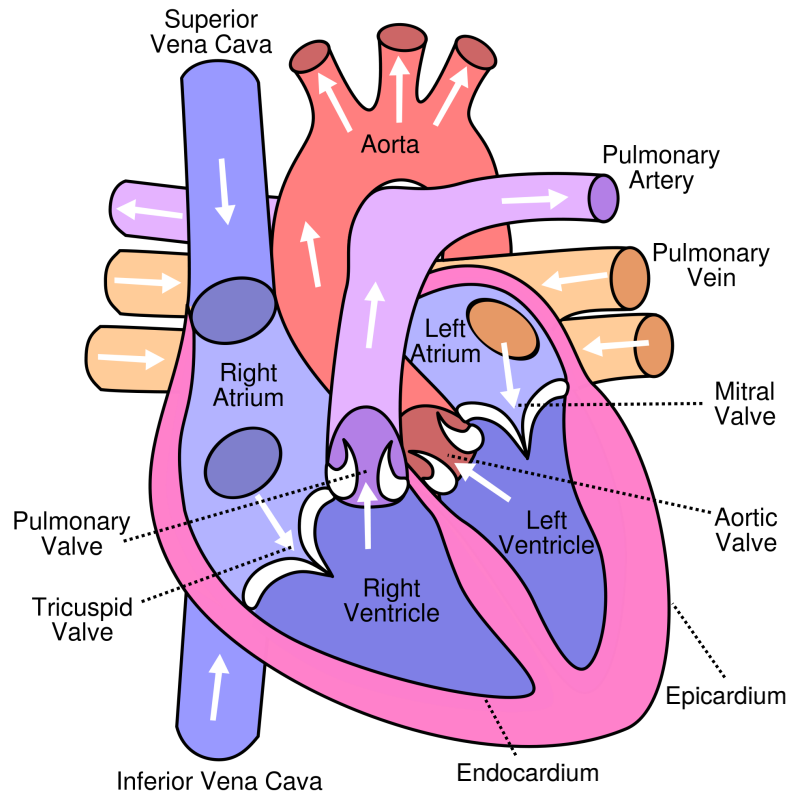


Figure 2.1: The anatomy of the human heart [12].

membrane (figure 2.2). The heart muscle cells are specialized and can be divided into two groups (figure 2.3): Cells embedded in the electrical conduction system of the heart - the Sinus (SA) node, atrioventricular (AV) node, common bundle/bundle of His, bundle branches and Purkinje fibers - have a non-constant resting potential, thus their action potential is capable of spontaneous oscillatory behavior. If the function of the SA node is destroyed or the activation is blocked somewhere, the other components of the electrical conduction system can also act as pacemakers but with lower frequencies (table 2.1). Cells inside the rest of the myocardium have a constant resting potential, thus they need a stimulus above the threshold potential to depolarize. In the healthy heart the depolarization of the cells is initiated by the SA node, then it propagates through the right and left atrium and converges in the AV node, which is the only conducting connection between the atria and the ventricles. Because the conduction velocity is reduced in the AV node, it generates a delay between the contraction of the atria and the ventricles to get an optimal blood flow. Subsequently, the depolarization propagates with higher speed through the bundle of His and the bundle branches to the Purkinje fibers. Afterwards the ventricular myocardium is depolarized by the Purkinje fibers at numerous sites in the endocardium and finally the rest of the ventricular myocardium is depolarized from endocardium to epicardium and from apex (tip of the heart) to base (valvular plane) [13] [14]. The repolarization of the ventricular muscle cells causes the relaxation of the ventricles and generates the T-wave in the ECG. The repolarization sequence of the ventricular myocardium takes place from epicardium to endocardium [15].

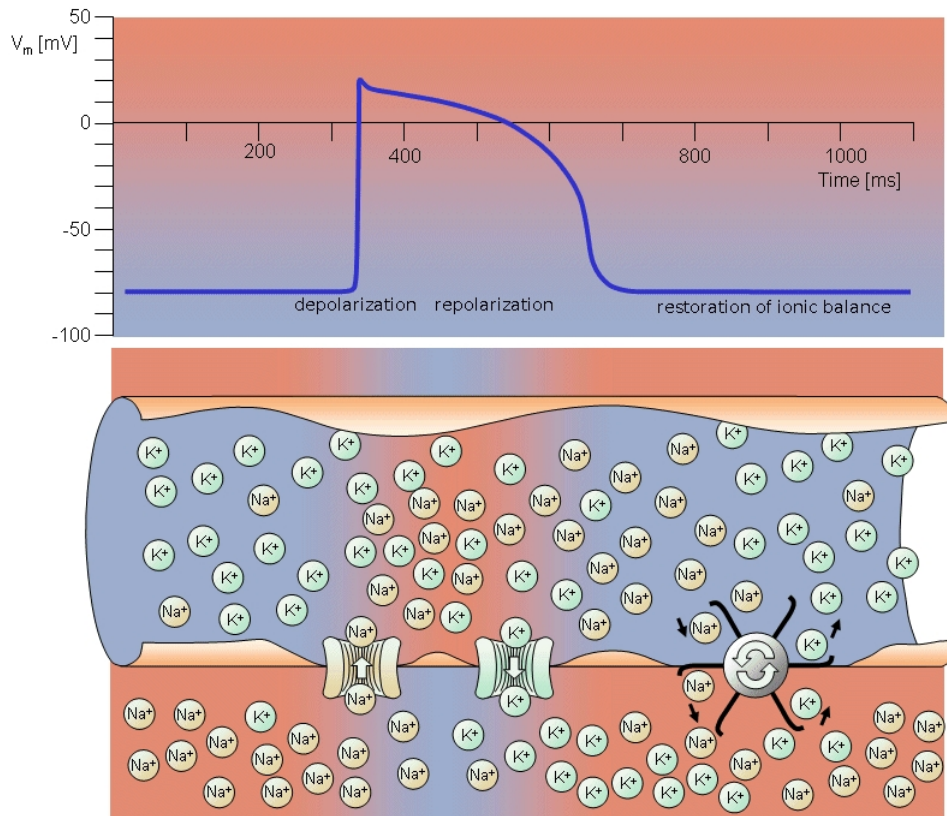


Figure 2.2: Ion channels and pumps causing depolarization and repolarization of a cardiac muscle cell [11]. V_m is the action/transmembrane potential of the cell.

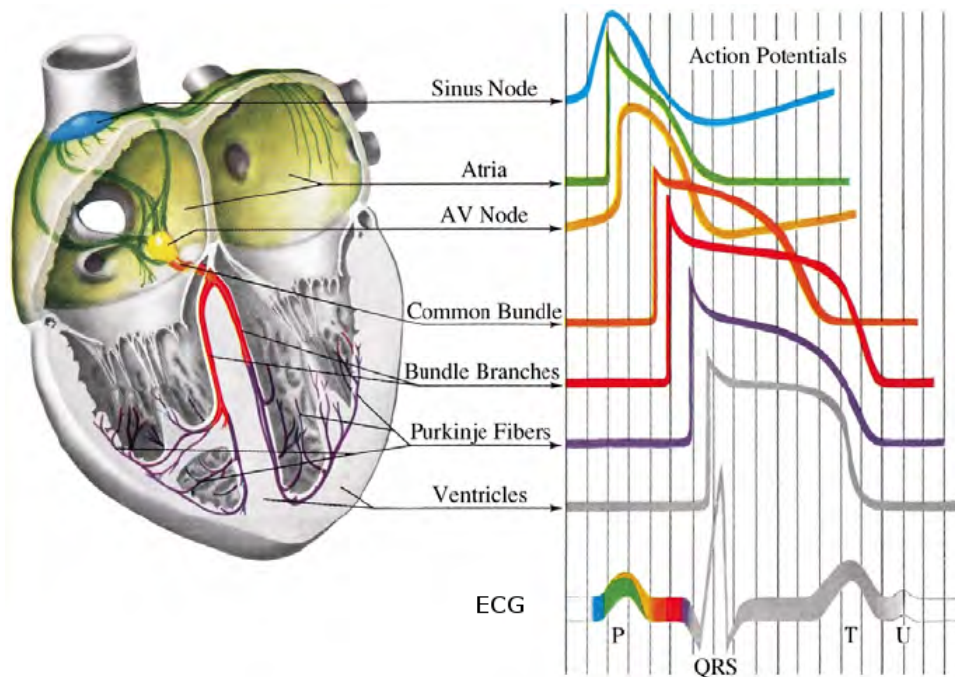


Figure 2.3: Excitation propagation in the healthy heart and heterogeneity of the action potential [16].

Location in the heart	Event	Time [ms]	Name in ECG	Conduction velocity [mm/s]	Intrinsic frequency [min^{-1}]
SA node	Start	0		50	70-80
Atrium right	Depolarization	50	P	800-1000	
Atrium left	Depolarization	85			
AV node	Arrival	50	P-Q interval	20-50	40-55
	Departure	125			
Bundle of His	activated	130		1000-1500	20-40
Bundle branches	activated	145			
Purkinje fibers	activated	150			
Endocardium	Depolarization	175	QRS	300 (\perp to fiber) 800 (\parallel to fiber)	
Left ventricle					
Right ventricle	190				
Epicardium	Depolarization	225			
Left ventricle					
Right ventricle	250				
Epicardium	Repolarization	400	T	500	
Ventricles					
Endocardium	Repolarization	600			

Table 2.1: Electrical events in the healthy heart [11].

2.3 Muscle fiber directions in the heart

The ventricular muscle fibers consist of four spirally oriented groups which are shown in figure 2.4. Three muscle fiber groups enclose both the right and the left ventricle and one additional group encloses only the left ventricle. The fiber angle, i.e. the angle between the fiber direction and the horizontal plane that is orthogonal to the ventricular axis direction (from base to apex), varies inside the ventricular wall from epicardium (-60°) to endocardium ($+60^\circ$) [17] which can clearly be seen in the histological sections of figure 2.5. The excitation conduction velocity inside the ventricular muscle is anisotropic with respect to the local muscle fiber direction ($v_{\perp} = 300 \text{ mm/s}$ perpendicular and $v_{\parallel} = 800 \text{ mm/s}$ parallel to the muscle fiber direction, table 2.1). The electrical conductivity σ of the myocardium is also anisotropic with respect to the muscle fiber directions (interstitial: 0.6 S/m parallel to the muscle fibers and 0.15 S/m perpendicular to the muscle fibers, intercellular: 0.3 S/m parallel to the muscle fibers and 0.075 S/m perpendicular to the muscle fibers [8]).

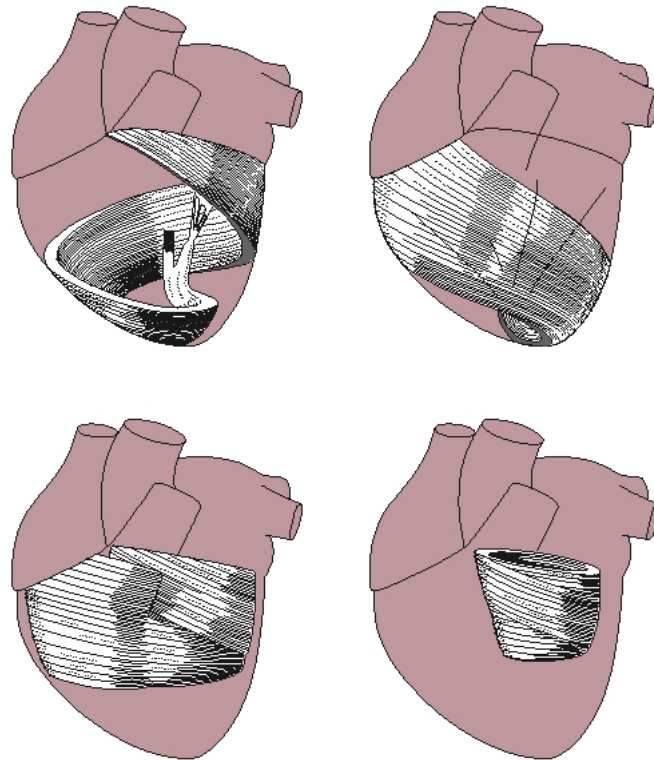


Figure 2.4: The ventricular muscle consists of four groups of muscle fibers [11].



Figure 2.5: The fiber angle between the fiber direction and the horizontal plane that is orthogonal to the ventricular axis direction (from base to apex) varies inside the ventricular wall from epicardium (-60°) to endocardium ($+60^\circ$) (photomicrographs of histological sections of the ventricle [17]).

Chapter 3

Heart and torso model

3.1 Anatomical model

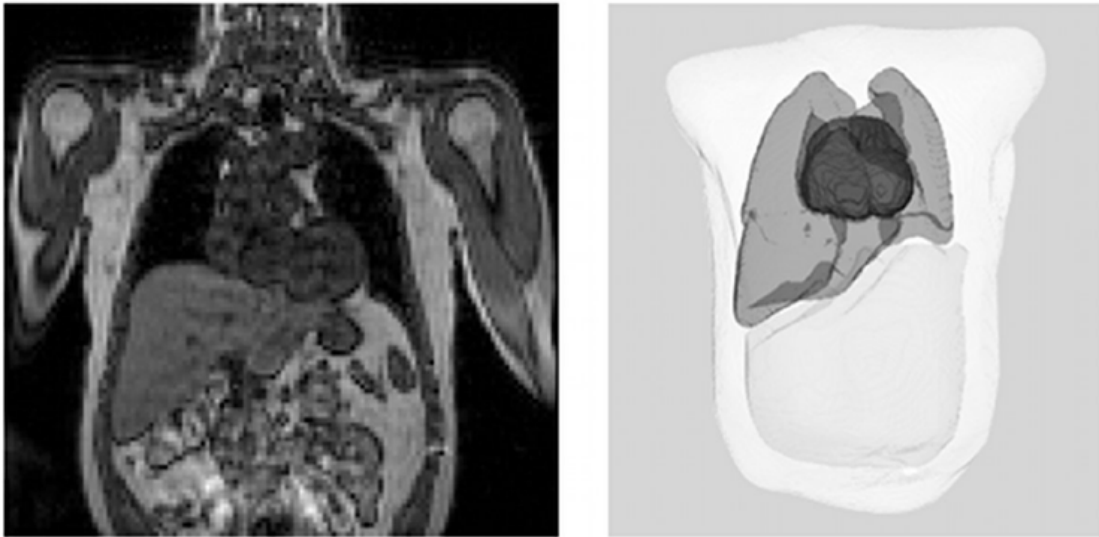


Figure 3.1: Left: MRI-Scan of the patients torso, Right: Segmentation of ventricles and lungs [18].

The ECG/MCG signals measured outside the body depend on both the primary currents flowing inside the myocardium and the volume currents flowing through the surrounding body tissues. By means of an electrical volume conduction problem the volume currents sensitively depend on the conductivities of the body tissues. Consequently, for an accurate description of the contribution of the volume currents, the patient specific geometries and conductivity values of organs, e.g. the heart and the lungs, are needed. In medical praxis the tissue geometries are typically provided by an MRI-Scan of the patients torso (figure 3.1, Left). On the right hand side of figure 3.1 the segmentation of the lungs and the ventricles is shown. In the computer simulations of this PhD thesis the geometries of the ECGSIM software [19] are used for the surfaces of the torso, the lungs and the ventricles (figure 3.2). Inside each of these regions the electrical conductivity is assumed to be homogeneous and isotropic.

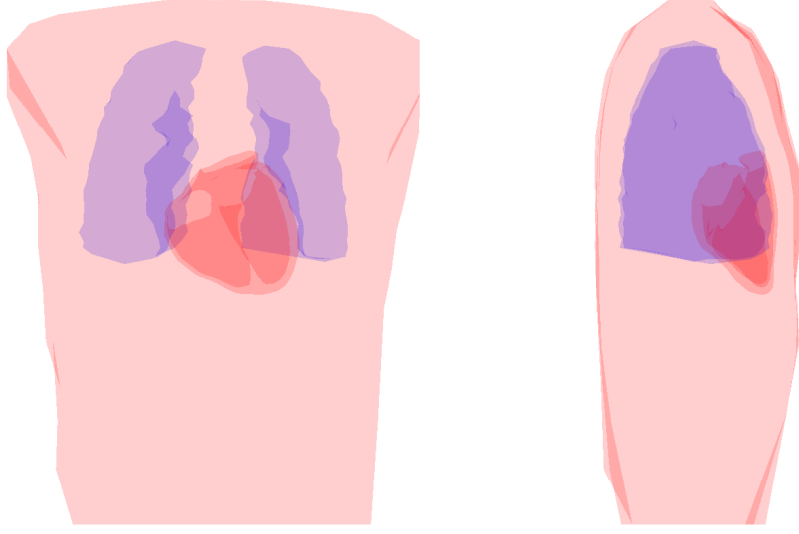


Figure 3.2: ECGSIM 1.3 geometries [19] of torso, lungs and ventricles of a normal young male (25 years, 100 kg).

3.2 Cellular automaton model

For the simulation of the depolarization time $\tau(\vec{r})$ of a cell at position \vec{r} in the ventricles in this PhD thesis a cellular automaton model [20] is used. Instead of simulating each cardiac muscle cell on a microscopic level, which can be computationally very time consuming, in the cellular automaton model each cubic cell unit (voxel) in the ventricles with an edge length of $d = 1.5 \text{ mm}$ comprises thousands of muscle cells. In this automaton approach a compromise between a low computational effort and a high simulation accuracy is reached. The cardiac muscle cells inside one voxel of the cellular automaton model are characterized by the same electrophysiological properties: the shape of the action potential, muscle fiber orientation and excitation conduction velocities with respect to the fiber orientation. The shape of the action potential is approximated by the 3 states, Resting (R), Wavefront (W) and Excited (E) (figure 3.3). The time interval dt of the action potential (AP) upstroke is of the order of $\sim 1 \text{ ms}$ [21]. In the model the upstroke was set to be $dt = 3 \text{ ms}$ in order to make the thickness of the wavefront in space bigger than the cell dimension of $d = 1.5 \text{ mm}$. The difference $\Delta\tau_{ij}$ between the activation times of two adjacent voxels i and j can be calculated as

$$\Delta\tau_{ij} = \frac{d_{ij}}{v} = \frac{d_{ij}}{\sqrt{v_{\parallel}^2 \cos^2(\vartheta) + v_{\perp}^2 \sin^2(\vartheta)}} \quad (3.1)$$

where d_{ij} is the length of the transition and ϑ is the angle between the muscle fiber direction and the direction of the transition. Starting from the voxel of initial activation (location of accessory pathway/pacer location) with the help of equation

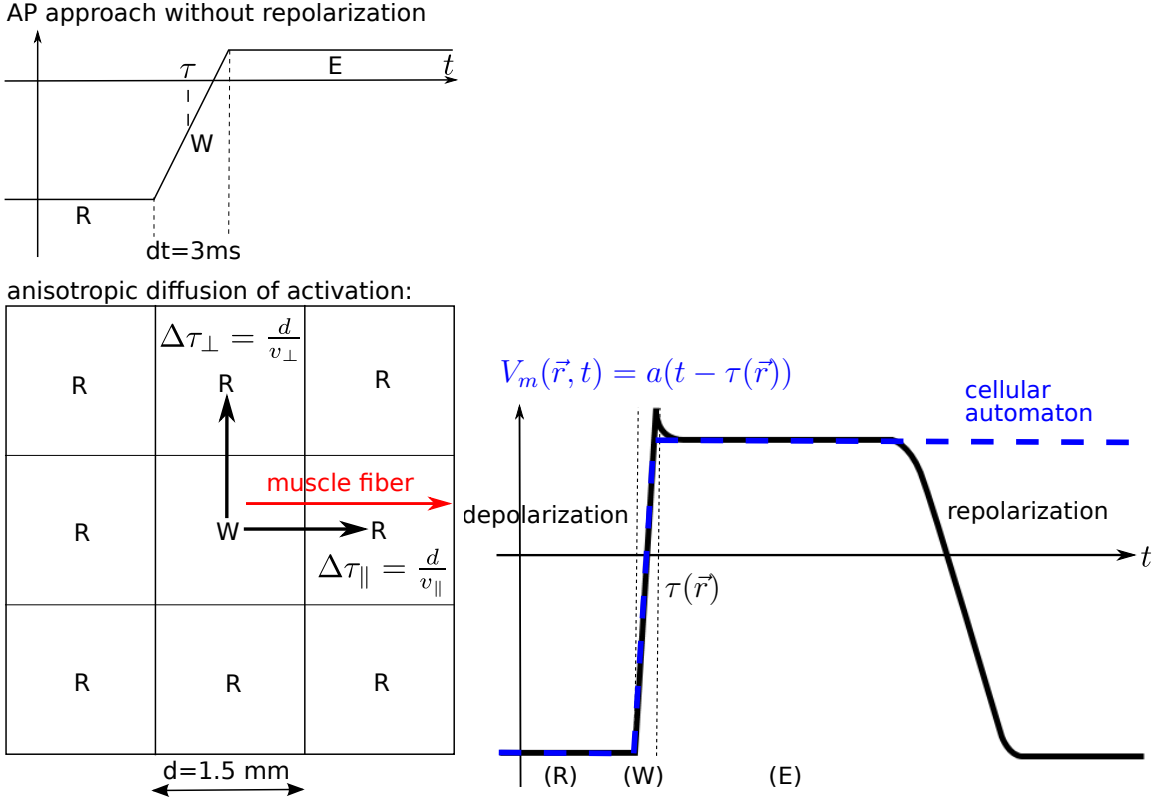


Figure 3.3: *Left*: The cellular automaton model [20] with the excitation conduction velocities v_{\parallel} and v_{\perp} , anisotropic with respect to the muscle fiber orientations. *Right*: The action potential of the cell is approximated by a simple function (blue).

(3.1) the activation times can be calculated iteratively for all voxels in the ventricles: If the voxel i is in the excitable Resting state (R) and the adjacent voxel j in the Wavefront state (W) the activation time of the voxel i can be calculated as [20]

$$\tau(\vec{r}_i) = \tau(\vec{r}_j) + \Delta\tau_{ij}. \quad (3.2)$$

The length of the transition fulfils

$$d_{ij} = \begin{cases} d, & \text{paraxial transition} \\ \sqrt{2}d, & \text{face diagonal transition} \\ \sqrt{3}d, & \text{space diagonal transition.} \end{cases} \quad (3.3)$$

The conduction velocities are selected corresponding to table 2.1 ($v_{\parallel} = 0.8 \frac{m}{s}$, $v_{\perp} = 0.3 \frac{m}{s}$). The directions of the muscle fibers in the ventricular model should be selected spirally corresponding to the anatomical information of chapter 2.3. In the cellular automaton model the myocardium is divided into layers of thickness 1.5 mm starting from the innermost epicardial layer and ending at the outermost endocardial layer (figure 3.4, [22]). The fibers are parallel to the layers and the angle to the horizontal plane varies from the innermost endocardial layer ($+60^\circ$) to the outermost epicardial layer (-60°) (figure 3.5). Because this work focuses on the simulation and inverse reconstruction of the depolarization times, the repolarization of the action potential is neglected in the model. Hence the transmural heterogeneity

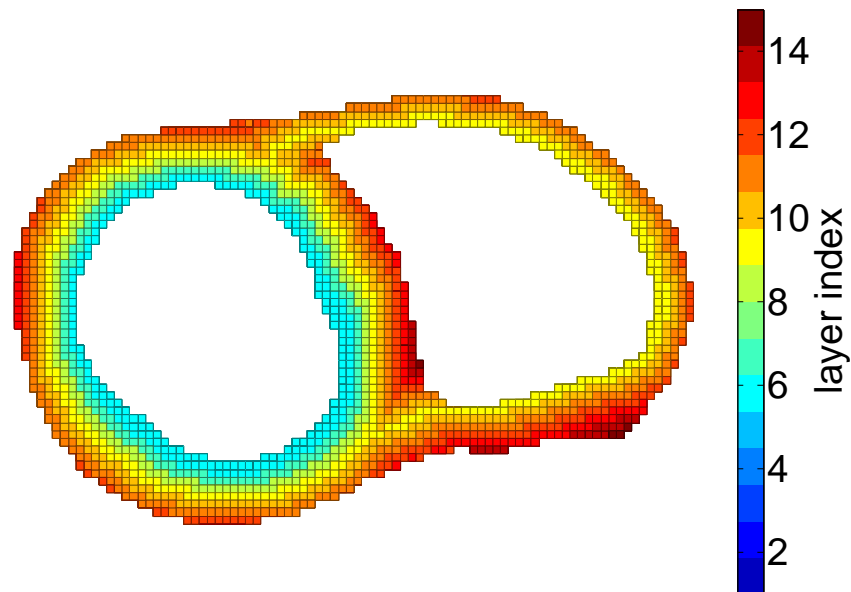


Figure 3.4: Layer based fiber model [22]. The ventricular cellular automaton model consists of $n = 53476$ cubic voxels of the dimension $1.5 \text{ mm} \times 1.5 \text{ mm} \times 1.5 \text{ mm}$.

of the action potential [23] is also neglected in the model, because it mainly affects the action potential duration and the repolarization of the cells.

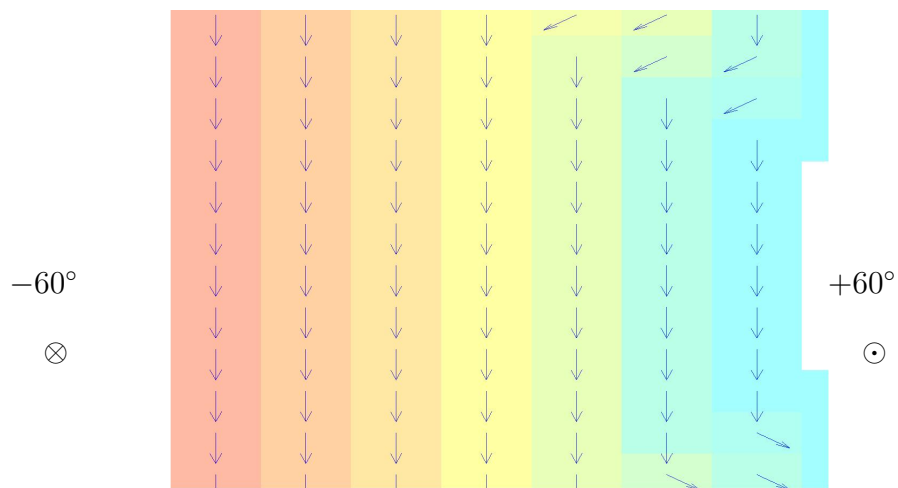


Figure 3.5: The fiber angle between the fiber direction and the horizontal plane that is orthogonal to the ventricular axis direction (from base to apex) varies inside the ventricular wall from epicardium (-60°) to endocardium ($+60^\circ$) (chapter 2.3) [17].

Chapter 4

Forward problem of Magnetocardiography

In this section it will be explained how the forward problem of magnetocardiography is solved in this work. In the forward problem of magnetocardiography the signal of the magnetic field sensors is calculated from the electrical activation of the heart. Because normally there are billions of electrically activated heart muscle cells on the microscopic cellular level, for numerical reasons macroscopic models with bigger cells comprising thousands of myocytes need to be developed (in the central chapter 6 of this work the macroscopic myocardial cell has a size of $(1.5 \text{ mm} \times 1.5 \text{ mm} \times 1.5 \text{ mm})$). In the first section of this chapter it will be explained how the primary current dipole of a macroscopic cell can be derived from the transmembrane potential in the bidomain model. The second section shows how the magnetic field at the sensor's position is calculated from the primary currents flowing in the heart and the volume currents flowing in the surrounding body tissues by means of the volume conduction problem. The third section connects the primary current dipoles with the activation/depolarization times of the macroscopic cells. The final result in the last section of this chapter is the MCG signal as a function of the activation times.

4.1 Bidomain model

The main idea of the bidomain model is to replace the system of billions of cardiac muscle cells by an averaged continuum composed of an intracellular and an extracellular space (figure 4.1). Although the ion channels in the cell membrane provide an electrical conducting connection between the inside and the outside of the cells, the conductivities of the intracellular space, σ_{int} , and the extracellular space, σ_{ext} , are different. Note that in figure 4.1 the intracellular space is only spatially extended over the inside of the *cardiac muscle cells*, while the extracellular space is spatially extended over both the cardiac and the torso tissue.

In the bidomain model the total current density \vec{j} at a point in the cardiac or torso tissue can be separated into an intracellular current density \vec{j}_{int} and an extracellular

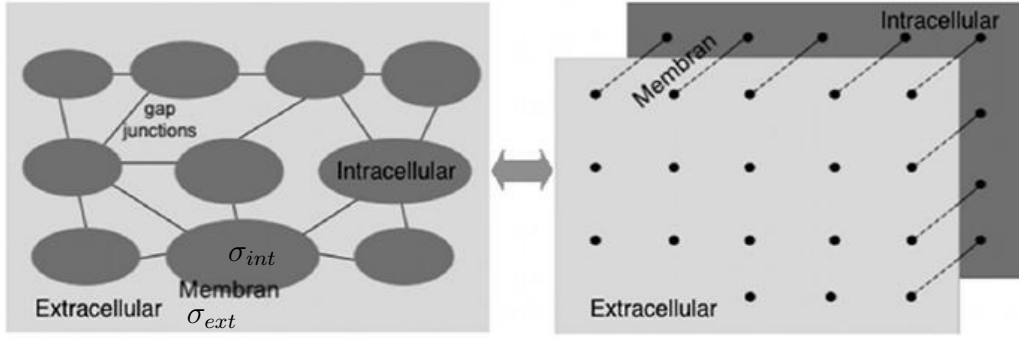


Figure 4.1: In the bidomain model the system of billions of microscopic cardiac muscle cells (*left*) is replaced by a macroscopic intracellular and extracellular space connected by the cell membranes [18] (conductivities σ_{int} , σ_{ext}). While the intracellular space only represents the inside of the *cardiac muscle cells*, the extracellular space is spatially extended over both the cardiac tissue and the surrounding torso tissue.

current density \vec{j}_{ext}

$$\vec{j} = \vec{j}_{int} + \vec{j}_{ext}. \quad (4.1)$$

The intracellular and extracellular currents can be replaced by the electric field using Ohm's law

$$\vec{j}_{int} = \sigma_{int} \vec{E}_{int} \quad (4.2)$$

$$\vec{j}_{ext} = \sigma_{ext} \vec{E}_{ext} \quad (4.3)$$

and because low-frequency bioelectric processes can be treated as quasi-stationary [11] the electric fields can be expressed by the negative gradients of the electric potentials

$$\vec{E}_{int} = -\nabla \varphi_{int} \quad (4.4)$$

$$\vec{E}_{ext} = -\nabla \varphi_{ext} \quad (4.5)$$

so another representation of the total current density is possible

$$\begin{aligned} \vec{j} &= \vec{j}_{int} + \vec{j}_{ext} \\ &= \sigma_{int} \vec{E}_{int} + \sigma_{ext} \vec{E}_{ext} \\ &= -\sigma_{int} \nabla \varphi_{int} - \sigma_{ext} \nabla \varphi_{ext} \\ &= -\sigma_{int} \nabla (\varphi_{int} - \varphi_{ext}) - (\sigma_{ext} + \sigma_{int}) \nabla \varphi_{ext}. \end{aligned} \quad (4.6)$$

By introducing the transmembrane potential (= action potential of the cell)

$$V_m = \varphi_{int} - \varphi_{ext} \quad (4.7)$$

and with the definition of the primary current density

$$\vec{j}_p := -\sigma_{int} \nabla V_m \quad (4.8)$$

that represents the ionic current density inside the depolarization wavefront, equation (4.6) can be written as

$$\begin{aligned} \vec{j} &= \vec{j}_p - (\sigma_{ext} + \sigma_{int}) \nabla \varphi_{ext} \\ &= \vec{j}_p + \sigma \vec{E}_{ext} \end{aligned} \quad (4.9)$$

with the total conductivity $\sigma = \sigma_{ext} + \sigma_{int}$. Because outside the cardiac tissue the intracellular space doesn't exist, the intracellular current vanishes (or $\sigma_{int} = 0$ and $\sigma = \sigma_{ext}$) and the second term can be identified as the total current density outside the cardiac tissue, the secondary or volume current density

$$\vec{j}_V = \sigma \vec{E}_{ext} = \sigma \vec{E}. \quad (4.10)$$

So in terms of the primary current density \vec{j}_p inside the cardiac tissue and the volume current density \vec{j}_V the total current density is

$$\vec{j} = \vec{j}_p + \vec{j}_V. \quad (4.11)$$

4.2 From primary current dipoles to MCG signal

Because the bioelectric processes are quasi-stationary [11] in the continuity equation the temporal change of the charge density $\frac{\partial \rho}{\partial t}$ can be neglected, the local charge conservation is fulfilled and the total current density is solenoidal

$$\nabla \cdot \vec{j} + \frac{\partial \rho}{\partial t} = \nabla \cdot \vec{j} = 0 = \nabla \cdot (\vec{j}_p + \vec{j}_V). \quad (4.12)$$

Let $\partial\Omega$ be the surface of the torso volume Ω (outer boundary in figure 3.2). The boundary condition for the magnetocardiography volume conduction problem is that the component $j_{V,\perp}$ of the volume current perpendicular to the torso surface $\partial\Omega$ vanishes on the torso surface

$$j_{V,\perp}|_{\partial\Omega} = (\vec{j}_V \cdot \vec{n})|_{\partial\Omega} \equiv 0 \quad (4.13)$$

with the normal vector \vec{n} of the torso surface $\partial\Omega$. So the volume conduction problem can be summarized as

$$\begin{aligned} \nabla \cdot (\vec{j}_p + \vec{j}_V) &= 0 \quad \text{in } \Omega \\ (\vec{j}_V \cdot \vec{n})|_{\partial\Omega} &= 0 \quad \text{on } \partial\Omega. \end{aligned} \quad (4.14)$$

After the solution of the volume conduction problem of equation (4.14) for a given primary current density the quasi-stationary magnetic field can be calculated by the Biot-Savart law

$$\begin{aligned}\vec{B}(\vec{R}, t) &= \frac{\mu_0}{4\pi} \int d^3\vec{r} \vec{j}_p(\vec{r}, t) \times \frac{\vec{R} - \vec{r}}{|\vec{R} - \vec{r}|^3} \\ &+ \frac{\mu_0}{4\pi} \int d^3\vec{r} \vec{j}_V(\vec{r}, t) \times \frac{\vec{R} - \vec{r}}{|\vec{R} - \vec{r}|^3}.\end{aligned}\quad (4.15)$$

The signal of the i -th magnetometer of the MCG sensor array is proportional to the magnetic flux $\varphi_{B,i}(t)$ through the area of the i -th magnetometer

$$\varphi_{B,i}(t) = \int_{\text{sensor } i} d\vec{f} \cdot \vec{B}(\vec{R}, t) \quad (4.16)$$

with the surface vector $d\vec{f}$ normal to the sensor area. For the n grid locations \vec{r}_k of the cubic ventricular grid of the cellular automaton model in figure 3.4 consider now a primary current density $\vec{j}_p(\vec{r}, t)$ which is the sum of n primary current dipoles $\vec{j}_p(\vec{r}_k, t)$ distributed over the grid¹

$$\vec{j}_p(\vec{r}, t) = \sum_{k=1}^n \delta(\vec{r} - \vec{r}_k) \vec{j}_p(\vec{r}_k, t). \quad (4.17)$$

Because the volume conduction problem (4.14) is a system of linear equations, the corresponding volume current density can also be written as a linear combination of the primary current dipoles $\vec{j}_p(\vec{r}_k, t)$ to satisfy the equation (4.14) ($\nabla \cdot \vec{j}_V = -\sum_{k=1}^n \vec{j}_p(\vec{r}_k, t) \cdot \nabla \delta(\vec{r} - \vec{r}_k)$)

$$\vec{j}_V(\vec{r}, t) = \sum_{k=1}^n \mathbf{A}(\vec{r}, \vec{r}_k) \vec{j}_p(\vec{r}_k, t) \quad (4.18)$$

with a (3×3) -matrix $\mathbf{A}(\vec{r}, \vec{r}_k)$. Inserting the primary current density (4.17) and the volume current density (4.18) into equation (4.15) and then equation (4.15) into equation (4.16), the MCG signal vector $(\varphi_{B,1}(t), \dots, \varphi_{B,m}(t))^T$ for m magnetometers can be written as a matrix product with the primary current dipoles

$$\varphi(t) = \begin{pmatrix} \varphi_{B,1}(t) \\ \vdots \\ \varphi_{B,m}(t) \end{pmatrix} = \mathbf{L} \begin{pmatrix} \vec{j}_p(\vec{r}_1, t) \\ \vdots \\ \vec{j}_p(\vec{r}_n, t) \end{pmatrix} = \mathbf{L}\mathbf{J}_p(t) \quad (4.19)$$

with the $(m \times 3n)$ leadfield matrix \mathbf{L} .

In this work the leadfield matrix \mathbf{L} is calculated with the Finite Element Method (FEM [24]) and 3-dimensional tetrahedral meshes for the ventricles, lungs and torso tissue in the solution of the volume conduction problem of equation (4.14). The tetrahedral meshes for figure 3.2 include 48780 tetrahedrons in the ventricles, 8045 tetrahedrons in the lungs and 238305 tetrahedrons in the torso tissue. It has been

¹Under the assumption of a homogeneous primary current density inside a cubic cell one can set $\vec{j}_p(\vec{r}, t)d^3 = \vec{j}_p(\vec{r}, t)$ so $\vec{j}_p(\vec{r}, t)$ and $\vec{j}_p(\vec{r}_k, t)$ have different units.

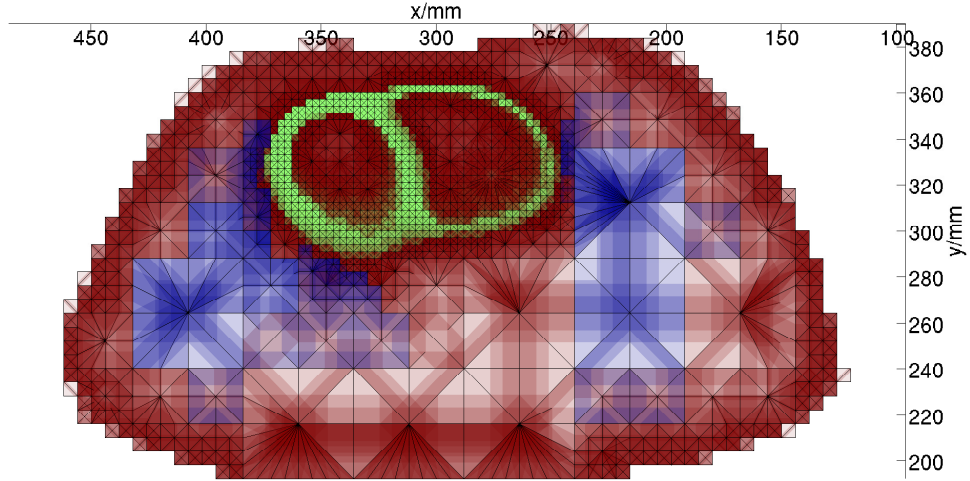


Figure 4.2: Horizontal slice through tetrahedral mesh perpendicular to z -axis for the solution of the volume conduction problem (slice thickness $\Delta z = 20 \text{ mm}$, torso tissue in red, lungs in blue, ventricles in green). The highest density of the tetrahedrons can be found in close proximity to the primary currents in the ventricles.

shown previously [25] that a local mesh refinement of the tetrahedrons in close proximity to the ventricles and the boundary of the torso improves the inverse solution, so the density of the tetrahedrons has been chosen to be inhomogeneous (figure 4.2). The piecewise homogeneous and isotropic electrical conductivities σ of the tissues were set as in [8]: $\sigma = 0.20 \text{ S/m}$ (torso), $\sigma = 0.08 \text{ S/m}$ (lungs) and $\sigma = 0.60 \text{ S/m}$ (cardiac tissue, average of conductivity parallel and transverse to muscle fiber directions).

For the practical calculation of the leadfield matrix \mathbf{L} the program SimBio NeuroFEM [26] [27] [28] developed by the Jena university was used. In principle the program calculates the magnetic flux through the area of the sensors (magnetometers) for the case of single primary current dipoles which are paraxial unit vectors:

$$\mathbf{J}_p(t) = \begin{pmatrix} 0 \\ \vdots \\ 1 \\ \vdots \\ 0 \end{pmatrix} = \mathbf{e}_i, \quad \text{for } i = 1, \dots, 3n. \quad (4.20)$$

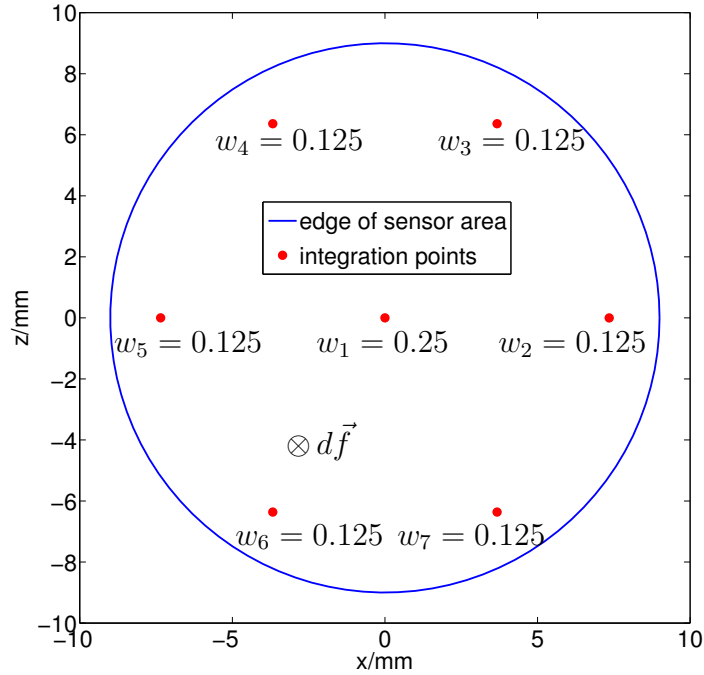


Figure 4.3: Distribution of the integration points for the numerical calculation of the magnetic flux through a circular magnetometer in the MCG sensor array. w_1, \dots, w_7 denote the weights of the integration points.

The sensors are circular magnetometers with radius $r = 9 \text{ mm}$. In SimBio NeuroFEM the magnetic flux through a sensor is calculated by a numerical integration over 7 integration points (figure 4.3) with the weights $w_1 = 0.25$ (center) and $w_2 = \dots = w_7 = 0.125$ (peripheral). The surface vector $d\vec{f}$ for the calculation of the magnetic flux in equation (4.16) is perpendicular to the area of the circle in figure 4.3.

4.3 From activation times to primary current dipoles

In this section it will be explained, how the vector $\mathbf{J}_p(t) = (\vec{j}_p(\vec{r}_1, t), \dots, \vec{j}_p(\vec{r}_n, t))^T$ including the primary current dipoles in equation (4.19) can be calculated for a fixed time t as a function of the activation time state vector

$$\mathbf{x} := (\tau(\vec{r}_1), \dots, \tau(\vec{r}_n))^T \quad (4.21)$$

that includes the activation times $\tau(\vec{r}_k)$ of the n cubic cells in the ventricles. With equation (4.8) and the action potential model $a(t - \tau(\vec{r}))$ of figure 4.4 the primary current density for a cell at position \vec{r} at the fixed time t is (figure 4.5)

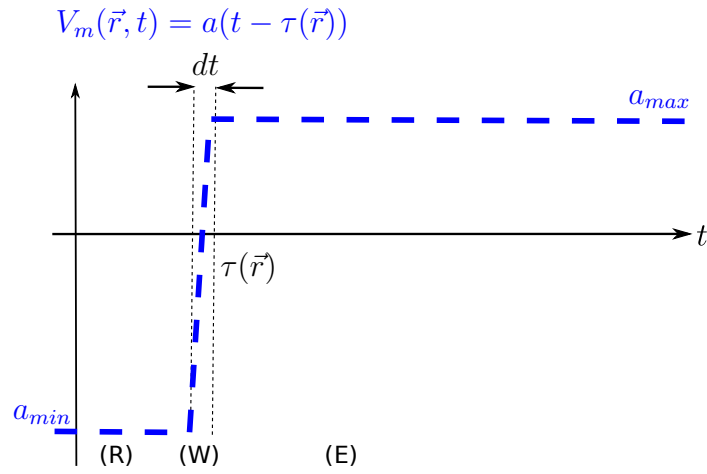


Figure 4.4: The action potential model $a(t - \tau(\vec{r}))$ of a ventricular cell at the fixed position \vec{r} showing only the depolarization at the activation time $\tau(\vec{r})$ (compare figure 3.3).

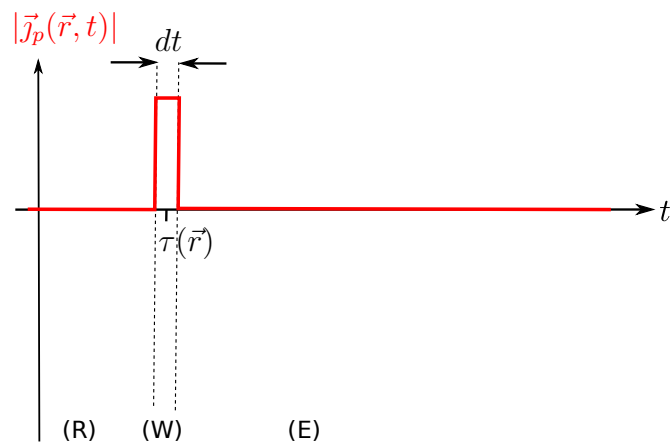


Figure 4.5: The primary current density $\vec{j}_p(\vec{r}, t)$ of a ventricular cell at the fixed position \vec{r} corresponding to the action potential model of figure 4.4.

$$\begin{aligned}
\vec{j}_p(\vec{r}, t) &= -\sigma_{int} \nabla V_m(\vec{r}, t) = -\sigma_{int} a'(t - \tau(\vec{r})) \nabla \tau(\vec{r}) \\
&= -\sigma_{int} \nabla \tau(\vec{r}) \cdot \begin{cases} \frac{a_{max} - a_{min}}{dt} & , \text{if } t - dt/2 \leq \tau(\vec{r}) \leq t + dt/2 \\ 0 & \text{else.} \end{cases} \quad (4.22)
\end{aligned}$$

For a sufficiently small lattice constant d (= size of a cubic ventricular cell) in the cubic ventricular grid the gradient of the activation time $\nabla \tau(\vec{r})$ can now be approximated by difference quotients with the help of the activation times $\tau(\vec{r} \pm d\vec{e}_i)$ of the adjacent cells:

$$\nabla \tau(\vec{r}) = \begin{pmatrix} \frac{\tau(\vec{r} + d\vec{e}_x) - \tau(\vec{r} - d\vec{e}_x)}{2d} \\ \frac{\tau(\vec{r} + d\vec{e}_y) - \tau(\vec{r} - d\vec{e}_y)}{2d} \\ \frac{\tau(\vec{r} + d\vec{e}_z) - \tau(\vec{r} - d\vec{e}_z)}{2d} \end{pmatrix}. \quad (4.23)$$

By evaluating the equations (4.22) and (4.23) for the n dipole positions $\vec{r} = \vec{r}_1, \dots, \vec{r}_n$ the vector of all primary current dipoles $\mathbf{J}_p(t) = (\vec{j}_p(\vec{r}_1, t), \dots, \vec{j}_p(\vec{r}_n, t))^T$ only depends on the activation times $\mathbf{x} = (\tau(\vec{r}_1), \dots, \tau(\vec{r}_n))^T$, the time t and constants

$$\mathbf{J}_p(t) \equiv \mathbf{J}_p(t, \mathbf{x}). \quad (4.24)$$

4.4 The MCG signal function $\mathbf{h}(\mathbf{x})$ of the activation times

By inserting the equation (4.24) into the MCG signal equation (4.19) also the MCG signal vector $\boldsymbol{\varphi}(t)$ of the time t can be written as a function of the activation times $\mathbf{x} = (\tau(\vec{r}_1), \dots, \tau(\vec{r}_n))^T$

$$\boldsymbol{\varphi}(t) = \mathbf{L}\mathbf{J}_p(t, \mathbf{x}). \quad (4.25)$$

Evaluating the left hand side of equation (4.25) for N data time samples $t = t_1, \dots, t_N$ and concatenating the corresponding MCG signal vectors $\boldsymbol{\varphi}(t_i)$ into one column vector one can define a total MCG data vector

$$\boldsymbol{\phi} := (\boldsymbol{\varphi}(t_1)^T, \dots, \boldsymbol{\varphi}(t_N)^T)^T \quad (4.26)$$

which for m sensors is a $(m \cdot N \times 1)$ vector. The concatenation of the right hand sides of equation (4.25) is defined as the MCG signal function

$$\mathbf{h}(\mathbf{x}) := ((\mathbf{L}\mathbf{J}_p(t_1, \mathbf{x}))^T, \dots, (\mathbf{L}\mathbf{J}_p(t_N, \mathbf{x}))^T)^T. \quad (4.27)$$

From the equations (4.25), (4.26) and (4.27) follows the theoretical MCG signal corresponding to the activation times \mathbf{x}

$$\boldsymbol{\phi} = \mathbf{h}(\mathbf{x}). \quad (4.28)$$

Because the primary current density $\vec{j}_p(\vec{r}, t)$ in equation (4.22) is a nonlinear (and

even non-smooth) function of the activation times $\mathbf{x} = (\tau(\vec{r}_1), \dots, \tau(\vec{r}_n))^T$ (figure 4.5), also the MCG signal function $\mathbf{h}(\mathbf{x})$ is a nonlinear function of the activation times \mathbf{x} .

Chapter 5

Investigated geometries of the MCG sensor arrays

In this chapter the quality of different sensor arrays will be compared. In the section 5.1 the 64 channel MCG system CS-MAG of the company Biomagnetik Park [1] will be investigated with a theoretical single dipole model and a comparison with experimental results. In the section 5.2 a rectangular (6×6)-array, which is used for the inverse simulations of chapter 6, will be investigated.

5.1 MCG system CS-MAG of Biomagnetik Park [1]

In this section the MCG sensor array CS-MAG of the company Biomagnetik Park [1] will be investigated. It is made of a circular array with 64 axial SQUID gradiometers (figure 5.1, *left*) cooled in a cylindrical fluid Helium dewar in a magnetically shielded room (figure 5.1, *right*). To investigate the importance of measurements from ventral and dorsal, there has been made an experimental study with heart-healthy subjects [29] in 5 dorsal and 5 ventral layers (figure 5.2). Although the signal to noise ratio decreases with the distance to the torso, ventral double layers were investigated, because on the one hand the signal in the second ventral layer may be bigger than the signal in the first dorsal layer. On the other hand a change of the magnetic field topology with a bigger distance of the sensors may improve the condition number of the leadfield matrix. The distance between two adjacent layers was 2 *cm*, the distance between the dewar and the thorax was 1 *cm*.

5.1.1 Theoretical model investigations

In this section the 64 channel MCG sensor array of figure 5.1 is applied to the standard anatomy of the program ECGSIM [19] to localize single primary current dipoles inside the thorax. While in practice with the MCG system of figure 5.1 only measurements from one side of the body are possible, in this section arrays with both ventral and dorsal sensors will be investigated, so the number of MCG sensors is $m = 2 \cdot 64 = 128$.

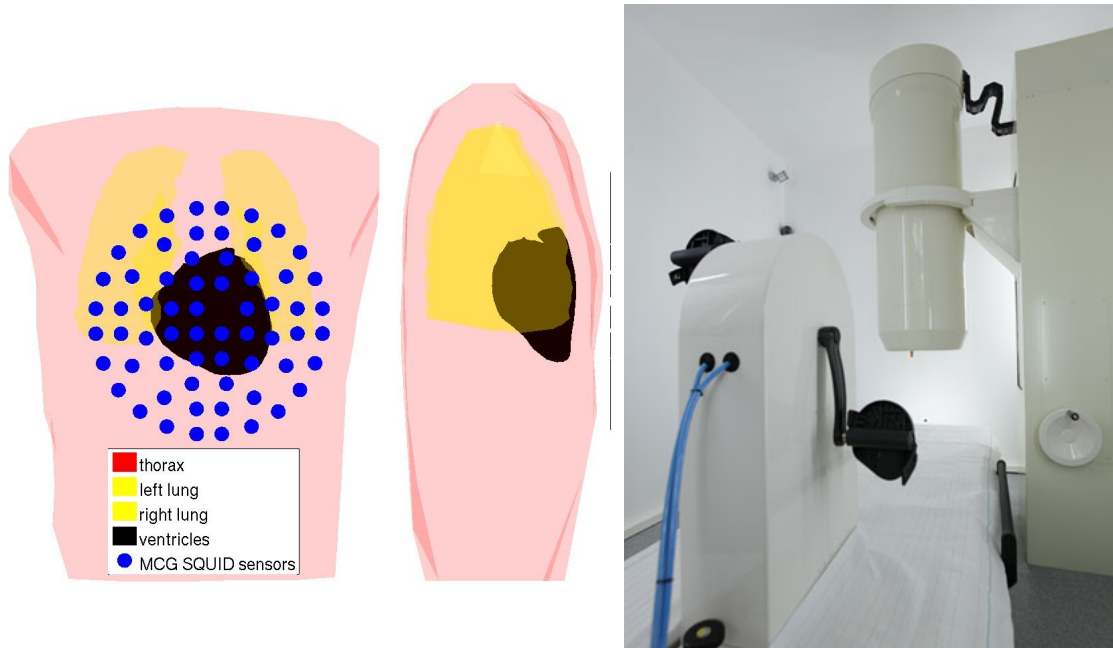


Figure 5.1: ECGSIM standard geometries of the healthy young male [19] (*left*) with the MCG SQUID sensors of the Biomagnetik Park MCG system CS-MAG [1] (*right*). The radius of a SQUID sensor is $r = 9 \text{ mm}$.

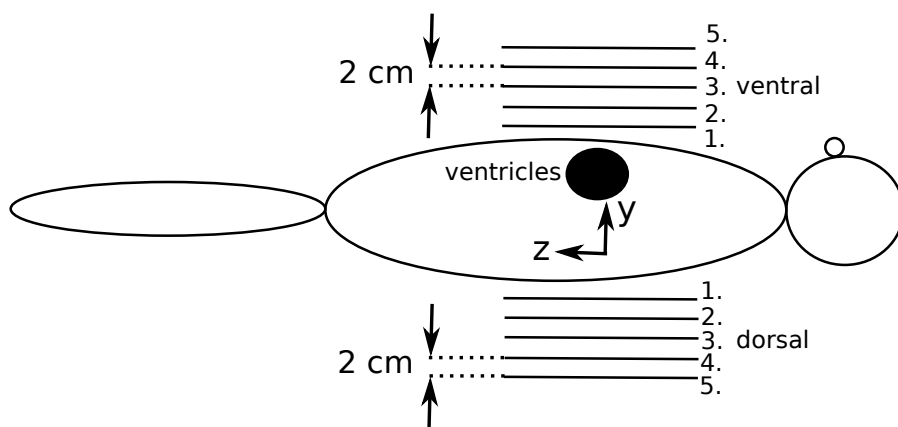


Figure 5.2: In the measurements of M. Schulte [29] the circular sensor array of figure 5.1 was located in the layers *ventral1* to *ventral5* and *dorsal1* to *dorsal5*.

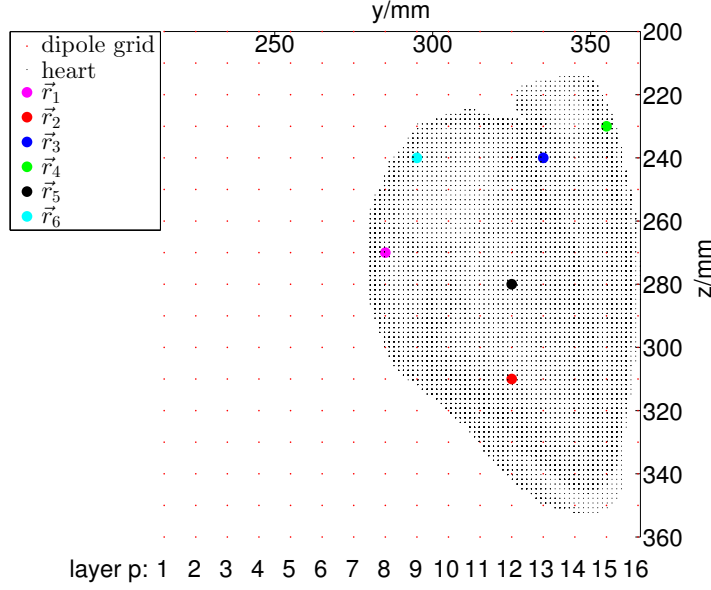


Figure 5.3: Side view of the dipole grid (red), ventricles (black) and the 6 true dipole locations $\vec{r}_1 = (335, 285, 270)mm$, $\vec{r}_2 = (255, 325, 310)mm$, $\vec{r}_3 = (345, 335, 240)mm$, $\vec{r}_4 = (285, 355, 230)mm$, $\vec{r}_5 = (305, 325, 280)mm$, $\vec{r}_6 = (305, 295, 240)mm$.

Three different cases of combined sensor arrays will be investigated (sensor layers of figure 5.2):

- **A:** *ventral1ventral2* (figure 5.4)
- **B:** *dorsal1dorsal2* (figure 5.7)
- **C:** *ventral1dorsal1* (figure 5.10)

In the simulations a single primary current dipole $\vec{j}_p = [1, 0, 1]j_p$ is placed inside the ventricles (*true dipole location* in figure 5.4). By the solution of the volume conduction problem, as explained in chapter 4, the leadfield matrix \mathbf{L} is calculated for a $(17 \times 16 \times 17)$ cubic dipole grid with a lattice constant of 10 mm (figure 5.3, red dots). The corresponding $(m \times 1)$ MCG signal vector $\varphi = \mathbf{L}\mathbf{J}_p$ (equation (1.1)) is calculated and used for the localization of the single current dipole. The single dipole localization technique used in this section is the MUltiple Signal Classification (MUSIC, [30]) which is briefly summarized here: Let

$$\varphi = \mathbf{U}\mathbf{\Sigma}\mathbf{V}^T \quad (5.1)$$

be the Singular Value Decomposition (SVD) of the data matrix φ for r dipoles where $\mathbf{\Sigma} = \text{Diag}(\sigma_i)$ is the diagonal matrix containing the singular values σ_i of the data matrix φ , the columns of \mathbf{U} contain the left singular vectors of φ and the columns of \mathbf{V} contain the right singular vectors of φ . The orthogonal projector to the noise subspace is defined as

$$\mathbf{P}^\perp = \mathbf{U}_{m-r} \mathbf{U}_{m-r}^T \quad (5.2)$$

where \mathbf{U}_{m-r} contains the column vectors of \mathbf{U} corresponding to the $m-r$ smallest singular values. Let \mathbf{L}_i be the $(m \times 3)$ leadfield matrix corresponding to the i -th primary current dipole. Then the MUSIC scanning function is defined as [30]

$$M(i) = \frac{\|\mathbf{P}^\perp \mathbf{L}_i\|^2}{\|\mathbf{L}_i\|^2} \quad (5.3)$$

and the r dipoles can be found by plotting $1/M(i)$ at all dipole grid locations and looking for r sharp peaks. The MUSIC single dipole localization ($r = 1$) is tested for 6 true dipole locations \vec{r}_i inside the ventricles (figure 5.3).

The figures 5.4 to 5.12 show the MUSIC single dipole localization results for the true dipole location \vec{r}_1 inside the posterior part of the ventricles. For each of the 3 investigated sensor arrays a side view, the corresponding MUSIC map $1/M(i)$ and a front view is shown. In the side views and the MUSIC maps the layers $p = 1, \dots, 16$ denote the (17×17) dipole grid layers parallel to the $x - z$ -plane. In the MUSIC maps the interval $[p-1, p]$ includes all MUSIC amplitudes $1/M(i)$ of the layer p . The MUSIC dipole location is calculated from the maximum of the MUSIC map $1/M(i)$ and the Localization Error LE is the distance between the true dipole location and the MUSIC dipole location.

The figures 5.4 to 5.6 show the MUSIC localization results for \vec{r}_1 and the sensor array *ventral1ventral2* (ventral double layer). The result is that the MUSIC dipole location is shifted away from the sensors into the posterior half of the body (layer $p = 1$, figure 5.4). The shift parallel to the sensor layers is smaller than the shift perpendicular to the sensor layers. The Localization Error is $LE = 76 \text{ mm}$.

The figures 5.7 to 5.9 show the MUSIC localization results for \vec{r}_1 and the sensor array *dorsal1dorsal2* (dorsal double layer). The result is that the MUSIC dipole location is shifted away from the sensors into the anterior half of the body (layer $p = 14$, figure 5.7). The shift parallel to the sensor layers is smaller than the shift perpendicular to the sensor layers. The Localization Error is $LE = 67 \text{ mm}$.

The figures 5.10 to 5.12 show the MUSIC localization results for \vec{r}_1 and the sensor array *ventral1dorsal1* (sensors on both the anterior and posterior side of the torso). The result is that the MUSIC dipole location remains in the same layer as the true dipole location (layer $p = 8$, figure 5.7). The Localization Error is $LE = 28 \text{ mm}$.

The comparison of the Localization Errors for \vec{r}_1 and the 3 sensor arrays results in $LE_{ventral1dorsal1} < LE_{dorsal1dorsal2} < LE_{ventral1ventral2}$, so for \vec{r}_1 the sensor array *ventral1dorsal1* results in the smallest Localization Error. In order to check whether the sensor array *ventral1dorsal1* also results in the smallest Localization Error averaged over the 6 dipole locations $\vec{r}_1, \dots, \vec{r}_6$, table 5.1 shows the Localization Errors for the 6 dipole locations and 5 different sensor arrays. In table 5.1 LE_i is the Localization Error for the i -th dipole and the average Localization Error is defined as $\overline{LE} = \frac{1}{6} \sum_i LE_i$.

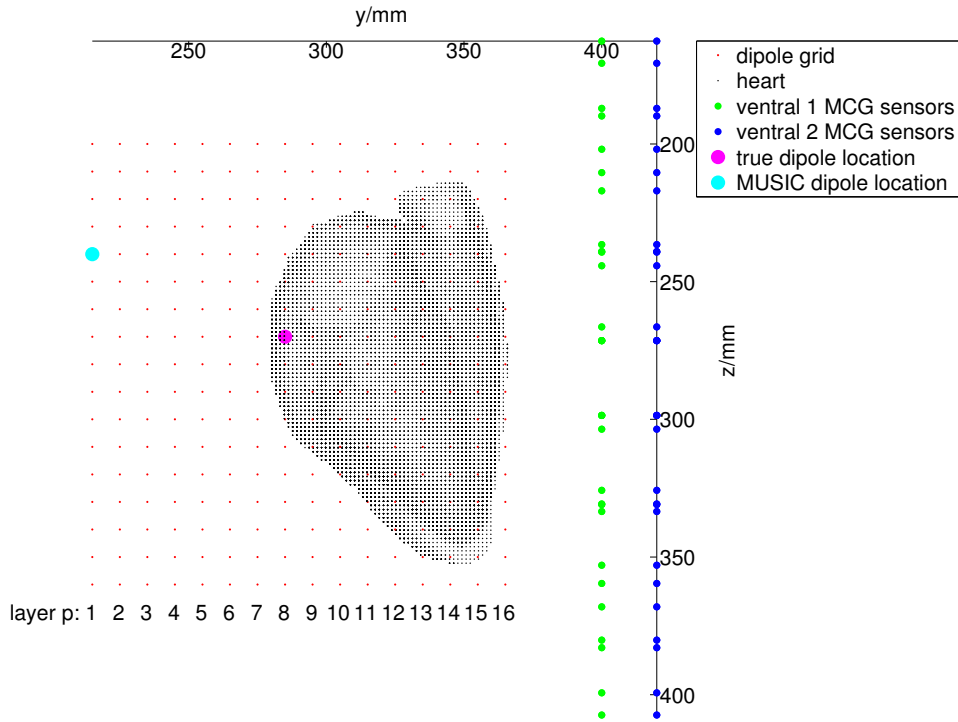


Figure 5.4: Side view of the sensor array *ventral1ventral2* (figure 5.2, ventral double layer) with true dipole location $\vec{r}_1 = (335, 285, 270)mm$.

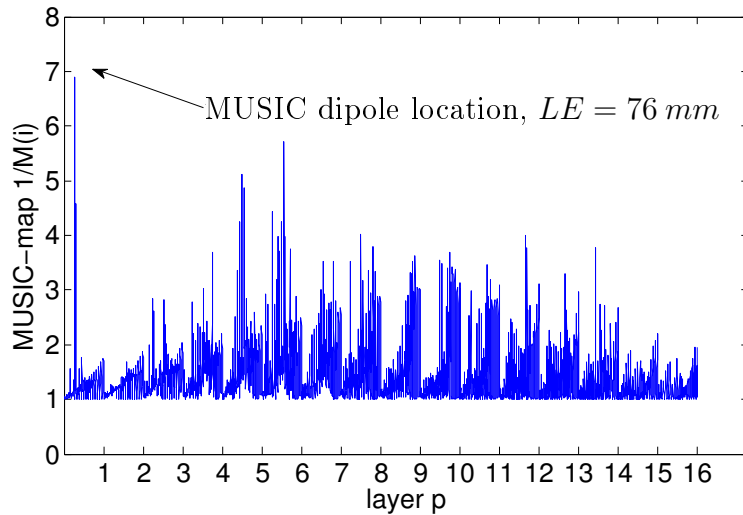


Figure 5.5: MUSIC map $1/M(i)$ of the sensor array *ventral1ventral2* (figure 5.2, ventral double layer) with true dipole location $\vec{r}_1 = (335, 285, 270)mm$. The x -axis interval $[p-1, p]$ includes all MUSIC amplitudes $1/M(i)$ of the layer p . $LE = 76 mm$ is the Localization Error between the true and MUSIC dipole location.

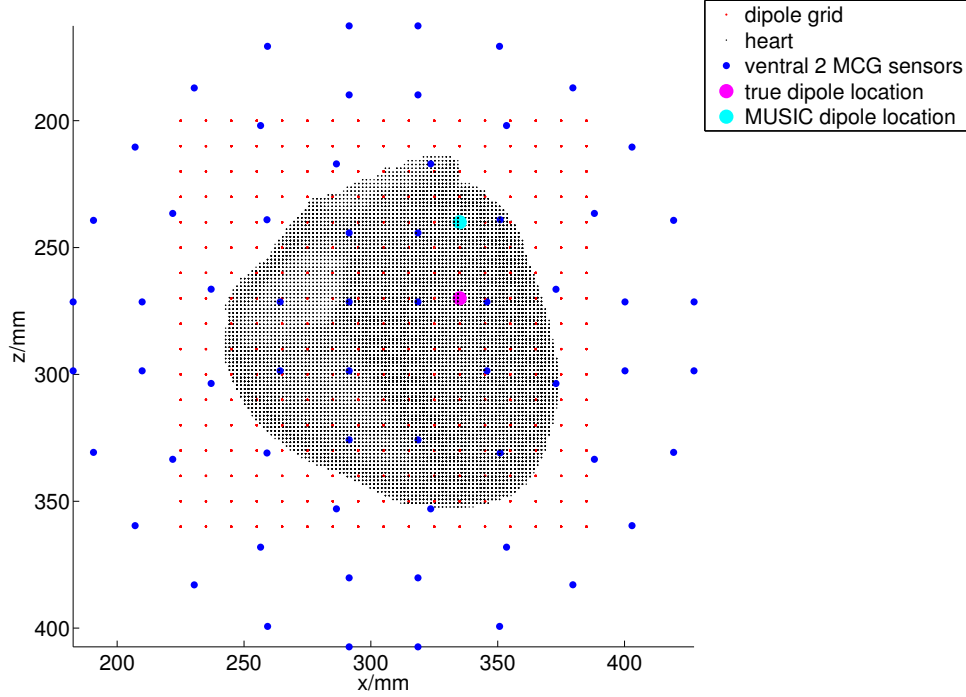


Figure 5.6: Front view of the sensor array *ventral1ventral2* (figure 5.2, ventral double layer) with true dipole location $\vec{r}_1 = (335, 285, 270)mm$.

	$\frac{LE_1}{mm}$	$\frac{LE_2}{mm}$	$\frac{LE_3}{mm}$	$\frac{LE_4}{mm}$	$\frac{LE_5}{mm}$	$\frac{LE_6}{mm}$	$\frac{\overline{LE}}{mm}$	κ
<i>ventral1</i>	76.16	90.00	76.16	46.90	41.23	31.62	60.35	$1.0 \cdot 10^9$
<i>ventral1ventral4</i>	76.16	90.00	76.16	46.90	41.23	31.62	60.35	$3.2 \cdot 10^{12}$
<i>ventral1ventral2</i>	76.16	90.00	76.16	46.90	41.23	31.62	60.35	$1.3 \cdot 10^{11}$
<i>dorsal1dorsal2</i>	67.08	96.95	156.52	54.77	22.36	36.06	72.29	$1.2 \cdot 10^{11}$
<i>ventral1dorsal1</i>	28.28	0.00	24.49	46.90	22.36	22.36	24.07	$3.8 \cdot 10^9$

Table 5.1: Localization Errors LE , the distance between the true and MUSIC dipole location, for the sensor arrays *ventral1*, *ventral1ventral4*, *ventral1ventral2*, *dorsal1dorsal2* and *ventral1dorsal1*. \overline{LE} is the averaged LE and the last column shows the condition numbers $\kappa \equiv \text{cond}(\mathbf{L})$ of the leadfield matrices.

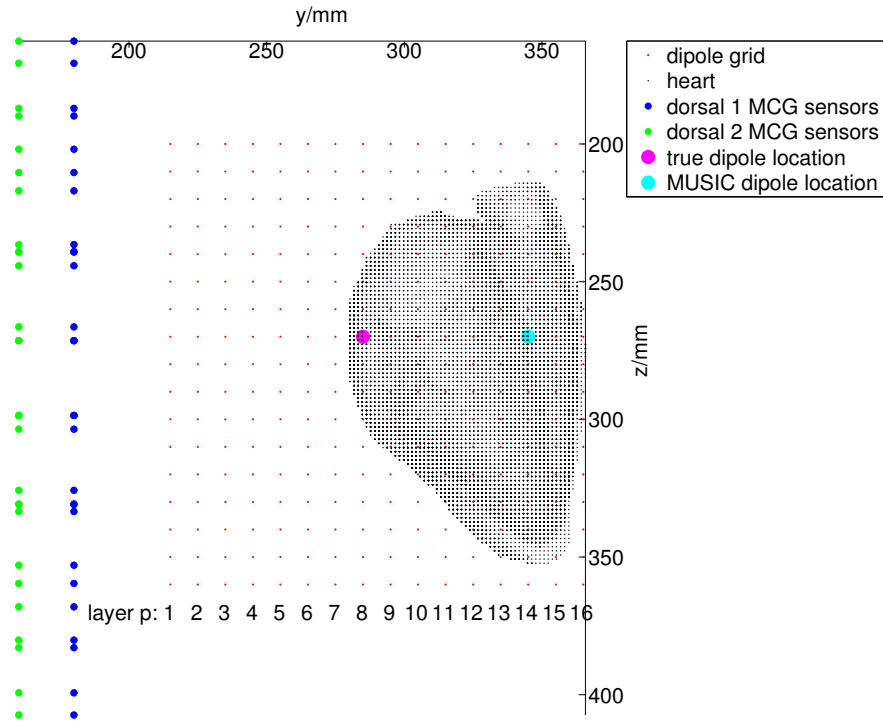


Figure 5.7: Side view of the sensor array *dorsal1dorsal2* (figure 5.2, dorsal double layer) with true dipole location $\vec{r}_1 = (335, 285, 270)mm$.

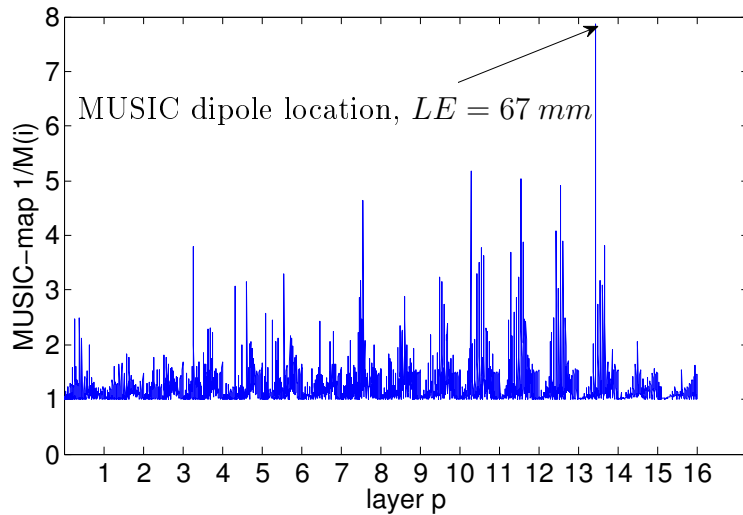


Figure 5.8: MUSIC map $1/M(i)$ of the sensor array *dorsal1dorsal2* (figure 5.2, dorsal double layer) with true dipole location $\vec{r}_1 = (335, 285, 270)mm$. The x -axis interval $[p - 1, p]$ includes all MUSIC amplitudes $1/M(i)$ of the layer p . $LE = 67 mm$ is the Localization Error between the true and MUSIC dipole location.

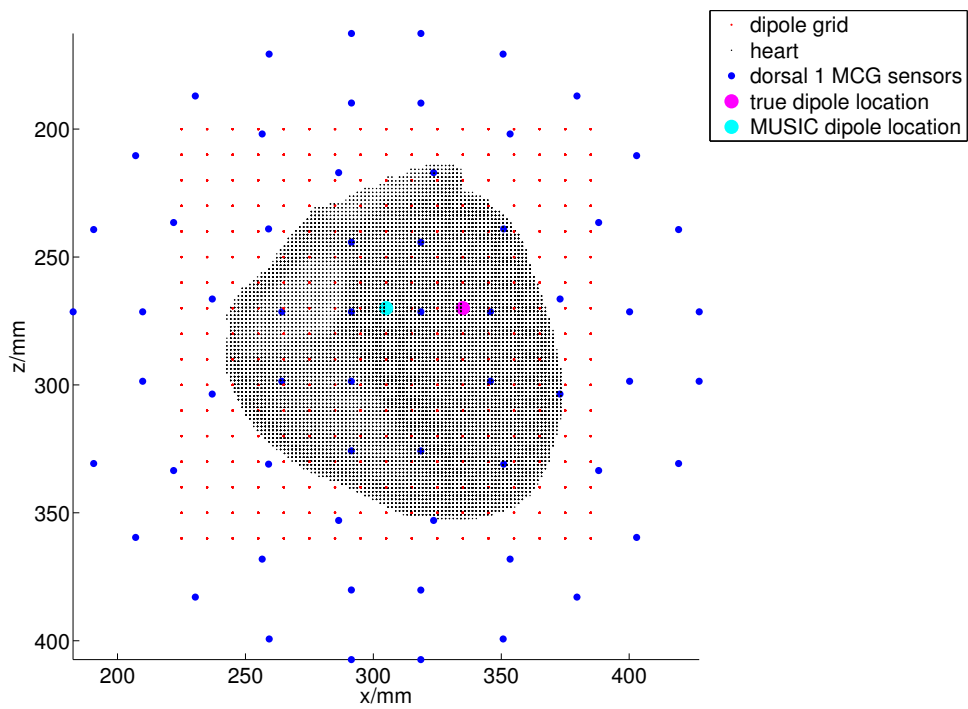


Figure 5.9: Front view of the sensor array *dorsal1dorsal2* (figure 5.2, dorsal double layer) with true dipole location $\vec{r}_1 = (335, 285, 270)mm$.

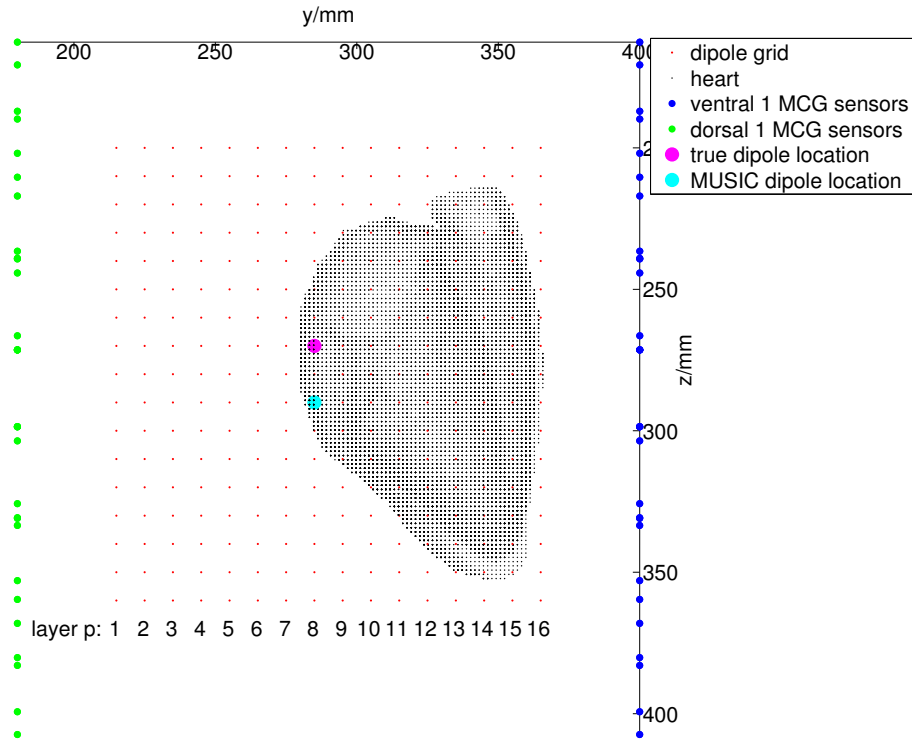


Figure 5.10: Side view of the sensor array *ventral1dorsal1* (figure 5.2) with true dipole location $\vec{r}_1 = (335, 285, 270)mm$.

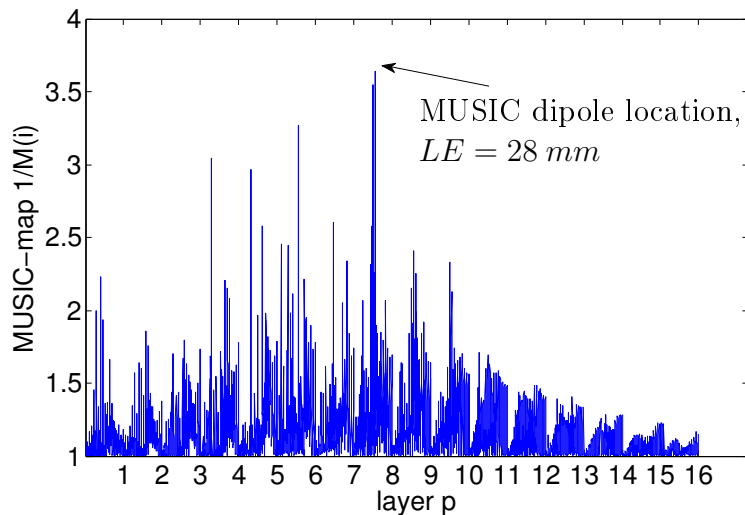


Figure 5.11: MUSIC map $1/M(i)$ of the sensor array *ventral1dorsal1* (figure 5.2) with true dipole location $\vec{r}_1 = (335, 285, 270)mm$. The x -axis interval $[p-1, p]$ includes all MUSIC amplitudes $1/M(i)$ of the layer p . $LE = 28 mm$ is the Localization Error between the true and MUSIC dipole location.

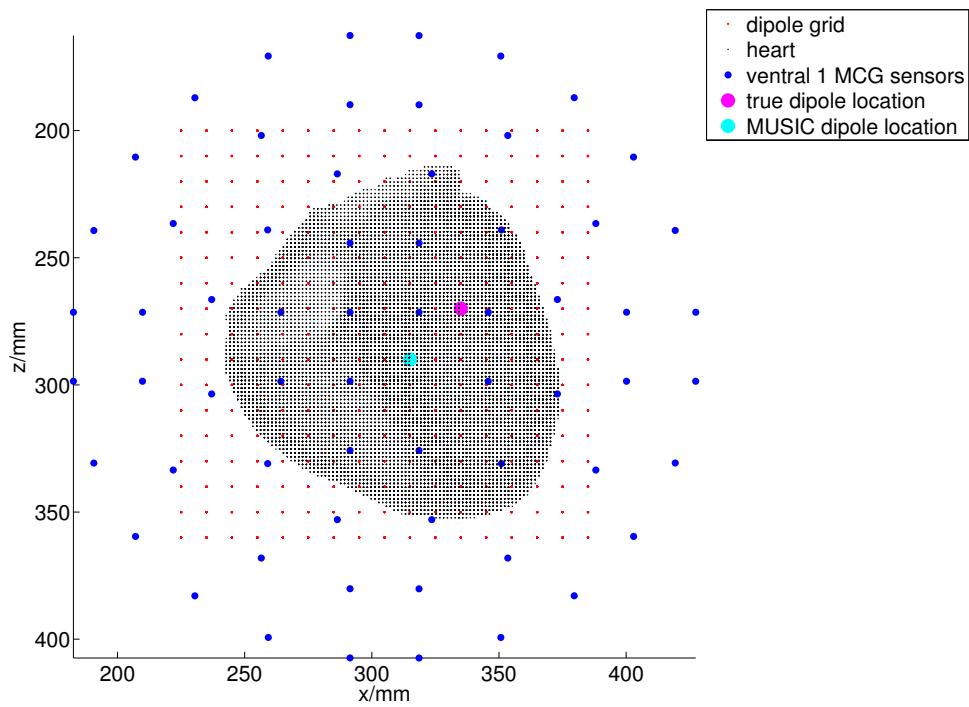


Figure 5.12: Front view of the sensor array *ventral1dorsal1* (figure 5.2) with true dipole location $\vec{r}_1 = (335, 285, 270)mm$.

The column \overline{LE} of table 5.1 shows that the sensor array *ventral1dorsal1* also produces the smallest averaged LE : $\overline{LE}_{ventral1dorsal1} < \overline{LE}_{ventral1ventral2} < \overline{LE}_{dorsal1dorsal2}$.

An explanation to the order of the Localization Errors for the 3 sensor arrays can give the condition number of the leadfield matrix

$$\kappa \equiv cond(\mathbf{L}) = \frac{\max\{\sigma_i\}}{\min\{\sigma_i\}} \quad (5.4)$$

where $\{\sigma_i\}$ are the singular values of the matrix \mathbf{L} . The condition number of the leadfield matrix \mathbf{L} measures the sensitivity $\delta\mathbf{J}$ of the solution of the system of linear equations $\boldsymbol{\varphi} = \mathbf{L}\mathbf{J}$ to errors in the data $\delta\boldsymbol{\varphi}$ [31]

$$\frac{\|\delta\mathbf{J}\|}{\|\mathbf{J}\|} \leq \kappa \frac{\|\delta\boldsymbol{\varphi}\|}{\|\boldsymbol{\varphi}\|}. \quad (5.5)$$

The smaller the condition number of the leadfield matrix $\kappa = cond(\mathbf{L})$ the smaller is the error $\delta\mathbf{J}$ for the inverse solution. Table 5.1 shows that the sensor array *ventral1dorsal1* provides the smallest condition number and so the most stable inverse solutions: The next section will show that the magnetic field topologies of the layers *ventral1* and *ventral2* are very similar and also the magnetic field topologies of the layers *dorsal1* and *dorsal2*. Consequently, the corresponding rows in the leadfield matrix are also very similar.

Table 5.1 also shows the Localization Errors of the sensor array *ventral1ventral4* with a bigger distance between the sensor layers of 6 cm (figure 5.2) and also the single layer sensor array *ventral1* with $m = 64$ sensors. The bigger distance between the sensor layers of the double layer provides a bigger difference between the magnetic fields of the layers so a smaller Localization Error was assumed. But although the condition numbers of the sensor arrays *ventral1ventral2*, *ventral1ventral4* and *ventral1* are different, the Localization Errors stay the same showing that the first layer *ventral1* is crucial for the localization of the dipoles. It should be noted that the condition number of the sensor array *ventral1* is not directly comparable with the condition numbers of the arrays with 128 sensors because of the smaller number of rows in the leadfield matrix of the array *ventral1*.

The bar graph of figure 5.13 summarizes the results for the averaged LE for the investigated sensor arrays.

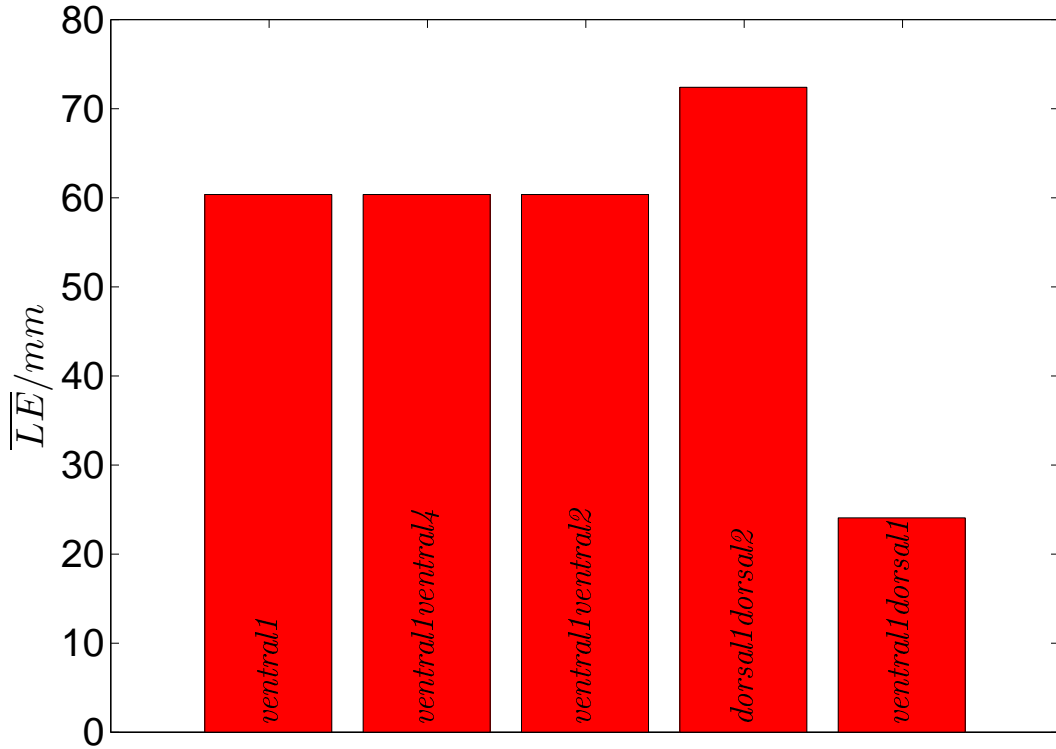


Figure 5.13: Localization Errors LE for the investigated sensor arrays averaged over the 6 ventricular pacer locations of figure 5.3 (MUSIC single dipole localization).

5.1.2 Comparison with experimental results

In this section MCG measurements for 5 heart-healthy subjects (2 male and 3 female of age < 30 years) made by M. Schulte [29] with the MCG system CS-MAG of the company Biomagnetik Park [1] will be presented and compared with theoretical single dipole results. The measurement layers are shown schematically in figure 5.2. The figures 5.15 to 5.24 show the linearly interpolated MCG-signal of the 5 subjects at the time of the R-peak for the layer *ventral1* (column left) and the layer *dorsal1* (column right).

The figure 5.14 shows how the angle ψ of the electric axis of the heart is calculated from the measured MCG-signal without using any anatomical information of the subject: first the maximum and minimum of the measured ventral MCG-signal are connected with a white arrow. The direction of the electric axis can be determined as the black arrow in figure 5.14, which is the direction of the white arrow rotated clockwise by 90° . In the figures 5.15 to 5.23 the direction of the electric axis is denoted by a black arrow and the corresponding measured angle between the electric axis and the x -axis is in the range $-45^\circ \leq \psi \leq 0^\circ$. These measurement results lie within the normal range of the electric axis ($-110^\circ \leq \psi \leq +30^\circ$, [11]) of the healthy heart.

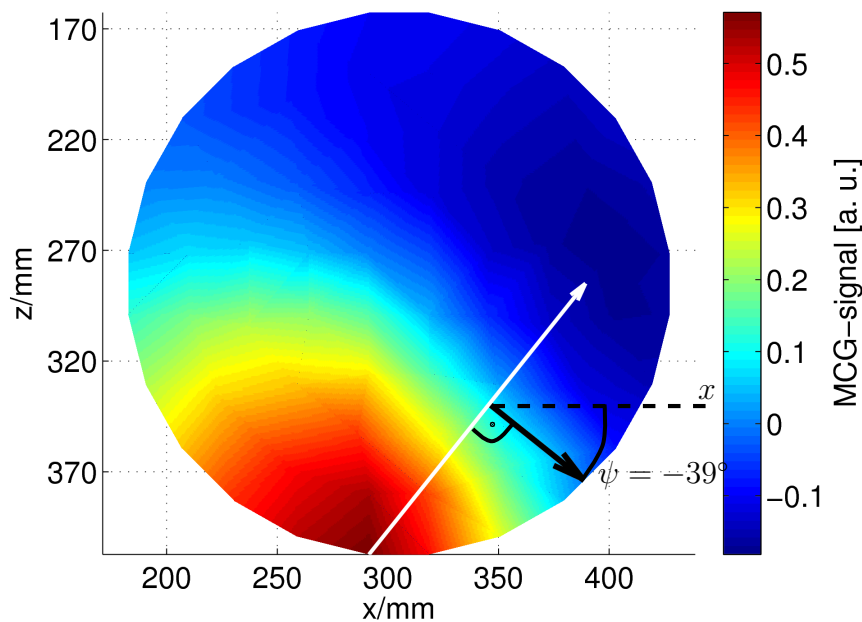


Figure 5.14: The angle ψ of the electric axis (black arrow) is perpendicular to the connection (white arrow) of the maximum and minimum of the MCG-signal (R-peak of subject 3, ventrall).

For comparison the figures 5.25 and 5.26 show measurements of the ventral MCG-signal map and the electric axis at the time of the R-peak taken from the literature.

In the following the measured MCG data of the 5 subjects will be used to localize a primary current dipole in the heart that corresponds to the R-peak activation of the heart. In contrast to the theoretical model investigations of the last subsection, here the location of the true primary current dipole at the time of the R-peak is not known: here the true primary current dipole is the approximation for the primary currents that are distributed globally all over the depolarization wavefront of the R-peak time. Because at the time of the R-peak the depolarization wavefront is distributed over large areas of the apex and the left ventricle (figure 5.26), here the single dipole MUSIC localization approach can only give a rough approximation for the location of the apex. In the figures 5.27 to 5.35 the true location of the apex is estimated geometrically from the anatomy of the ventricles and called apex location (magenta) and the Localization Error is calculated as the distance between the MUSIC dipole location and the apex location. For the calculation of the MUSIC dipole location here no simulated data is used but only the R-peak data of the subject and the leadfield matrix of the subjects anatomy. Because in the study [29] there were no patient specific anatomies (e.g. from MRI-scans) available, the anatomy for all subjects is assumed to be the standard ECGSIM geometry (figure 5.1, left) and consequently also the leadfield matrix is assumed to be identical for all subjects.

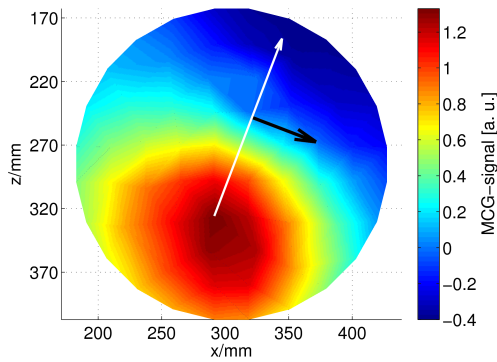


Figure 5.15: Subject 1 (female), sensor array *ventral1*, MCG-signal at R-peak, $\psi = -21^\circ$.

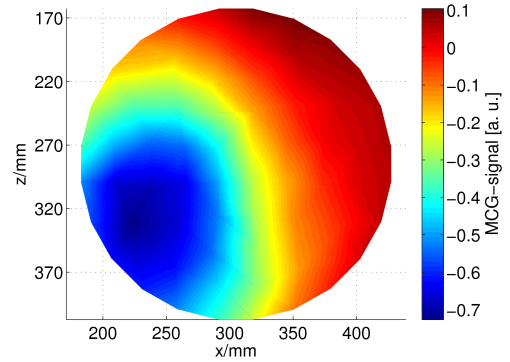


Figure 5.16: Subject 1 (female), sensor array *dorsal1*, MCG-signal at R-peak.

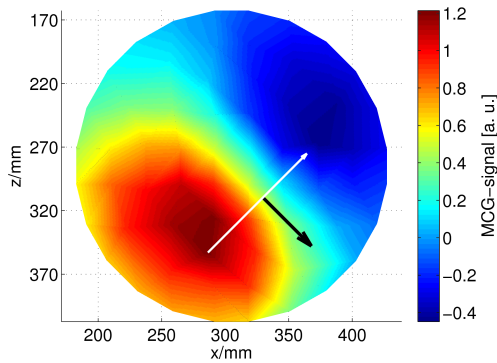


Figure 5.17: Subject 2 (male), sensor array *ventral1*, MCG-signal at R-peak, $\psi = -45^\circ$.

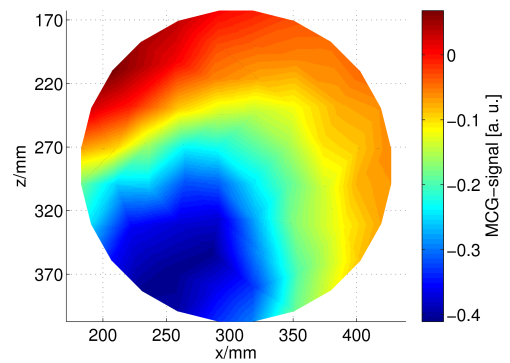


Figure 5.18: Subject 2 (male), sensor array *dorsal1*, MCG-signal at R-peak.

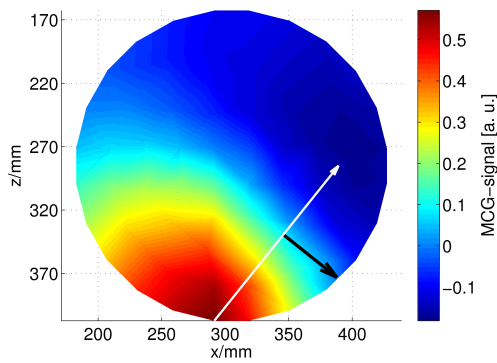


Figure 5.19: Subject 3 (female), sensor array *ventral1*, MCG-signal at R-peak, $\psi = -39^\circ$.

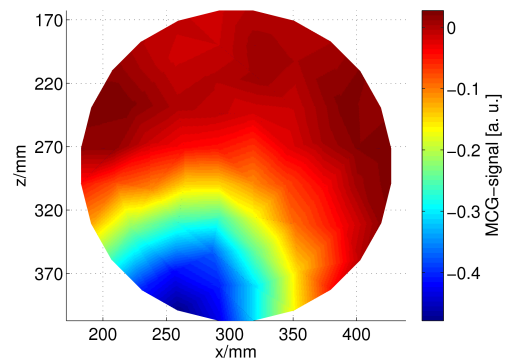


Figure 5.20: Subject 3 (female), sensor array *dorsal1*, MCG-signal at R-peak.

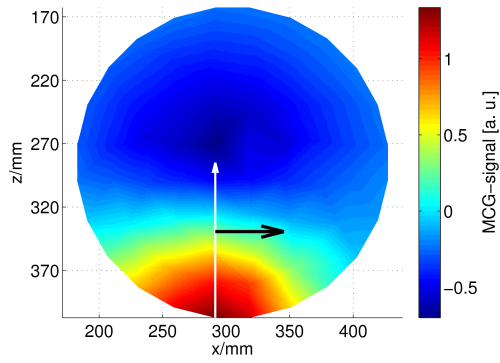


Figure 5.21: Subject 4 (female), sensor array *ventral1*, MCG-signal at R-peak, $\psi = 0^\circ$.

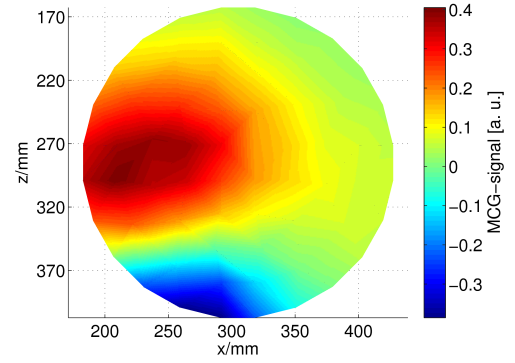


Figure 5.22: Subject 4 (female), sensor array *dorsal1*, MCG-signal at R-peak.

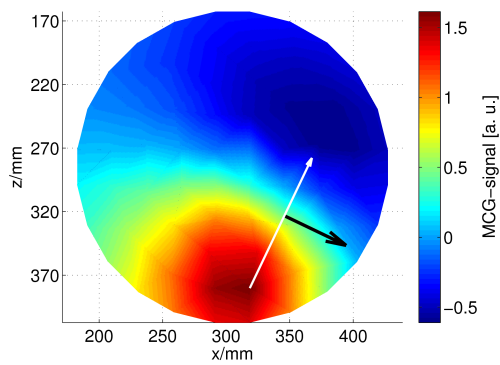


Figure 5.23: Subject 5 (male), sensor array *ventral1*, MCG-signal at R-peak, $\psi = -26^\circ$.

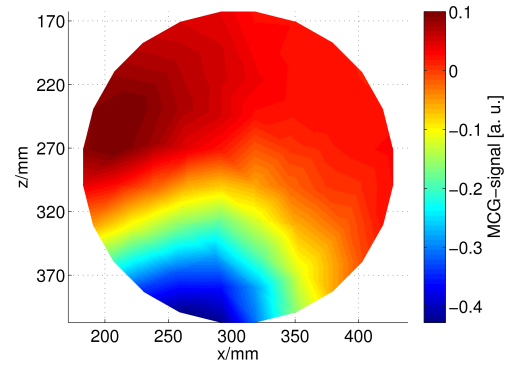


Figure 5.24: Subject 5 (male), sensor array *dorsal1*, MCG-signal at R-peak.

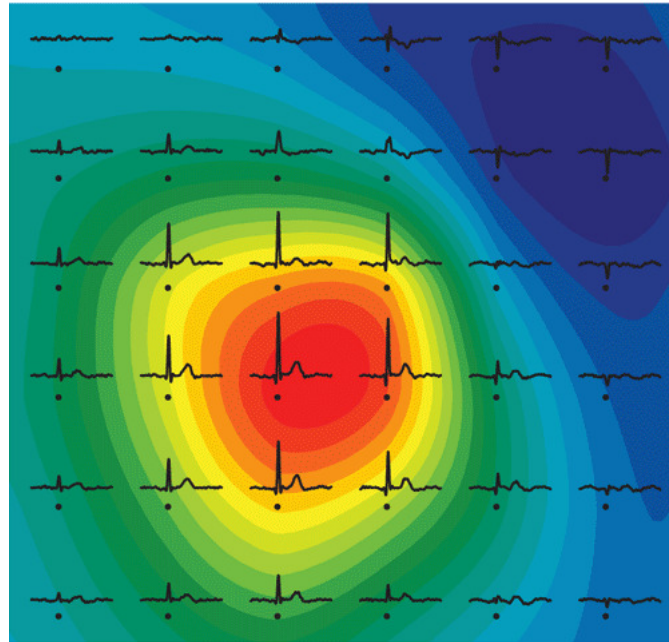


Figure 5.25: Out-of-chest component of the ventral magnetic field at the R-peak measured with atomic magnetometers [32]. The magnetic field is averaged over 100 heartbeats, the scale of the map ranges from -30 pT (blue) to $+60 \text{ pT}$ (red).

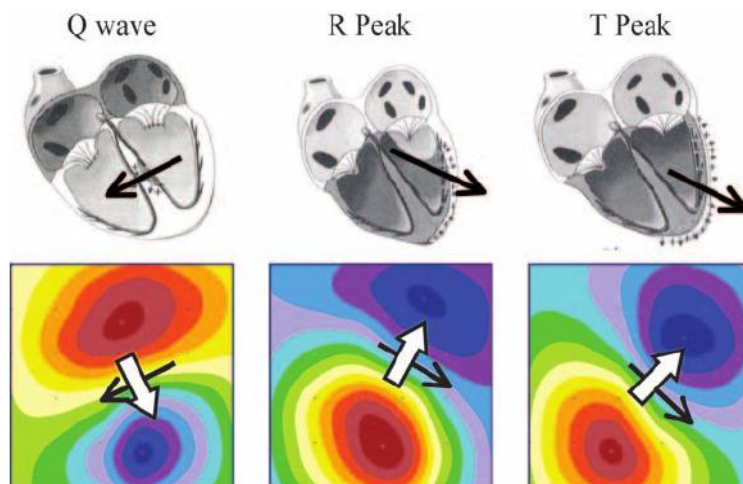


Figure 5.26: The direction of the electric axis in the heart (black arrow, top row) and the corresponding ventral magnetic field maps (bottom row) [33].

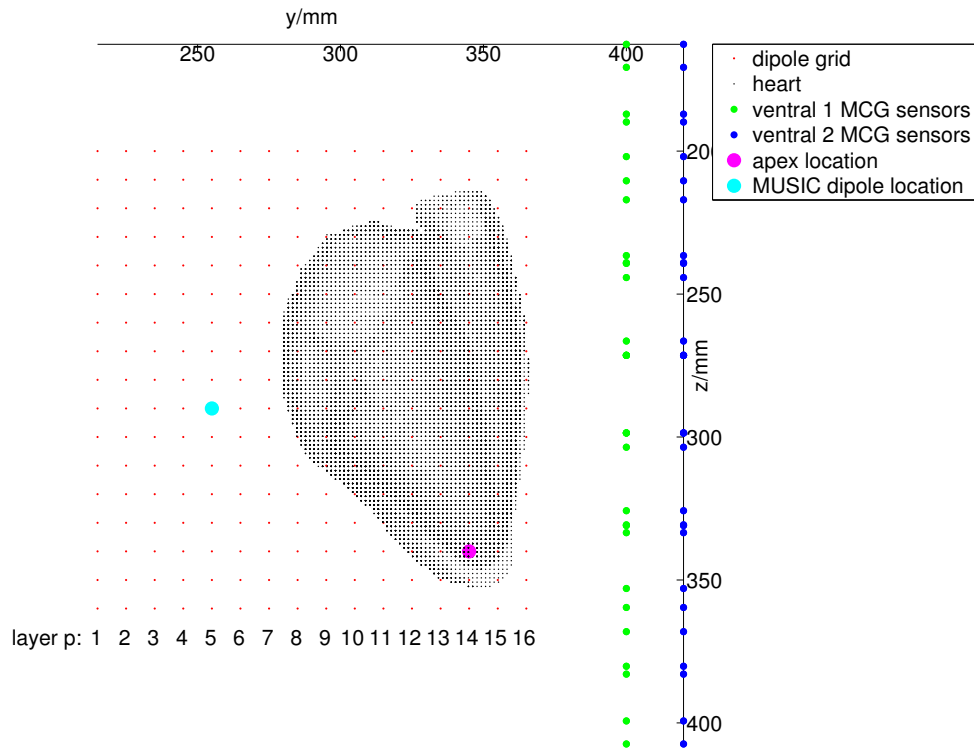


Figure 5.27: Side view of the sensor array *ventral1ventral2* (figure 5.2) with apex location $\vec{r}_{apex} = (335, 345, 340)mm$ and MUSIC dipole location estimated from R-peak data of subject 5.

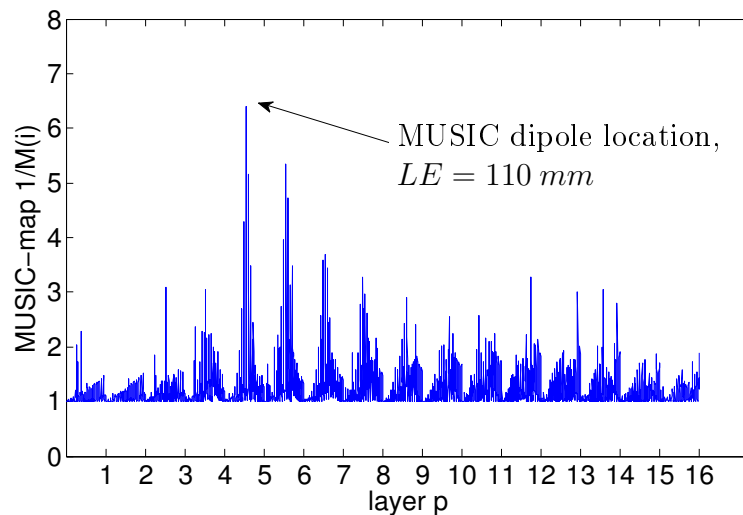


Figure 5.28: MUSIC map $1/M(i)$ of the sensor array *ventral1ventral2* (figure 5.2). The x -axis interval $[p - 1, p]$ includes all MUSIC amplitudes $1/M(i)$ of the layer p . $LE = 110 mm$ is the Localization Error between the apex and MUSIC dipole location estimated from R-peak data of subject 5.

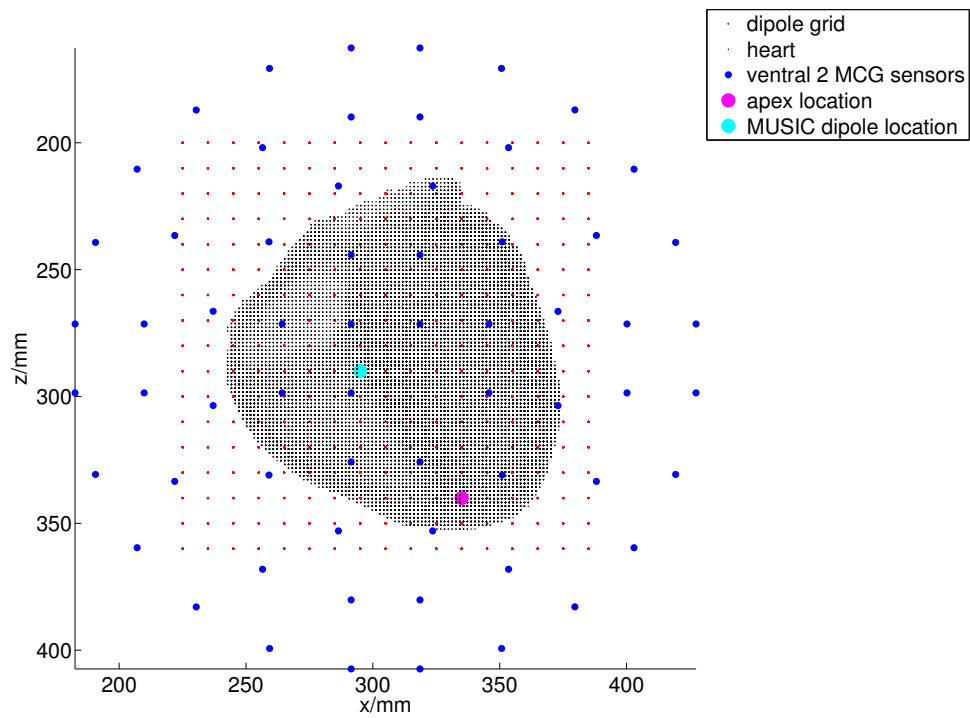


Figure 5.29: Front view of the sensor array *ventral1ventral2* (figure 5.2) with apex location $\vec{r}_{apex} = (335, 345, 340)mm$ and MUSIC dipole location estimated from R-peak data of subject 5.

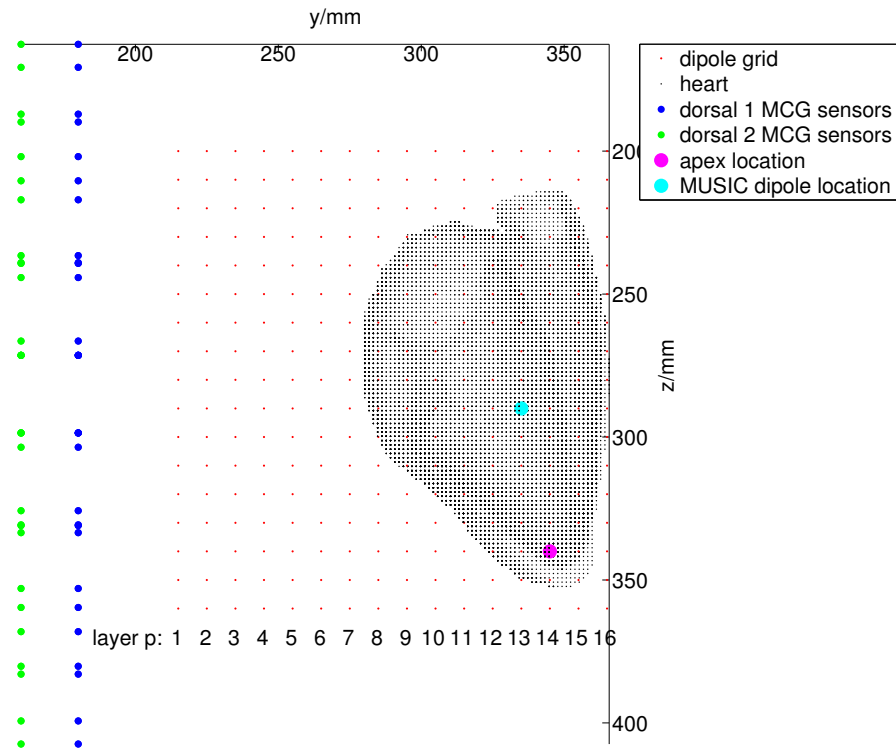


Figure 5.30: Side view of the sensor array *dorsal1dorsal2* (figure 5.2) with apex location $\vec{r}_{apex} = (335, 345, 340)mm$ and MUSIC dipole location estimated from R-peak data of subject 5.

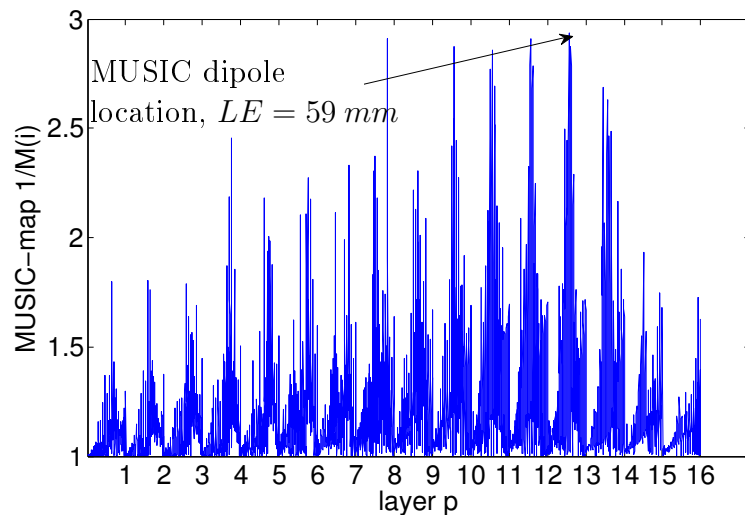


Figure 5.31: MUSIC map $1/M(i)$ of the sensor array *dorsal1dorsal2* (figure 5.2). The x -axis interval $[p - 1, p]$ includes all MUSIC amplitudes $1/M(i)$ of the layer p . $LE = 59 mm$ is the Localization Error between the apex and MUSIC dipole location estimated from R-peak data of subject 5.

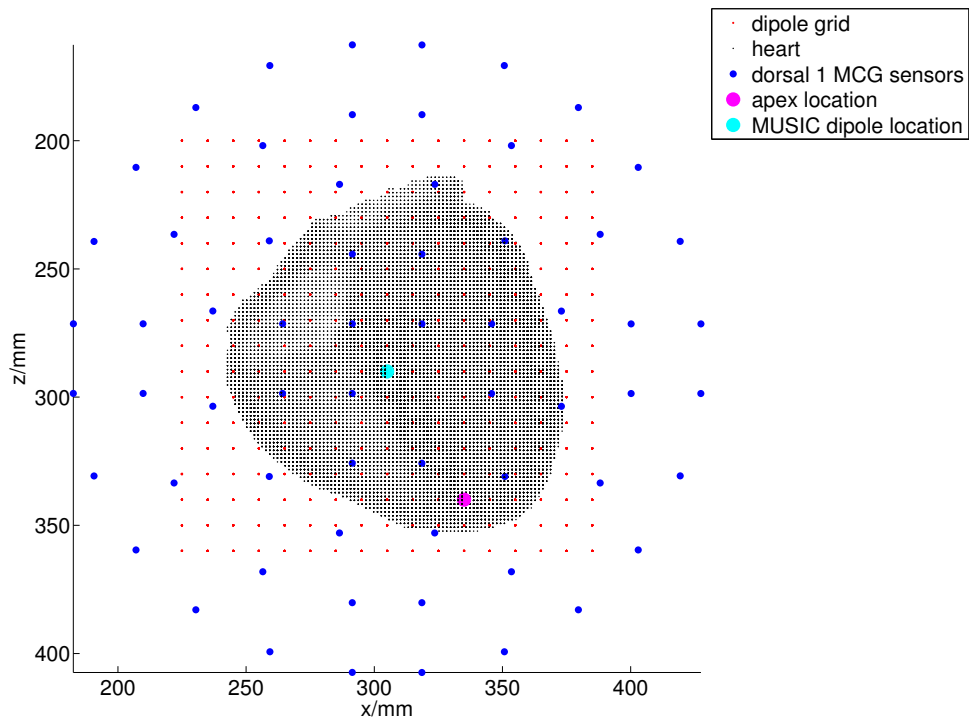


Figure 5.32: Front view of the sensor array *dorsal1dorsal2* (figure 5.2) with apex location $\vec{r}_{apex} = (335, 345, 340)mm$ and MUSIC dipole location estimated from R-peak data of subject 5.

The figures 5.27 to 5.29 show the MUSIC dipole localization for the R-peak data of subject 5 and the sensor array *ventral1ventral2* (double layer). Similar to the result for the theoretically simulated data (figure 5.4) the MUSIC dipole location is shifted into the posterior part of the torso. The Localization Error between the MUSIC dipole location and the apex location is $LE = 110 \text{ mm}$ (figure 5.28).

The figures 5.30 to 5.32 show the MUSIC dipole localization for the R-peak data of subject 5 and the sensor array *dorsal1dorsal2* (posterior double layer). In contrast to the theoretical result (figure 5.7) here a shift of the MUSIC dipole location away from the sensors in the direction of the anterior side of the thorax is not clearly visible. The Localization Error between the MUSIC dipole location and the apex location is $LE = 59 \text{ mm}$ (figure 5.31).

The figures 5.33 to 5.35 show the MUSIC dipole localization for the R-peak data of subject 5 and the sensor array *ventral1dorsal1*. Similar to the theoretical result (figure 5.10) a significant shift to the anterior or posterior side of the torso is not visible and the Localization Error between the MUSIC dipole location and the apex location $LE = 30 \text{ mm}$ (figure 5.34) is of the same order as the theoretical result ($LE = 28 \text{ mm}$).

The table 5.2 shows the Localization Errors for the R-peak data of the 5 subjects (LE_1 to LE_5) and the sensor arrays *ventral1ventral2*, *dorsal1dorsal2* and *ventral1dorsal1*. In comparison with the theoretical dipole localization results of table 5.1 there is a change in the order of the averaged Localization Errors, the averaged Localization Error of the sensor array *dorsal1dorsal2* is the smallest:

$$39.22 \text{ mm} = \overline{LE}_{dorsal1dorsal2} < \overline{LE}_{ventral1dorsal1} < \overline{LE}_{ventral1ventral2} = 123.90 \text{ mm}.$$

As can be seen for instance in figure 5.8 the MUSIC algorithm tends to shift the dipole location away from the sensors. Because the apex location is close to the anterior border of the dipole grid, this shift is not visible here. Another reason for the change of the order of the averaged Localization Errors might be differences in the positions of the patients with respect to the sensor arrays due to errors in the posture of the patients, visible for instance in the different heights of the magnetic field maps (e.g. figure 5.17 in comparison to 5.19) in z -direction. Because of the small spatial resolution of the dipole grid (10 mm), with a better alignment of the position of the patients and a higher number of patients the order of $\overline{LE}_{ventral1dorsal1}$ and $\overline{LE}_{dorsal1dorsal2}$ may again change.

In the next subsection there will be presented a second theoretical proof, that a sensor array with anterior and posterior sensors provides the smallest Localization Errors.

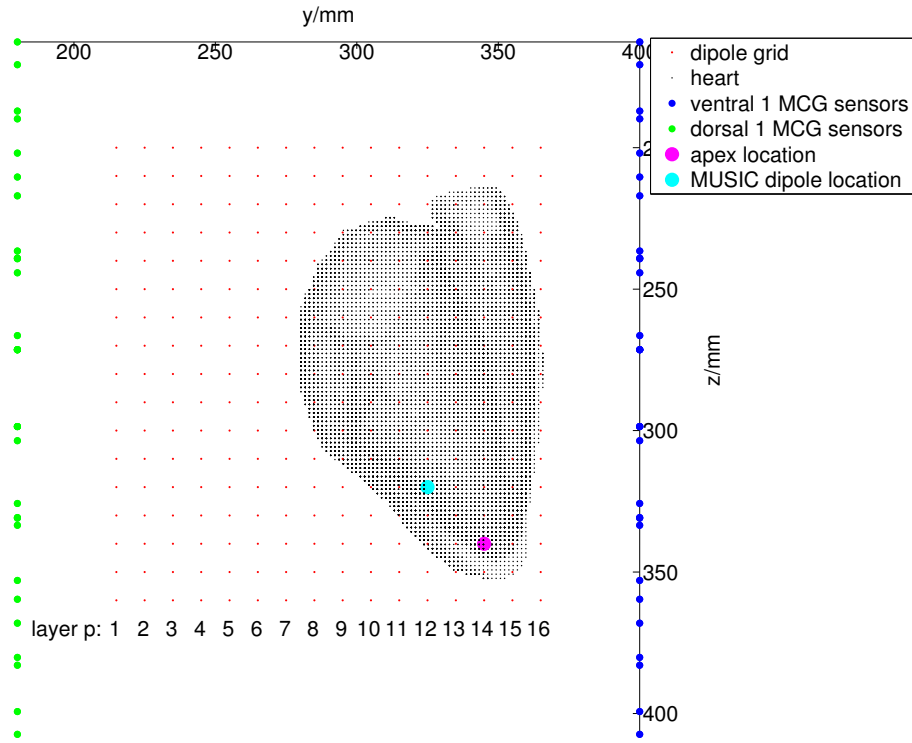


Figure 5.33: Side view of the sensor array *ventral1dorsal1* (figure 5.2) with apex location $\vec{r}_{apex} = (335, 345, 340)mm$ and MUSIC dipole location estimated from R-peak data of subject 5.

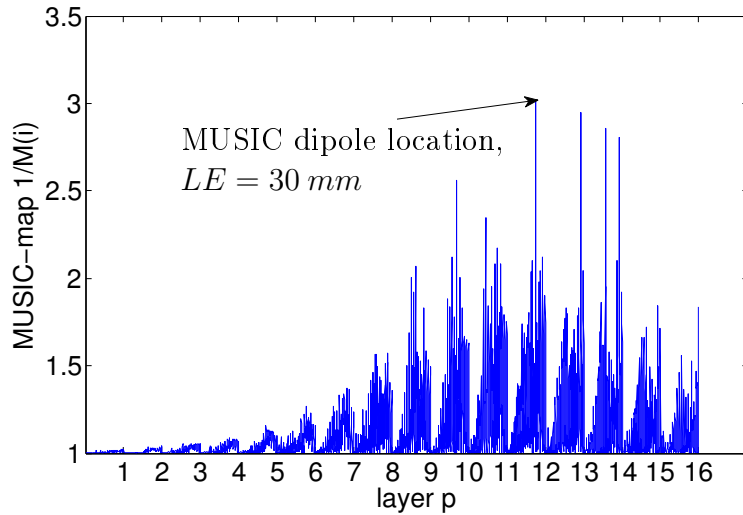


Figure 5.34: MUSIC map $1/M(i)$ of the sensor array *ventral1dorsal1* (figure 5.2). The x -axis interval $[p - 1, p]$ includes all MUSIC amplitudes $1/M(i)$ of the layer p . $LE = 30 mm$ is the Localization Error between the apex and MUSIC dipole location estimated from R-peak data of subject 5.

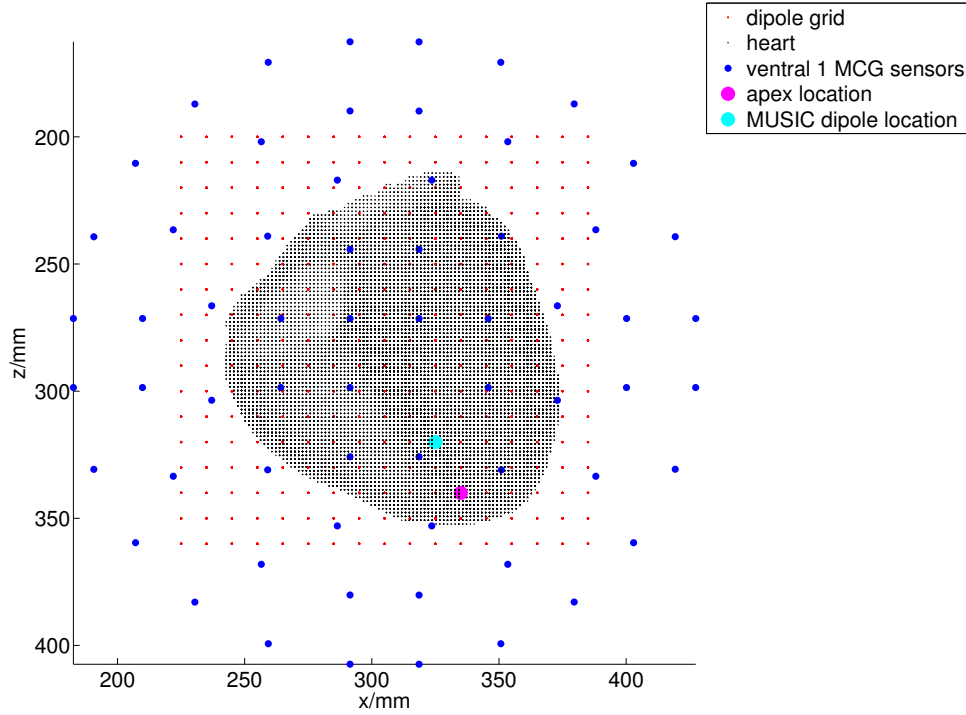


Figure 5.35: Front view of the sensor array *ventral1dorsal1* (figure 5.2) with apex location $\vec{r}_{apex} = (335, 345, 340)mm$ and MUSIC dipole location estimated from R-peak data of subject 5.

	$\frac{LE_1}{mm}$	$\frac{LE_2}{mm}$	$\frac{LE_3}{mm}$	$\frac{LE_4}{mm}$	$\frac{LE_5}{mm}$	$\frac{\overline{LE}}{mm}$	κ
<i>ventral1ventral2</i>	145.94	134.53	129.61	98.99	110.45	123.90	$1.3 \cdot 10^{11}$
<i>dorsal1dorsal2</i>	41.23	22.36	22.36	50.99	59.16	39.22	$1.2 \cdot 10^{11}$
<i>ventral1dorsal1</i>	53.85	24.49	102.96	61.64	30.00	54.59	$3.8 \cdot 10^9$

Table 5.2: Experimental Localization Errors LE , the distance between the apex location and MUSIC dipole location, for the 5 subjects and the sensor arrays *ventral1ventral2*, *dorsal1dorsal2* and *ventral1dorsal1*. \overline{LE} is the averaged LE and the last column shows the condition numbers $\kappa \equiv \text{cond}(\mathbf{L})$ of the leadfield matrices.

	\overline{LE}_x mm	\overline{LE}_y mm	\overline{LE}_z mm	\overline{LE} mm	$rank(\mathbf{L})$	$cond(\mathbf{L})$
<i>ventral1</i>	14.70	21.85	20.92	19.16	36	$7.1 \cdot 10^3$
<i>ventral1ventral4</i>	14.70	21.85	20.92	19.16	53	$1.2 \cdot 10^{13}$
<i>ventral1ventral2</i>	15.05	21.38	20.92	19.12	72	$1.4 \cdot 10^8$
<i>dorsal1dorsal2</i>	33.54	34.15	29.26	32.32	45	$1.0 \cdot 10^{13}$
<i>ventral1dorsal1</i>	13.30	19.37	17.18	16.62	72	$4.4 \cdot 10^5$

Table 5.3: Localization Errors LE , the distance between the true and MUSIC dipole location, for the sensor arrays *ventral1*, *ventral1ventral4*, *ventral1ventral2*, *dorsal1dorsal2* and *ventral1dorsal1*. \overline{LE}_i is the LE averaged over the 12 dipoles parallel to the i -axis, $\kappa \equiv cond(\mathbf{L})$ is the condition number of the leadfield matrices.

5.2 (6×6) -array simulations

In contrast to the last section the sensor arrays investigated in this section consist of several square (6×6) -arrays (figure 5.36). The radius of a magnetometer is $r = 9 \text{ mm}$ and the distance between the circle centers of two adjacent sensors in one layer is 3 cm . Analogous to the investigations in the last subsection four MCG sensor arrays will be compared: A double layer array with 2 square (6×6) -arrays on the ventral side of the torso and distance $D = 6 \text{ cm}$ between the layers (*ventral1ventral4*, figure 5.37), a double layer array with 2 square (6×6) -arrays on the ventral side of the torso and distance $D = 2 \text{ cm}$ between the layers (*ventral1ventral2*, figure 5.38) a double layer array with 2 square (6×6) -arrays on the dorsal side of the torso and distance $D = 2 \text{ cm}$ between the layers (*dorsal1dorsal2*, figure 5.39) and a sensor array with (6×6) sensors on the ventral and (6×6) sensors on the dorsal side of the torso (*ventral1dorsal1*, figure 5.40). For the positions of the primary current dipoles now the ventricular cubic grid with $n = 53476$ voxels (figure 3.4) will be used.

To compare the quality of the sensor arrays shown in the figures 5.37 to 5.40 first the $(m \times 3n)$ leadfield matrices \mathbf{L} for the $m = 72$ sensors and $n = 53476$ primary current dipoles in the ventricular grid have been calculated. Then the MCG signal vector $\boldsymbol{\varphi} = \mathbf{L}\mathbf{J}_p$ is calculated for single paraxial dipoles oriented in x -, y - and z -direction and located at the 12 uniformly distributed ventricular pacer locations shown in figure 6.1. In the next step the single dipoles are localized with the help of the MUSIC algorithm of the equations 5.1 to 5.3. Table 5.3 shows the Localization Errors LE between the given dipole location of figure 6.1 and the inversely estimated dipole locations, where \overline{LE}_x , \overline{LE}_y and \overline{LE}_z are the averaged Localization Errors for dipoles oriented in x -, y - and z -direction, respectively. The averaged Localization Error over the 12 dipole locations of figure 6.1 and all dipole orientations \overline{LE} is also shown in the bar graph of figure 5.41.

The result of the bar graph in figure 5.41 for the average LE using the $n = 53476$ ventricular dipole grid and the (6×6) -arrays is similar to the result of the bar graph in figure 5.13 for the average LE using the dipole grid with 1 cm lattice constant and the circular sensor arrays of the Biomagnetik Park system:

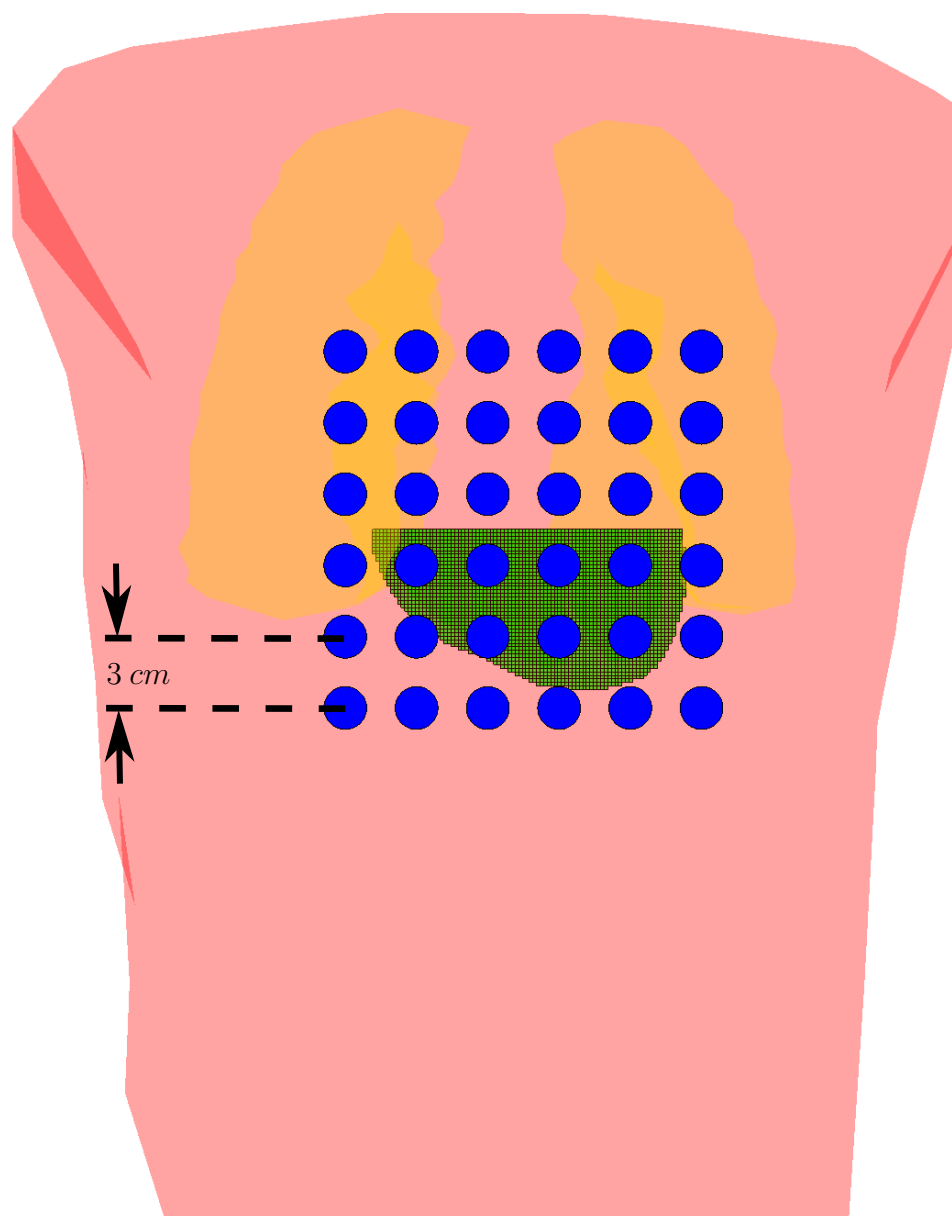


Figure 5.36: Square (6×6) -array, front view (radius of a sensor $r = 9 \text{ mm}$, minimum distance to torso = 1 cm , torso in red, lungs in yellow, ventricular grid in green).

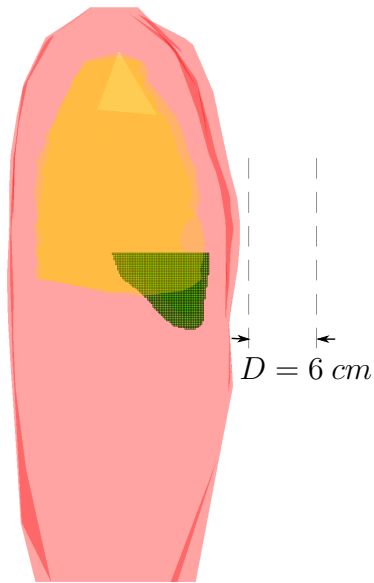


Figure 5.37: Sensor array $ventral1ventral4$, $cond(\mathbf{L}) = 1.2 \cdot 10^{13}$.

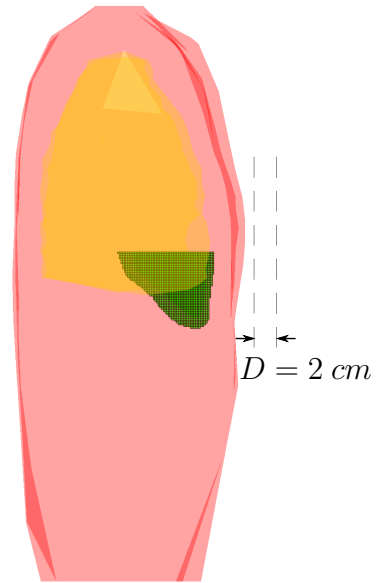


Figure 5.38: Sensor array $ventral1ventral2$, $cond(\mathbf{L}) = 1.4 \cdot 10^8$.

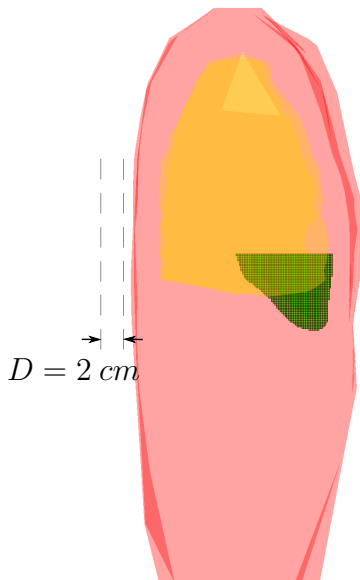


Figure 5.39: Sensor array $dorsal1dorsal2$, $cond(\mathbf{L}) = 1.0 \cdot 10^{13}$.

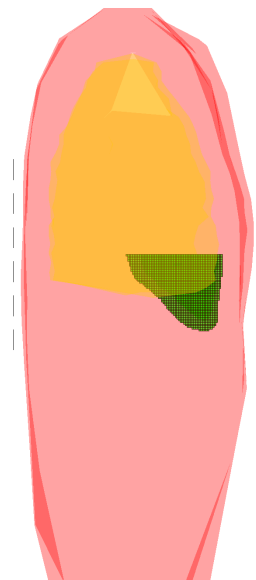


Figure 5.40: Sensor array $ventral1dorsal1$, $cond(\mathbf{L}) = 4.4 \cdot 10^5$.

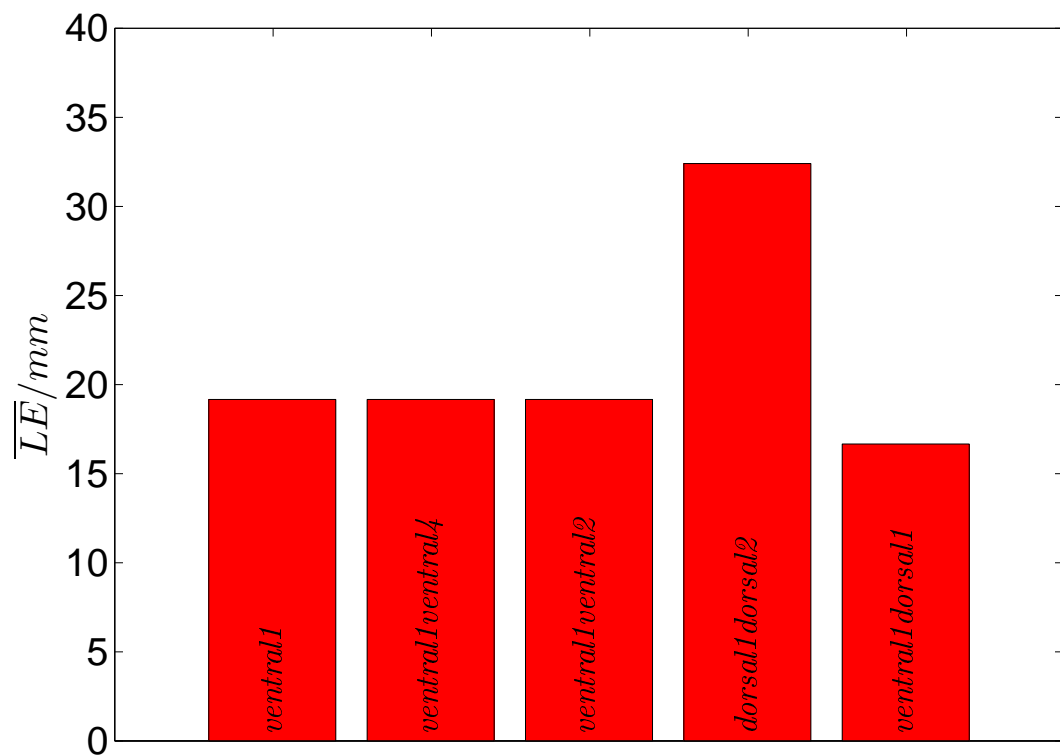


Figure 5.41: Localization Errors LE for the (6×6) sensor arrays averaged over the 12 ventricular pacer locations of figure 6.1 and the 3 paraxial dipole orientations.

In both cases the sensor array *ventral1dorsal1* with sensors on the anterior and posterior side of the body provides the smallest Localization Errors. Table 5.3 shows the following order of averaged Localization Errors for the (6×6) -arrays

$$\overline{LE}_{ventral1dorsal1} < \overline{LE}_{ventral1ventral2} < \overline{LE}_{ventral1ventral4} = \overline{LE}_{ventral1} < \overline{LE}_{dorsal1dorsal2}.$$

Analogous to the results of the circular sensor arrays the Localization Errors for the 6 cm double layer array *ventral1ventral4* and the single layer array *ventral1* are the same. Especially for a large distance D between the layers of the double layer the first layer *ventral1* is crucial for the localization because of the close proximity to the ventricles. In contrast to the results of the circular sensor arrays the (6×6) -array simulations reveal that the 2 cm double layer array *ventral1ventral2* provides smaller Localization Errors than the 6 cm double layer array *ventral1ventral4*. This may be due to the smaller lattice constant 1.5 mm in the (6×6) -array simulations compared to the lattice constant 1 cm in the simulations with the circular sensor array of the Biomagnetik Park system.

Because the dimension of the solution space of the system of linear equations $\varphi = \mathbf{L}\mathbf{J}_p$ is given by $dim = 3n - rank(\mathbf{L})$, the inverse solutions should be improved by increasing the rank of the leadfield matrix $rank(\mathbf{L})$. Table 5.3 shows that the only sensor arrays with maximum rank leadfield matrices *ventral1dorsal1* and *ventralventral2* (maximum of $rank(\mathbf{L}) = m = 2 \cdot 36 = 72$) indeed provide the smallest Localization Errors. As explained in subsection 5.1 a small condition number of the leadfield matrix is another clue for the high quality of a sensor array. So the smaller Localization Errors of the sensor array *ventral1dorsal1* compared to the double layer array *ventral1ventral2* can be explained by the order of the corresponding condition numbers (table 5.3)

$$cond(\mathbf{L}_{ventral1dorsal1}) < cond(\mathbf{L}_{ventral1ventral2}).$$

Because the sensor array *ventral1dorsal1* with (6×6) sensors on the anterior and (6×6) sensors on the posterior side of the torso (figure 5.40) provides the smallest MUSIC Localization Errors it will be used in the simulations of the central chapter 6.

Chapter 6

Inverse problem of Magnetocardiography

6.1 Generation of initial states

Because the Kalman Filters developed in chapter 6.2 are recursive algorithms, they need an initial guess for the activation time state vector $\mathbf{x}_{k=0}$ of the first iteration step $k = 0$ of the Kalman Filter. In this thesis the Weighted Minimum Norm (WMN) and the Multiple Signal Classification (MUSIC) are used for the purpose of generating the initial state. In the WMN approach the initial activation times are estimated from the maximum amounts of the WMN-estimated primary current dipoles, in the MUSIC approach first the location of the accessory pathway is estimated and then the initial activation times are simulated using the cellular automaton model. To make the most of the advantages of both imaging techniques a WMN-MUSIC hybrid technique is also investigated.

To quantify the quality of an inverse solution the Localization Error (LE) of the accessory pathway and the Relative Error (RE) of the activation time state vector \mathbf{x} are introduced. The Relative Error is defined as the normalized distance between

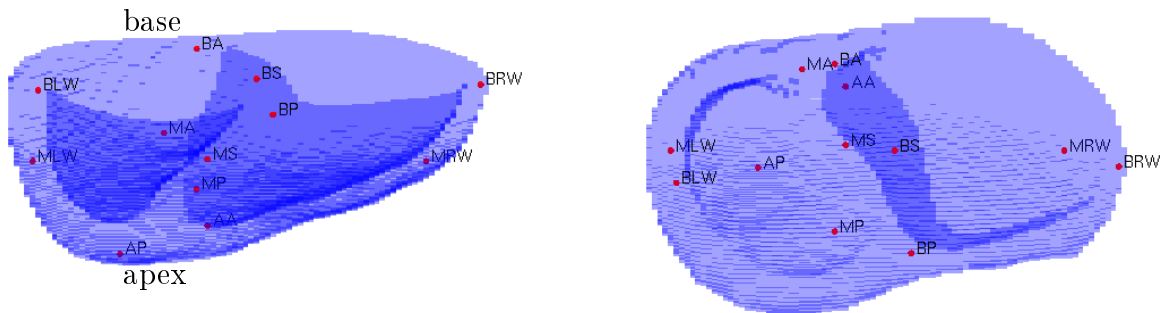


Figure 6.1: The forward and inverse simulations in this work are tested for the following 12 pacer locations in the ventricles from base to apex: BA (Basal-anterior), BRW (Basal-right-wall), BP (Basal-posterior), BLW (Basal-left-wall), BS (Basal-septum), MA (Mid-anterior), MRW (Mid-right-wall), MP (Mid-posterior), MLW (Mid-left-wall), MS (Mid-septum), AA (Apical-anterior), AP (Apical-posterior).

the true activation times \mathbf{x}_{true} and the activation times \mathbf{x} of the inverse solution

$$RE = \frac{\|\mathbf{x} - \mathbf{x}_{true}\|}{\|\mathbf{x}_{true}\|} \quad (6.1)$$

with the euclidian norm $\|\cdot\|$. In order to get a stable convergence of the Localization Error, it is defined with a center of mass around the minimum of the inversely estimated activation times \mathbf{x} : Let $\vec{r}_{min,center}(\mathbf{x})$ be the center of mass of a small time interval $\Delta t = 12 \text{ ms}$ above the minimum of the estimated activation times \mathbf{x} and let $\vec{r}_{min}(\mathbf{x}_{true})$ be the location of the minimum of the true activation times \mathbf{x}_{true} . Then the Localization Error (LE) is defined as the distance between the minimum of the true activation times and the center-of-mass-minimum of the estimated activation times

$$LE = \|\vec{r}_{min}(\mathbf{x}_{true}) - \vec{r}_{min,center}(\mathbf{x})\|. \quad (6.2)$$

The use of this center-of-mass-minimum generates in many cases smaller Localization Errors (figure 6.2) and stabilizes its convergence. Figure 6.3 shows that the Localization Error LE decreases with the center-of-mass time interval Δt for all imaging techniques investigated in the next three sections. The forward and inverse simulations in this work have been tested for the 12 ventricular pacer locations shown in figure 6.1. The basal pacer locations could represent the locations of accessory pathways, the mid and apical pacer locations could be the origins in focal ventricular tachycardia.

6.1.1 Weighted Minimum Norm (WMN)

The amount of the primary current density $\vec{j}_p(\vec{r}_k, t) = -\sigma_{int} \nabla V_m(\vec{r}_k, t)$ of a voxel at position \vec{r}_k has a maximum at the time t of maximal spatial slope of the transmembrane potential V_m . Because the spatial slope of the transmembrane potential V_m has a spike inside the depolarization wavefront (figure 3.3), the depolarization time $\tau(\vec{r}_k)$ of the voxel can be estimated to [34]

$$\tau(\vec{r}_k) = \arg \max_{t \in \{t_1, \dots, t_N\}} \left(\left| \vec{j}_p(\vec{r}_k, t) \right| \right). \quad (6.3)$$

In [34] some different WMN methods for estimating the primary current dipoles $\vec{j}_p(\vec{r}_k, t)$ from the measured data have been compared. Here only the Truncated Singular Value Decomposition (TSVD) method that results in the smallest Relative Errors and Localization Errors of [34] is presented and used for the WMN solutions. The Singular Value Decomposition (SVD) of the measured data matrix $\Phi = (\varphi(t_1), \dots, \varphi(t_N))$ can be written as

$$\Phi = \mathbf{U} \Sigma \mathbf{V}^T = \sum_{k=1}^{\min(N,m)} \mathbf{u}_k \sigma_k \mathbf{v}_k^T \quad (6.4)$$

with the $(m \times 1)$ -vectors \mathbf{u}_k , the $(N \times 1)$ -vectors \mathbf{v}_k and the corresponding singular values σ_k . The spatial components with $k \geq P$ that do not fulfil the discrete Picard condition [35] are dominated by noise perturbations, thereby they are trun-

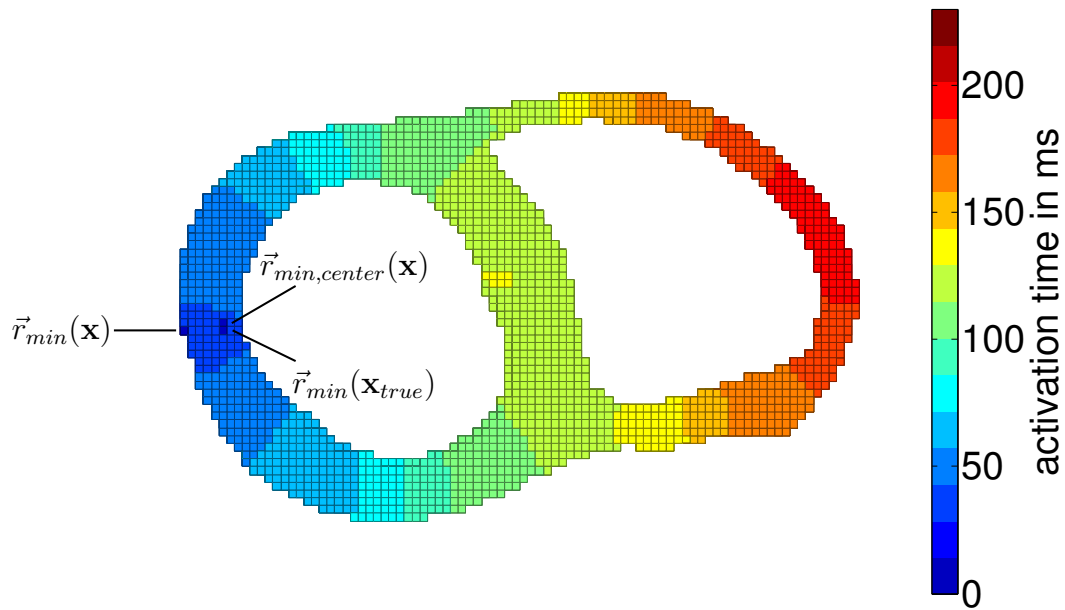


Figure 6.2: The center-of-mass-minimum $\vec{r}_{min,center}(\mathbf{x})$ of the estimated activation times is closer to the minimum $\vec{r}_{min}(\mathbf{x}_{true})$ of the true activation times than the minimum $\vec{r}_{min}(\mathbf{x})$ of the estimated activation times (figure 6.5).

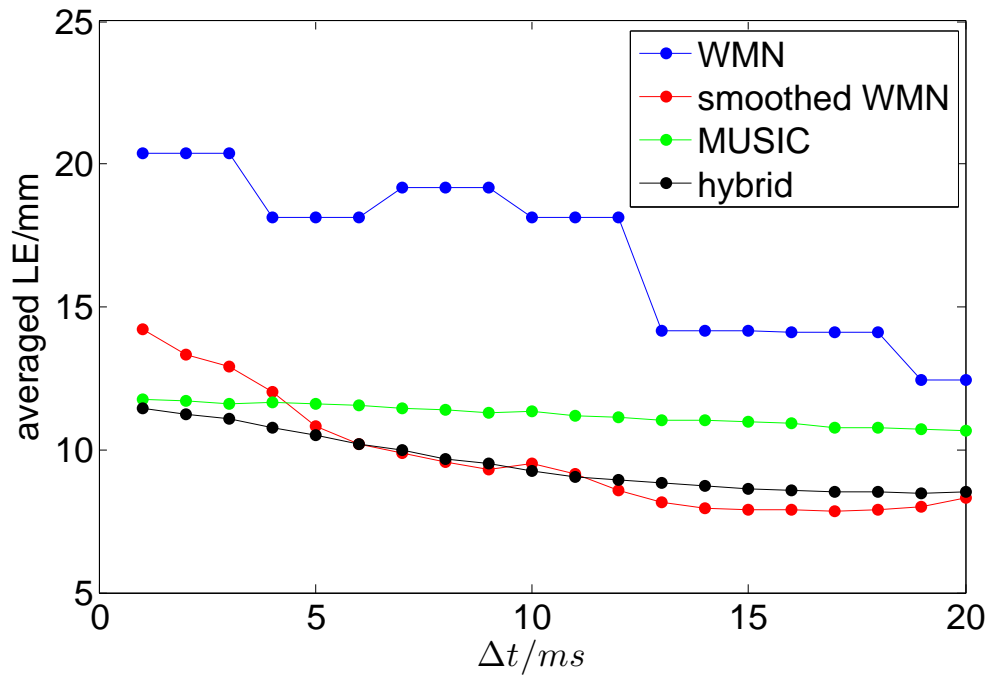


Figure 6.3: Localization Error LE averaged over the 12 pacer locations of figure 6.1 as a function of the center-of-mass time interval Δt .

cated in the TSVD. Then the $(3n \times N)$ -matrix $\hat{\mathbf{J}} = (\hat{\mathbf{J}}_p(t_1), \dots, \hat{\mathbf{J}}_p(t_N))$, including the estimations of the primary currents (equation (1.2)) of the data time samples t_1, \dots, t_N , can be obtained by

$$\hat{\mathbf{J}} = \sum_{k=1}^P \hat{\mathbf{J}}_k \sigma_k \mathbf{v}_k. \quad (6.5)$$

Here $\hat{\mathbf{J}}_k$ is the solution of the Tikhonov regularized minimization problem

$$\hat{\mathbf{J}}_k = \arg \min_{\mathbf{J}} (||\mathbf{u}_k - \mathbf{LJ}||^2 + \lambda_k ||\mathbf{J}||^2) = \mathbf{H}(\lambda_k) \mathbf{u}_k \quad (6.6)$$

where $\mathbf{H}(\lambda_k)$ is the kernel matrix¹

$$\mathbf{H}(\lambda_k) = \mathbf{L}^T (\mathbf{L}\mathbf{L}^T + \lambda_k \mathbf{I})^{-1} \quad (6.7)$$

and the regularization parameter λ_k is obtained by the L-curve approach [37]: $\lambda_k = \lambda(\mathbf{u}_k)$.

Figure 6.4 shows the WMN activation times $\tau(\vec{r}_k)$ of the pacer location BLW derived with the equations (6.3) to (6.7) using the 72 sensor MCG array *ventral1dorsal1* and torso model of subsection 5.2 (figure 5.40). Because of the non-uniqueness of the inverse problem (the leadfield-matrix \mathbf{L} is a $(72 \times 3 \cdot 53476)$ -matrix) there are significant errors in the estimated primary current dipoles $\vec{j}_p(\vec{r}_k)$ that generate significant errors in the activation time map. In figure 6.4 these errors in the activation time map can be identified as outliers (e.g. black arrow). Because the measurement function $\mathbf{h}(\mathbf{x})$ is proportional to the gradient of the activation times $\mathbf{h}(\mathbf{x}) \sim \nabla \tau(\vec{r}_k)$ (equation (4.22)) those outliers produce large relative errors in the simulated MCG signal

$$RE_{signal} = ||\mathbf{h}(\mathbf{x}) - \phi|| / ||\phi|| \quad (6.8)$$

making the convergence in the following Kalman Filter calculations unstable. To get rid of the outliers in the estimated activation times \mathbf{x} a smoothing process function $\mathbf{f}(\mathbf{x})$ is introduced, whose j -th component is defined by

$$f^j(\mathbf{x}) = \begin{cases} x^j, & \text{if } \left| x^j - \frac{1}{Z} \sum_{n=1}^Z x^{i_n} \right| \leq \varepsilon \\ \frac{1}{Z} \sum_{n=1}^Z x^{i_n}, & \text{if } \left| x^j - \frac{1}{Z} \sum_{n=1}^Z x^{i_n} \right| > \varepsilon \end{cases} \quad (6.9)$$

where Z is the number of next neighbors ($i_n; n = 1, \dots, Z$) within a distance \bar{d} . Consequently, the activation time of a voxel tends to the average activation time of the adjacent voxels which has a smoothing effect on the activation times \mathbf{x} . The smoothed WMN activation times of figure 6.5 are calculated from the WMN

¹proof e.g. in the appendix of [36]. Here the weighting matrix of [34] is set to be the unity matrix $\mathbf{W} = \mathbf{I}$.

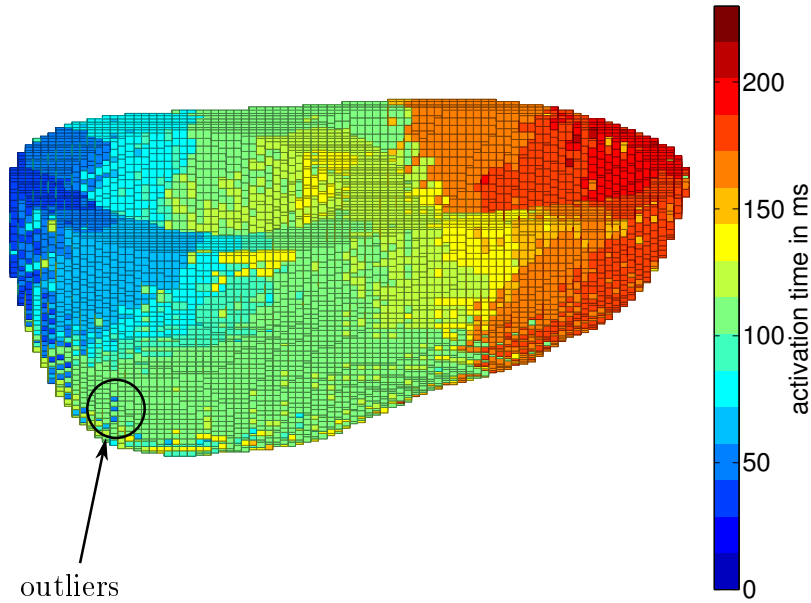


Figure 6.4: WMN activation times of the pacer location BLW ($SNR = 8.66 \times 10^3$, truncation at $P = 50$, $RE = 0.137$, $RE_{signal} = 0.900$, $LE = 4.8 \text{ mm}$).

activation times of figure 6.4 with the recursive algorithm

$$\mathbf{x}_k = \mathbf{f}(\mathbf{x}_{k-1}) \quad k = 1, 2, 3, \dots \quad (6.10)$$

until RE_{signal} is minimized. The smoothing with the recursive algorithm (6.10) will be explained in detail in the appendix B. The appendix A explains how the noise in the data is simulated and how the Signal to Noise Ratio (SNR) is defined. The Relative Errors show that the smoothed WMN activation times are closer to the corresponding simulated (=true) activation times of the pacer location BLW which is shown in figure 6.6. Parameter tests for ε and \bar{d} shown in the appendix C reveal optimal values of $\varepsilon = 0.001$ and $\bar{d} = 5.25 \text{ mm}$ with the fastest convergence and smallest RE .

6.1.2 Multiple Signal Classification (MUSIC)

In this chapter the localization of pacers (e.g. accessory pathways) in the heart with the help of the MUSIC algorithm [30] will be discussed. The basic idea of the MUSIC algorithm is to replace the primary current dipoles inside the depolarization wavefront by one single dipole for each pacer. The MUSIC algorithm will only produce good localization results if the data matrix is restricted to a small time interval $\overline{\Delta t}$ after the onset of the pacer. Because of the finite conduction velocities of table 2.1 the depolarization wavefront within a time interval of $\overline{\Delta t} = 12 \text{ ms}$ will be located in a distance of $\overline{\Delta t} \cdot v_{\parallel} = 9.6 \text{ mm}$ to the pacer, which makes the single dipole

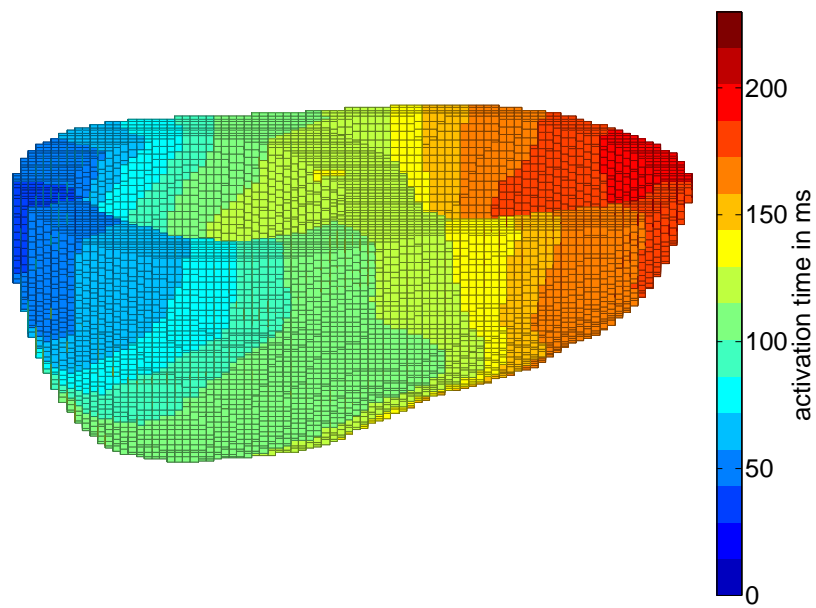


Figure 6.5: Smoothed WMN activation times of the pacer location BLW ($\varepsilon = 0.001$, $\bar{d} = 5.25 \text{ mm}$, $RE = 0.112$, $RE_{signal} = 0.302$, $LE = 4.9 \text{ mm}$).

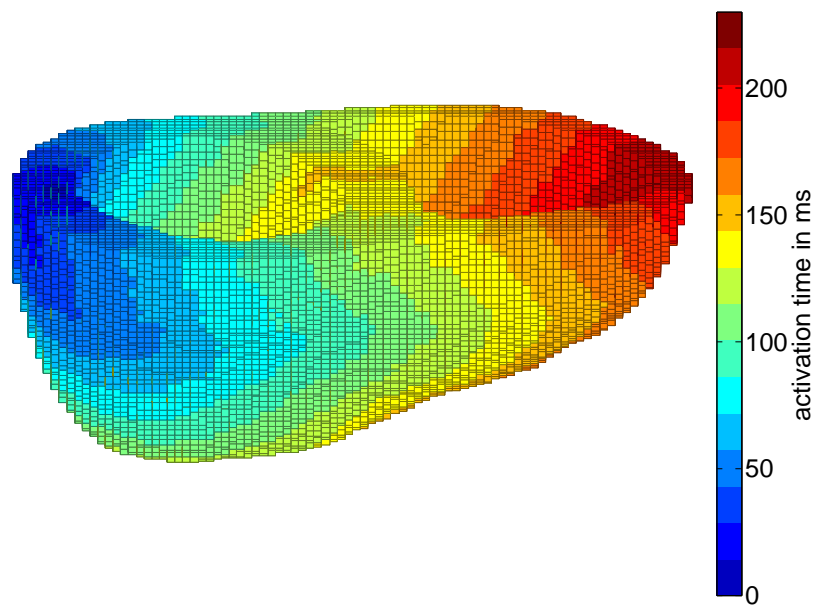


Figure 6.6: True (=simulated) activation times of the pacer location BLW.

approximation reasonable. Let r be the number of simultaneously active pacers and $\overline{\Phi}$ the part of the data matrix corresponding to the initial time interval $\overline{\Delta t}$. With the help of the SVD of the initial data matrix

$$\overline{\Phi} = \overline{\mathbf{U}}\overline{\Sigma}\overline{\mathbf{V}}^T \quad (6.11)$$

we can define an orthogonal projector to the noise subspace

$$\mathbf{P}^\perp = \overline{\mathbf{U}}_{m-r}\overline{\mathbf{U}}_{m-r}^T \quad (6.12)$$

where $\overline{\mathbf{U}}_{m-r}$ contains the column vectors of $\overline{\mathbf{U}}$ corresponding to the $m-r$ smallest singular values. \mathbf{P}^\perp is inserted into the MUSIC scanning function $M(i)$ (equation (5.3)) and the r active pacers can be found by plotting the MUSIC map $1/M(i)$ at all dipole locations and looking for r sharp peaks. Once the pacer locations have been estimated with the MUSIC algorithm, the corresponding MUSIC activation times are calculated using the anisotropic cellular automaton model developed in chapter 3.2. Figure 6.7 shows the MUSIC activation times of the pacer location BLW. In comparison with the smoothed WMN activation times of figure 6.5 one can see that the distance between wavefronts is better estimated with the MUSIC algorithm, especially in the septal regions, because the MUSIC algorithm includes information of the anisotropic wavefront velocity in the inverse calculation.

To find an optimal value for the initial time interval $\overline{\Delta t}$ the Localization Errors LE have been calculated for the 12 pacer locations depicted in figure 6.1 and for different values of $\overline{\Delta t}$. Figure 6.8 shows the Localization Error averaged over the 12 pacer locations as a function of the initial time interval $\overline{\Delta t}$ the data matrix is restricted to. The optimal initial time interval of $\overline{\Delta t} = 12 \text{ ms}$ with the smallest averaged LE will be used for all further calculations with the MUSIC algorithm.

6.1.3 WMN-MUSIC hybrid technique

While the MUSIC algorithm only uses the first part of the data matrix corresponding to the initial time interval $\overline{\Delta t}$ for the estimation of the pacer location, the WMN technique makes use of the full data matrix. On the other hand the advantage of the MUSIC estimation of the activation times is that the physiological information (muscle fiber directions, anisotropic wavefront velocities) is used in the second cellular automaton step. To make use of the benefits of both techniques in this work also a new inverse approach will be investigated: We define the WMN-MUSIC hybrid activation times by the arithmetic mean

$$\mathbf{x}_{\text{hybrid}} = \frac{1}{2}(\mathbf{x}_{\text{smoothed WMN}} + \mathbf{x}_{\text{MUSIC}}) \quad (6.13)$$

where the smoothed WMN activations times $\mathbf{x}_{\text{smoothed WMN}}$ and the MUSIC activation times $\mathbf{x}_{\text{MUSIC}}$ are used. The WMN-MUSIC hybrid activation times of the pacer location BLW are shown in figure 6.9.

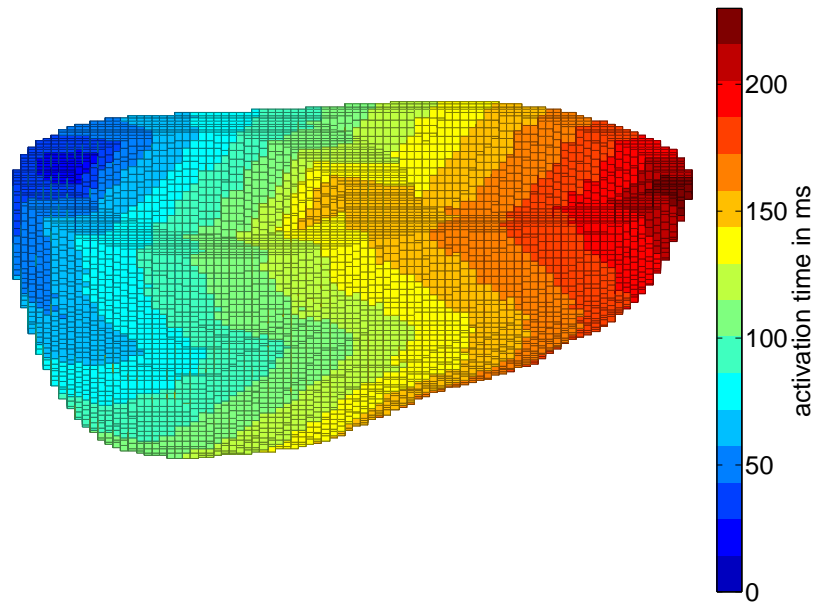


Figure 6.7: MUSIC activation times of the pacer location BLW ($\overline{\Delta t} = 12 \text{ ms}$, $RE = 0.138$, $RE_{signal} = 0.294$, $LE = 14.9 \text{ mm}$).

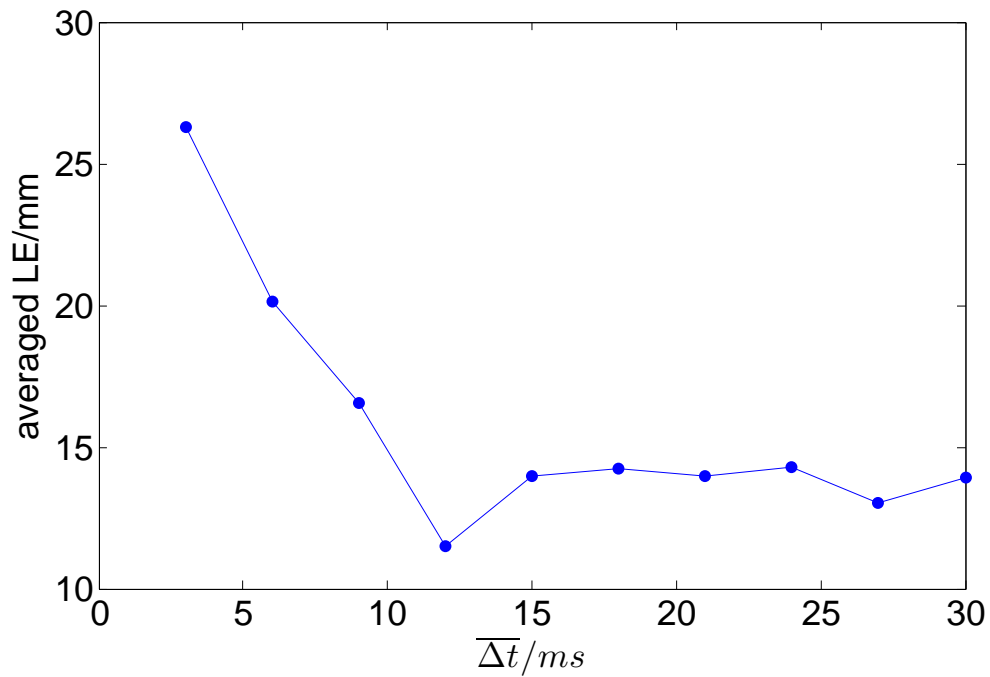


Figure 6.8: MUSIC Localization Error LE averaged over the 12 pacer locations of figure 6.1 as a function of the initial time interval $\overline{\Delta t}$.

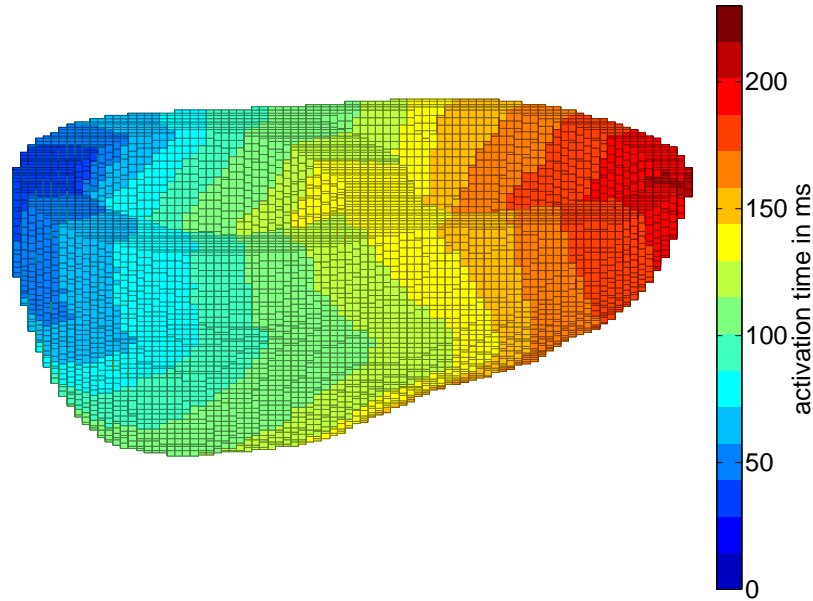


Figure 6.9: Hybrid WMN-MUSIC activation times of the pacer location BLW ($\overline{\Delta t} = 12 \text{ ms}$, $RE = 0.103$, $RE_{signal} = 0.197$, $LE = 9.8 \text{ mm}$).

6.1.4 Comparison of the reconstructed activation times for single pacers

In this section the activation times of the 12 pacer locations in figure 6.1 are compared for the four imaging techniques WMN, smoothed WMN, MUSIC and WMN-MUSIC hybrid, which were discussed in the last three sections. Table 6.1 shows the Relative Error RE for every single pacer location and in the last line RE averaged over the 12 pacer locations. The smallest averaged RE can be achieved with the WMN-MUSIC hybrid technique (in bold print). One can also figure out that averaged over all pacer locations the MUSIC technique is superior to the smoothed WMN and WMN technique in estimating RE . The MUSIC technique of estimating the activation times includes the physiological information of the cellular automaton (e.g. wavefront velocities). The WMN algorithm only uses the information of the data and noise, so the estimation of the distance between wavefronts is worse compared to the MUSIC technique (e.g. septal regions in figure 6.5). The global estimation of the activation times works best with the WMN-MUSIC hybrid technique. It combines the advantages of the MUSIC technique (cellular automaton information) and the WMN technique (use of the full data matrix).

Table 6.2 shows the Relative Error for the measured MCG signal calculated with equation (6.8). The WMN-MUSIC hybrid technique also results in the smallest averaged RE_{signal} and the (non-smoothed) WMN technique produces the biggest

	WMN	smoothed WMN	MUSIC	WMN-MUSIC hybrid
BLW	0.137	0.112	0.138	0.103
BRW	0.109	0.081	0.050	0.049
BP	0.166	0.138	0.077	0.089
BA	0.202	0.187	0.073	0.102
BS	0.182	0.165	0.227	0.136
MLW	0.153	0.133	0.155	0.119
MRW	0.166	0.144	0.141	0.120
MP	0.229	0.216	0.171	0.155
MA	0.225	0.201	0.145	0.125
MS	0.271	0.256	0.118	0.151
AA	0.199	0.174	0.098	0.094
AP	0.201	0.175	0.089	0.101
averaged	0.187	0.165	0.124	0.112

Table 6.1: Relative Errors (RE) for the 12 pacer locations of figure 6.1. The last line shows the RE averaged over the 12 pacer locations. The smallest averaged RE is in bold print.

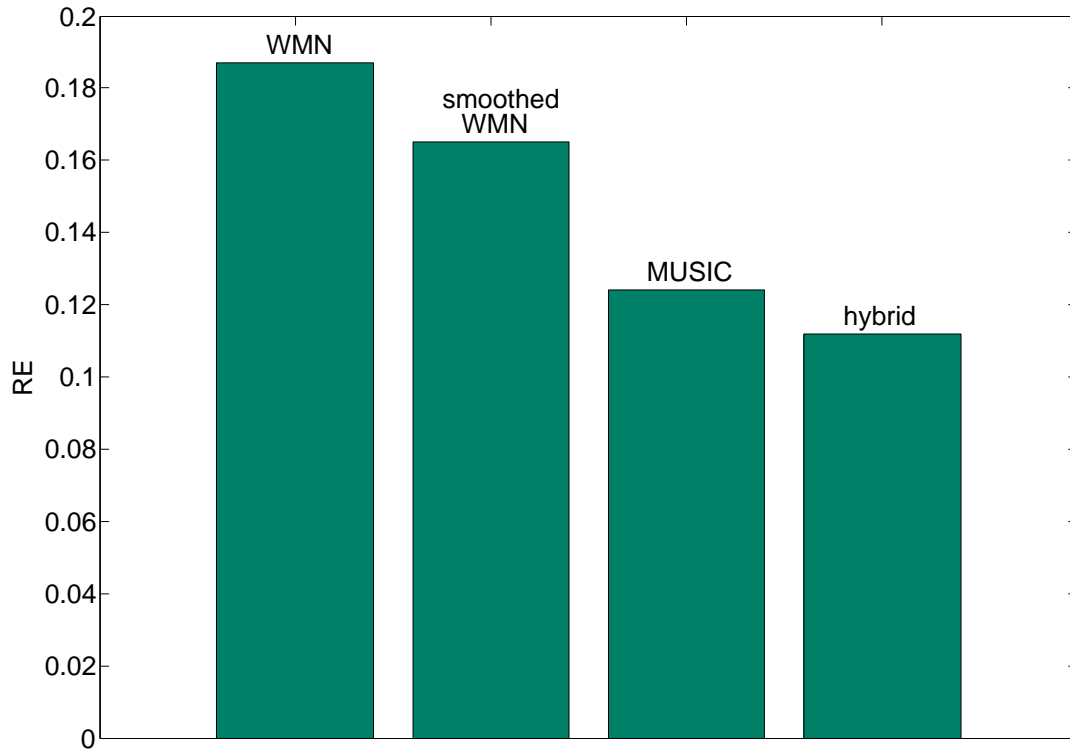


Figure 6.10: RE of the initial states averaged over the 12 pacer locations ($SNR = 8.66 \times 10^3$, $\bar{d} = 5.25$ mm, $\varepsilon = 0.001$).

	WMN	smoothed WMN	MUSIC	WMN-MUSIC hybrid
BLW	0.900	0.302	0.294	0.197
BRW	0.932	0.305	0.231	0.205
BP	1.068	0.453	0.308	0.215
BA	0.973	0.445	0.268	0.330
BS	0.879	0.418	0.883	0.627
MLW	0.873	0.363	0.420	0.309
MRW	0.824	0.403	0.324	0.319
MP	1.309	0.829	0.727	0.620
MA	1.806	0.573	0.934	0.657
MS	1.142	0.513	0.717	0.527
AA	1.276	0.365	0.338	0.283
AP	0.845	0.351	0.311	0.281
averaged	1.069	0.443	0.519	0.381

Table 6.2: Relative Errors of the MCG signal (RE_{signal}) for the 12 pacer locations of figure 6.1. The last line shows the RE_{signal} averaged over the 12 pacer locations. The smallest averaged RE_{signal} is in bold print.

RE_{signal} . The nonlinearity of the function $\mathbf{h}(\mathbf{x})$ can be seen in the order of the smoothed WMN and the MUSIC method: although the averaged RE of the MUSIC method (0.124) is smaller than the averaged RE of the smoothed WMN method (0.165), the averaged RE_{signal} of the MUSIC method (0.519) is bigger than the the averaged RE_{signal} of the smoothed WMN method (0.443).

Table 6.3 shows the Localization Error LE for every single pacer location and in the last line LE averaged over the 12 pacer locations. The smoothed WMN technique results in the smallest averaged LE (in bold print). This section can only give a clue on finding the best initial state for the Kalman Filters: Because the initial state of the Kalman Filters in section 6.2 is the global activation time state vector $\mathbf{x}_{k=0}$, the smoothed WMN technique doesn't necessarily need to be the best initial state generator for the localization of accessory pathways. To find out the best technique for generating the initial states one has to look at the Localization Errors of the converged Kalman Filter results in section 6.2.

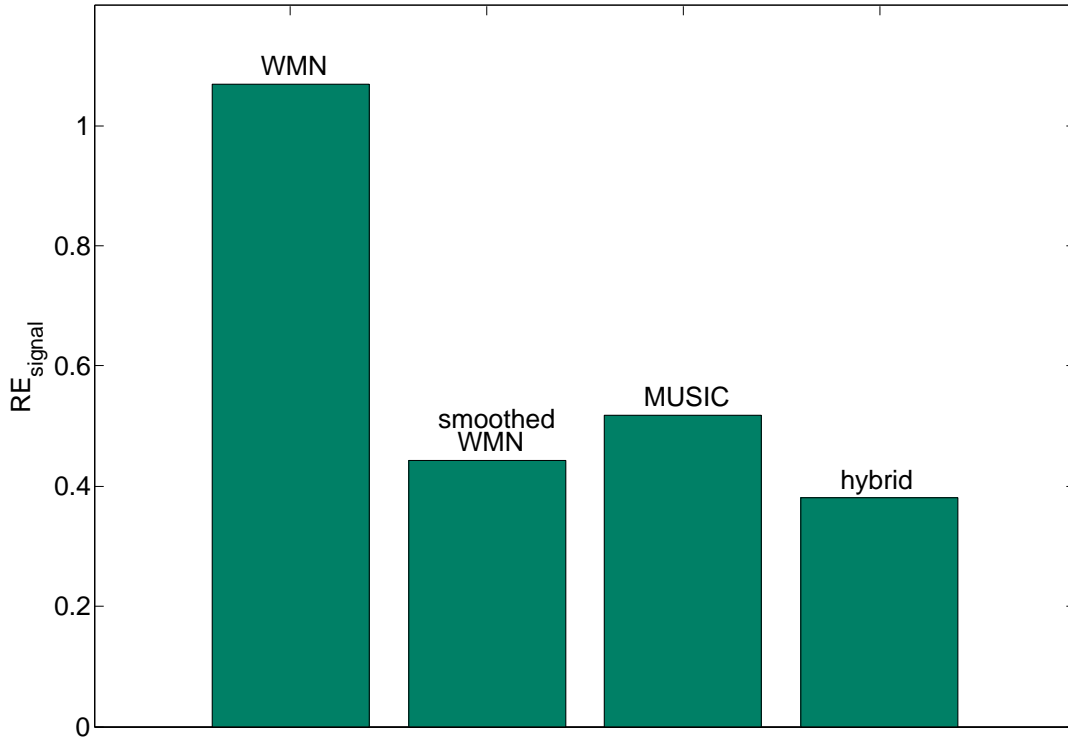


Figure 6.11: RE_{signal} of the initial states averaged over the 12 pacer locations ($SNR = 8.66 \times 10^3$, $\bar{d} = 5.25$ mm, $\varepsilon = 0.001$).

	WMN	smoothed WMN	MUSIC	WMN-MUSIC hybrid
BLW	4.76	4.99	14.99	9.79
BRW	20.27	7.15	6.91	5.13
BP	7.99	3.02	4.10	2.09
BA	9.55	4.32	6.61	1.09
BS	13.02	9.88	18.46	16.11
MLW	19.61	11.44	13.35	12.25
MRW	15.23	12.33	12.82	11.57
MP	12.62	7.69	16.83	15.46
MA	4.98	5.51	11.29	8.45
MS	18.20	20.89	9.83	12.04
AA	68.34	4.12	9.98	4.10
AP	22.82	11.55	8.71	9.43
averaged	18.12	8.57	11.16	8.96

Table 6.3: Localization Errors (LE) in mm for the 12 pacer locations of figure 6.1. The last line shows the LE averaged over the 12 pacer locations. The smallest averaged LE is in bold print.

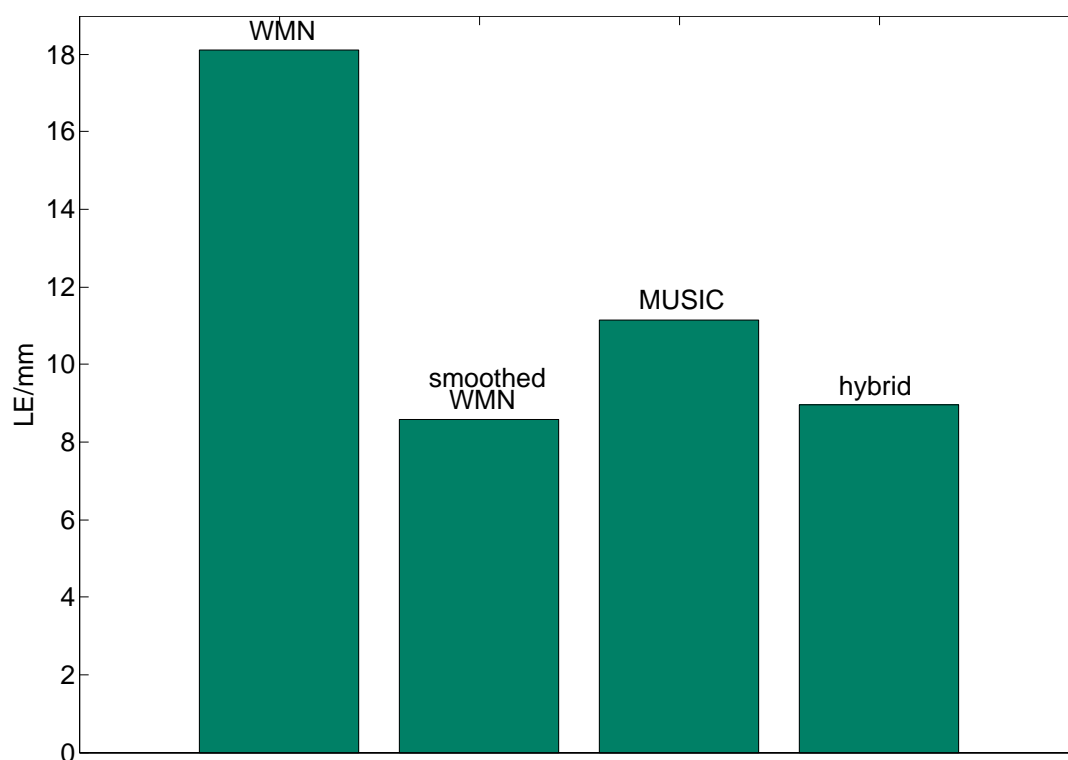


Figure 6.12: LE of the initial states averaged over the 12 pacer locations ($SNR = 8.66 \times 10^3$, $\bar{d} = 5.25$ mm, $\varepsilon = 0.001$).

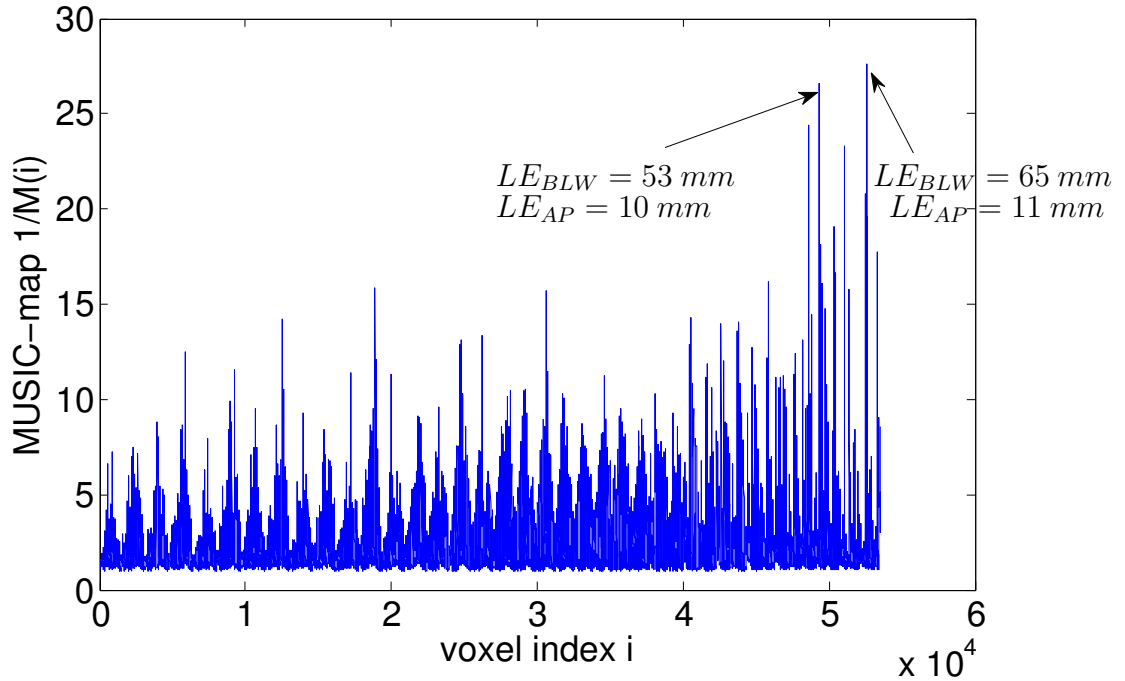


Figure 6.13: MUSIC-map $1/M(i)$ for the 2 simultaneously activated pacers BLW-AP as a function of the voxel index i ($\Delta t = 12$ ms).

6.1.5 Comparison of the reconstructed activation times for 2 pacers

The incidence of multiple accessory pathways in Wolff-Parkinson-White syndrome has been reported to be about 3 – 20% in surgical series and 5 – 18% in radiofrequency ablation series [38]. In this section the initial state generators are compared for the following pairs of pacer locations (figure 6.1): BA-MP, BRW-MLW, BP-MS, BLW-AA, BLW-AP, BS-AP, MA-AP. The pair BLW-AP will be used for the purpose of demonstration.

First the case of simultaneously activated pacers will be investigated: Figure 6.13 shows the MUSIC-map $1/M(i)$ for the $r = 2$ pacers BLW-AP activated at the same time. Although the 2 maxima in the MUSIC-map should represent the location of the 2 pacers BLW-AP, the shown Localization Errors LE (black arrows) suggest that only the pacer location AP can be localized. The pacer location BLW (at voxel index $i = 8854$) is not visible in the map. One requirement for the MUSIC algorithm is that the activated sources (here: pacers) have a linearly independent time series [39]. Because the 2 pacers BLW-AP are activated at the same time, the corresponding 2 magnetic field topologies have linearly dependent time series so the pacers can hardly be identified in the MUSIC-map so the MUSIC algorithm is not applicable to localize simultaneously activated pacers.

As an example for WMN the figure 6.14 shows the (non-smoothed) WMN acti-

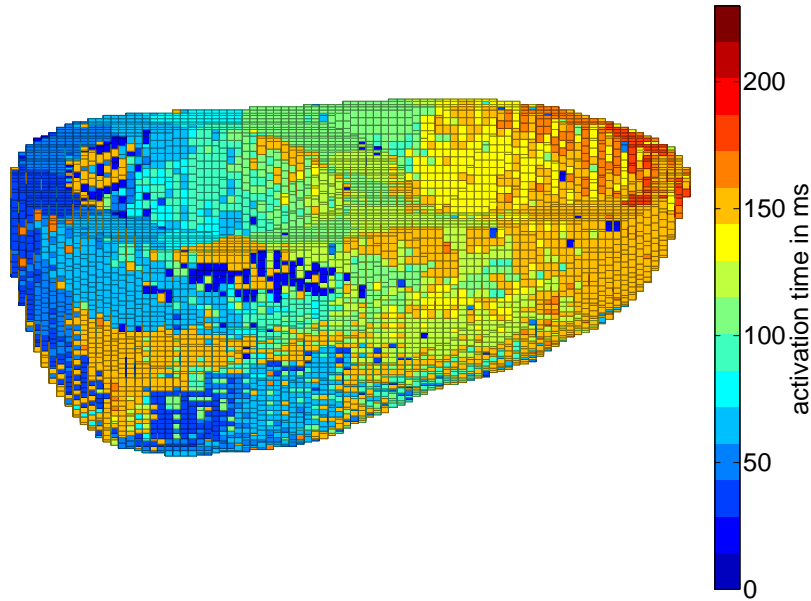


Figure 6.14: WMN activation times of the 2 pacer locations BLW-AP ($SNR = 8.66 \times 10^3$, truncation at $P = 50$, $RE = 0.399$, $RE_{signal} = 1.707$).

	BAMP	BRWMLW	BPMS	BLWAA	BLWAP	BSAP	MAAP	av.
RE	0.286	0.240	0.287	0.199	0.282	0.357	0.309	0.280
$\frac{LE_1}{mm}$	33.44	17.75	14.69	11.02	9.84	35.94	17.56	20.03
$\frac{LE_2}{mm}$	18.12	33.17	20.40	12.55	41.79	58.86	39.43	36.62

Table 6.4: Smoothed WMN errors for 2 simultaneously activated pacers. The last column (av.) shows the average over all pairs of pacers.

vation times of the 2 pacer locations BLW-AP. In figure 6.15 the WMN activation times are smoothed via the process function $f(\mathbf{x})$. Similar to the case of single pacer activation RE and RE_{signal} are reduced by the recursive smoothing algorithm of equation (6.10). Figure 6.16 shows the simulated activation times.

In the following the case of non-simultaneously activated pacers will be investigated: The time delay is set to $t_2 - t_1 = 20 ms$, so the first pacer location is activated at $t_1 = 0 ms$ and the second at $t_2 = 20 ms$. Figure 6.17 shows the MUSIC-map $1/M(i)$ for a time delay of $20 ms$ and the pair of pacer locations BLW-AP. Because the MUSIC algorithm only selects the initial time interval $\overline{\Delta t} = 12 ms$ of the data and the second pacer AP starts at $t_2 = 20 ms$, the contribution of the second pacer AP is excluded from the data. The corresponding MUSIC-map should be the same as in the single pacer stimulation (data noise errors neglected). Indeed the Localization Error $LE_{BLW} = 14.99 mm$ for the pacer location BLW is the same as in the single pacer case (table 6.3). In figure 6.18 the initial time interval is increased

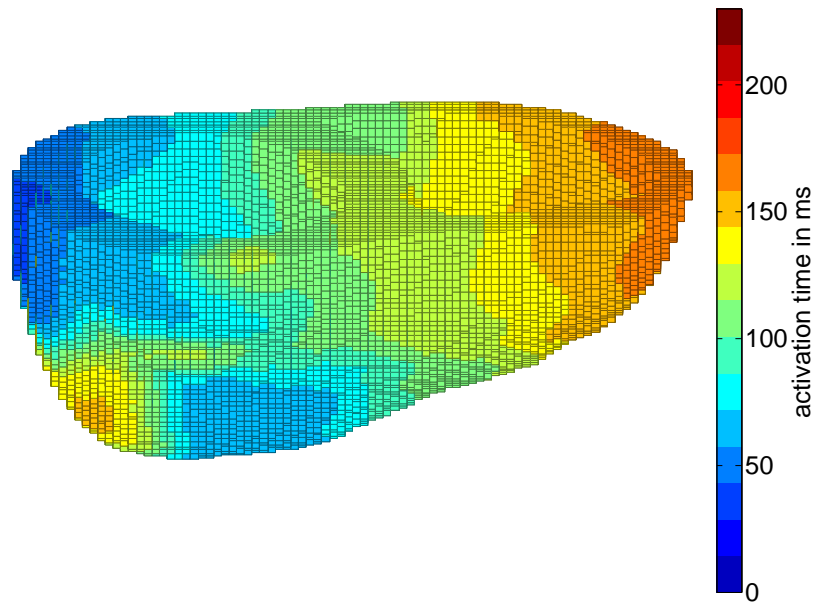


Figure 6.15: Smoothed WMN activation times of the 2 pacemaker locations BLW-AP ($\varepsilon = 0.001$, $\bar{d} = 5.25 \text{ mm}$, $RE = 0.282$, $RE_{signal} = 0.572$).

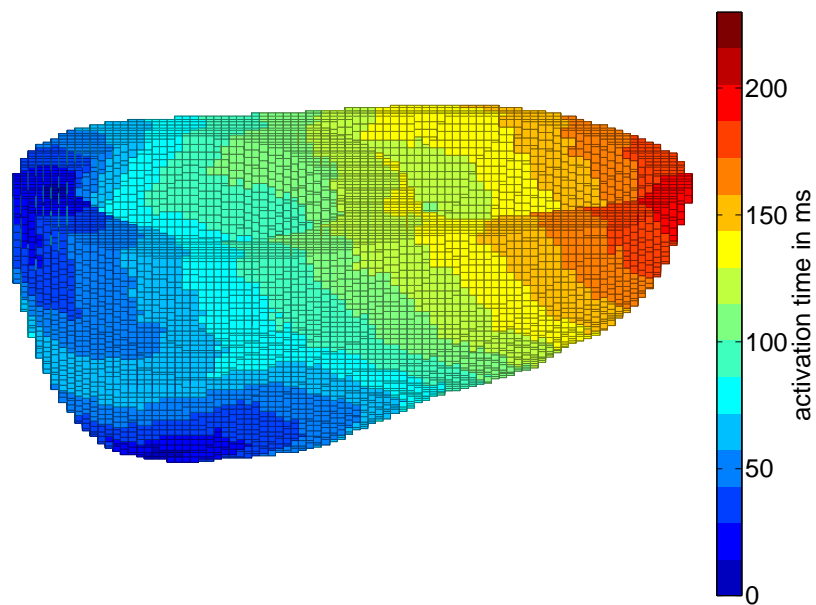


Figure 6.16: True (=simulated) activation times of the 2 pacemaker locations BLW-AP.

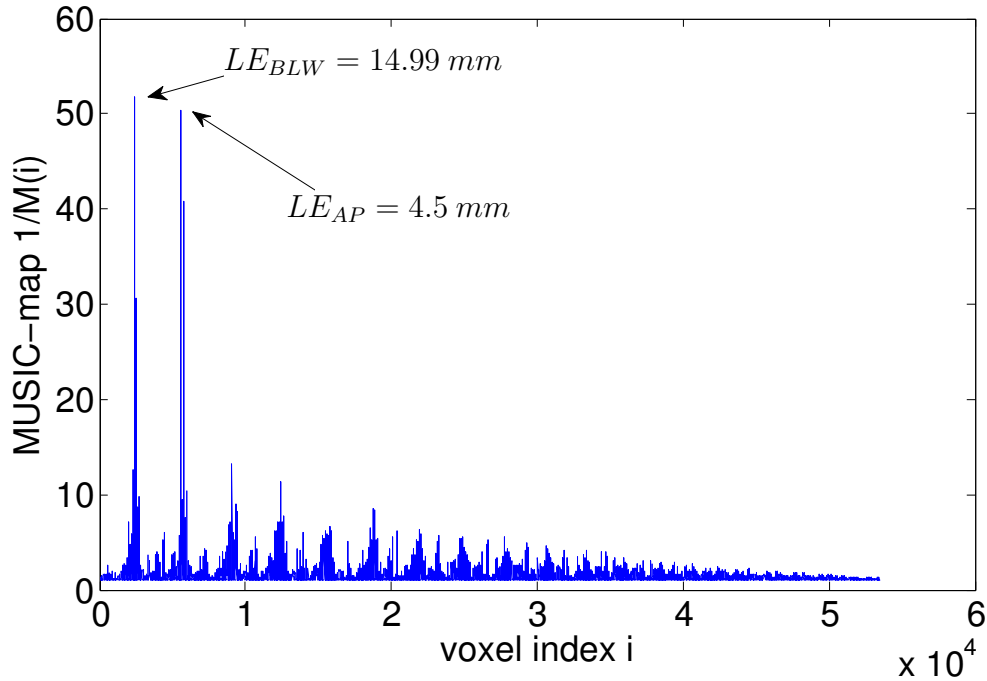


Figure 6.17: MUSIC-map $1/M(i)$ for the 2 pacers BLW-AP with a time delay of 20 ms as a function of the voxel index i ($\overline{\Delta t} = 12\text{ ms}$).

to $\overline{\Delta t} = 24\text{ ms}$ that the second pacer AP is included in the data. This results in a second peak in the MUSIC-map that cannot be clearly identified with the AP location because of the big Localization Error ($LE_{AP} = 44\text{ mm}$). In figure 6.19 the initial time interval is further increased to $\overline{\Delta t} = 27\text{ ms}$ but a clear identification of the MUSIC-peaks with the pacers BLW or AP is also hardly possible: The signal of the first activated BLW pacer dominates over the signal of the AP pacer and the spatial extent of the depolarization wavefront of the BLW pacer is too big for the single dipole approximation. So although the time series of the pacers are linearly independent for the case of a time delay of 20 ms , only the first pacer BLW can be localized with the MUSIC algorithm and neglecting noise errors the Localization Errors are the same as in the single pacer case (table 6.3).

Figure 6.20 shows the non-smoothed WMN activation times of the pacer locations BLW-AP with time delay of 20 ms between the pacer activations, figure 6.21 shows the smoothed WMN activation times of the pacer locations BLW-AP with time delay of 20 ms between the pacer activations and figure 6.22 the corresponding simulated activation times. Table 6.5 shows the corresponding Relative Errors and Localization Errors with time delay of 20 ms for the smoothed WMN method. In comparison with the errors of simultaneously activated pacers (table 6.4) the average Localization Error of the first activated pacer is significantly reduced from 20.03 mm (simultaneously) to 10.25 mm (time delay of 20 ms): in the case of the 20 ms time delay there is a smaller overlap between the depolarization wavefronts of the first and the second pacer, so the localization of the first pacer is more accurate.

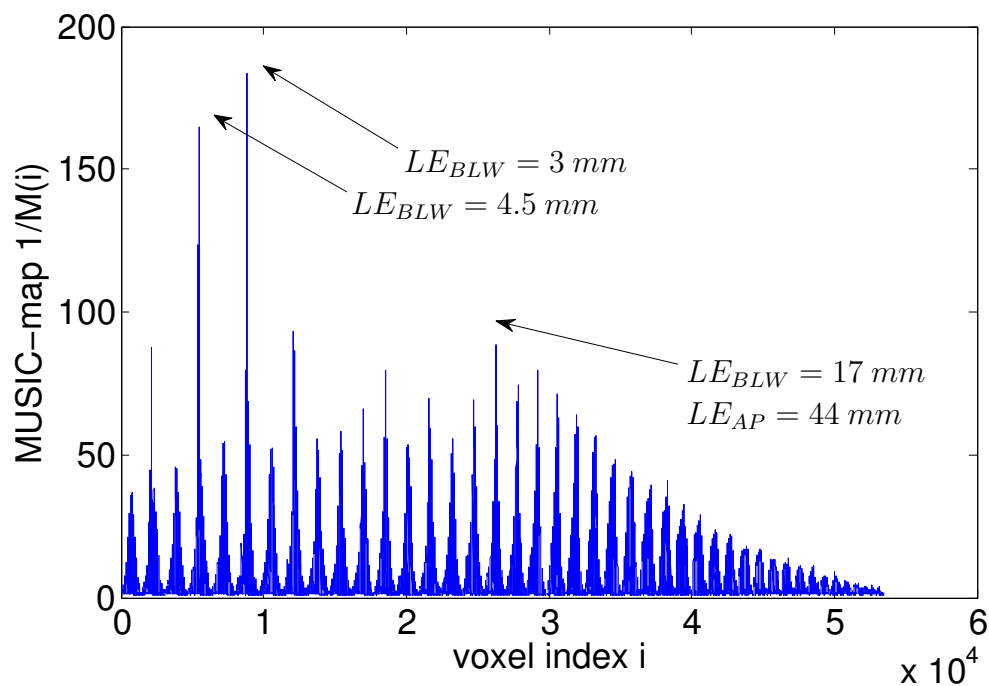


Figure 6.18: MUSIC-map $1/M(i)$ for the 2 pacers BLW-AP with a time delay of 20 ms as a function of the voxel index i ($\Delta t = 24 \text{ ms}$).

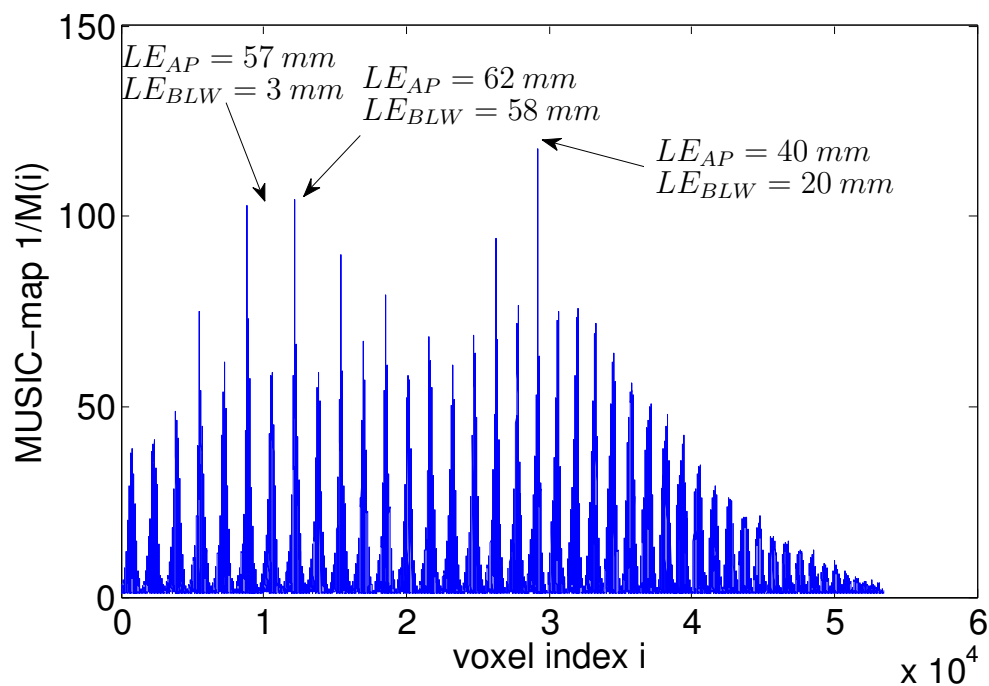


Figure 6.19: MUSIC-map $1/M(i)$ for the 2 pacers BLW-AP with a time delay of 20 ms as a function of the voxel index i ($\Delta t = 27 \text{ ms}$).

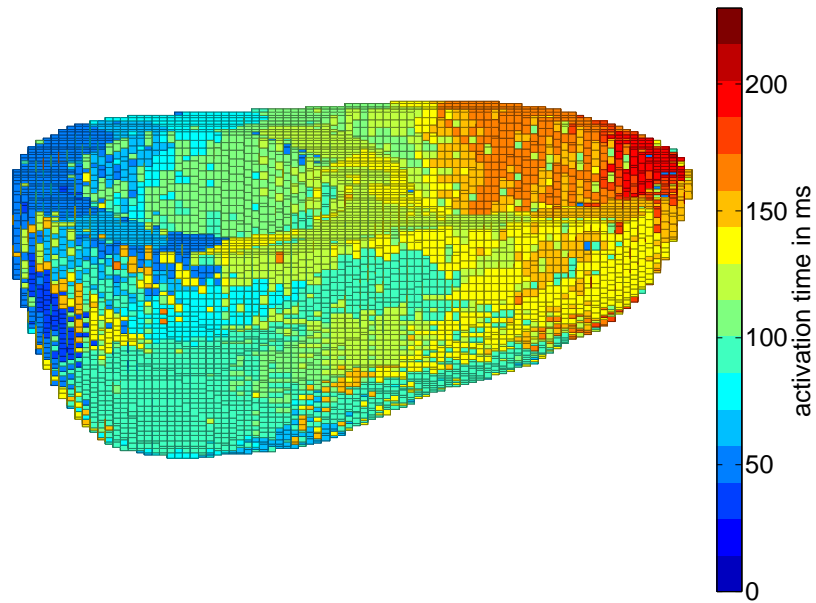


Figure 6.20: WMN activation times of the 2 pacer locations BLW-AP with a time delay of 20 ms ($SNR = 8.66 \times 10^3$, $P = 50$, $RE = 0.232$, $RE_{signal} = 1.270$).

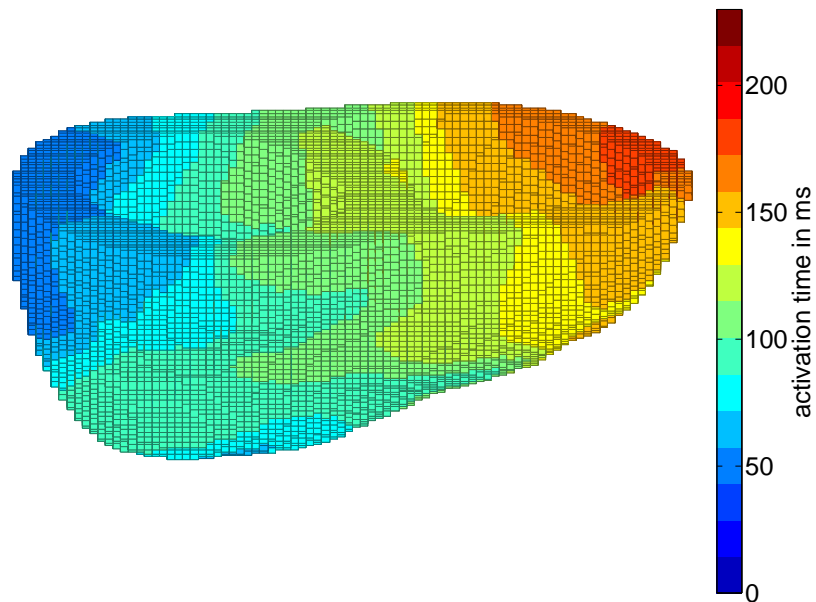


Figure 6.21: Smoothed WMN activation times of the 2 pacer locations BLW-AP with a time delay of 20 ms ($\varepsilon = 0.001$, $\bar{d} = 5.25$ mm, $RE = 0.173$, $RE_{signal} = 0.455$).

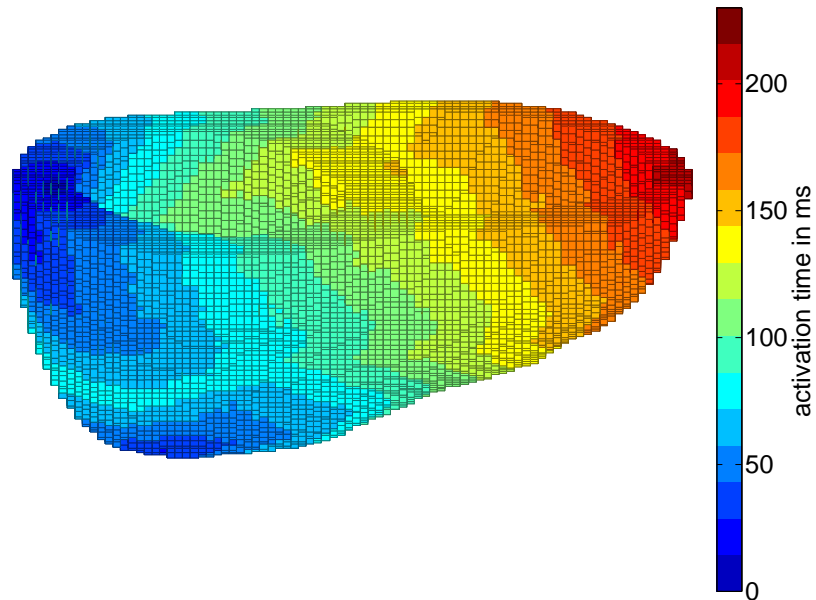


Figure 6.22: True (=simulated) activation times of the 2 pacer locations BLW-AP with a time delay of 20 *ms*.

	BAMP	BRWMLW	BPMS	BLWAA	BLWAP	BSAP	MAAP	av.
RE	0.239	0.258	0.276	0.199	0.173	0.198	0.248	0.227
$\frac{LE_1}{mm}$	6.16	17.84	14.74	11.46	8.71	7.70	5.15	10.25
$\frac{LE_2}{mm}$	41.70	59.04	15.66	18.61	51.74	58.42	57.09	43.18

Table 6.5: Smoothed WMN errors for 2 pacers with time delay of 20 *ms*. The last column (av.) shows the average over all pairs of pacers.

6.2 Kalman Filters

In this work the Extended Kalman Filter (EKF) and the Unscented Kalman Filter (UKF) [40] are used for the estimation of the activation times in the ventricles. Both Kalman Filters are specialized for estimation or localization problems in nonlinear systems. Because the measurement function $\mathbf{h}(\mathbf{x})$ (equation (4.27)) and the smoothing process function $\mathbf{f}(\mathbf{x})$ (equation (6.9)) are nonlinear (and even nonsmooth) functions of the activation times \mathbf{x} , an application of the EKF and UKF for the estimation of activation times is reasonable. In the first section the underlying nonlinear state-space model will be discussed.

6.2.1 Nonlinear state-space model

As discussed in chapter 1 the solution of the system of linear equations (1.1) is non-unique, because of the huge number n of cells in the ventricles compared to the number of sensors m . In the system of nonlinear equations (4.28) the number of equations also is smaller than the number of variables, $m \cdot N < n$ (in the simulations of this chapter $m = 72$ is the number of sensors, $N < 78$ the number of data time samples and $n = 53476$ the number of cells in the ventricles). In general the solution of the nonlinear system of equations (4.28) is assumed to be non-unique too. To tackle the non-uniqueness of equation (4.28) a state-space model is formulated introducing the smoothing process function $\mathbf{f}(\mathbf{x})$ of equation (6.9) [8]

$$\begin{aligned}\mathbf{x}_k &= \mathbf{f}(\mathbf{x}_{k-1}) + \mathbf{w}_{k-1} \\ \phi_k &= \mathbf{h}(\mathbf{x}_k) + \mathbf{v}_k\end{aligned}\tag{6.14}$$

where \mathbf{x}_k is the activation time state vector of iteration step k ($k = 1, 2, 3, \dots$), \mathbf{f} is a process function that predicts the k -th state from the $(k-1)$ -th state, ϕ_k is the MCG data vector of the full k -th heart beat and \mathbf{v}_k and \mathbf{w}_{k-1} are the measurement noise and process noise, respectively. Both are assumed as Gaussian white noise with the following normal distributions

$$p(\mathbf{w}) \sim N(0, \mathbf{Q}) \quad p(\mathbf{v}) \sim N(0, \mathbf{R})\tag{6.15}$$

where \mathbf{R} and \mathbf{Q} are the noise covariance matrices of the measurement and process, respectively. Equation (6.14) doesn't state the recursive algorithm of the Kalman Filters, it just represents the underlying dynamical model. The explicit recursive algorithms of the EKF and UKF are shown in the next two subsections.

6.2.2 Extended Kalman Filter (EKF)

The main idea of the Extended Kalman Filter [41] is the linearization of the nonlinear state-space model (6.14) by calculating the Jacobian matrices \mathbf{H}, \mathbf{F} of the functions \mathbf{h}, \mathbf{f} and approximating the first partial derivatives with difference quotients [8]

$$\begin{aligned}
H_{ij} &= \frac{h^i(x^1, \dots, x^j + \delta t, \dots, x^n) - h^i(x^1, \dots, x^j - \delta t, \dots, x^n)}{2\delta t} \\
F_{ij} &= \frac{f^i(x^1, \dots, x^j + \delta t, \dots, x^n) - f^i(x^1, \dots, x^j - \delta t, \dots, x^n)}{2\delta t}
\end{aligned} \tag{6.16}$$

with the temporal resolution δt and omitting the iteration step index k . The Extended Kalman Filter now minimizes the error covariance matrix \mathbf{P}_k [41] defined by the expectation values

$$\mathbf{P}_k = \langle (\mathbf{x}_k - \mathbf{x}_{true})(\mathbf{x}_k - \mathbf{x}_{true})^T \rangle \tag{6.17}$$

where \mathbf{x}_{true} is the true activation sequence and \mathbf{x}_k the estimated activation of step k . The minimization of the error covariance matrix \mathbf{P}_k is done with a recursive algorithm which works as follows.

In the “predict” procedure of the algorithm a priori estimates of the state vector and the error covariance matrix are projected from the last step

$$\mathbf{x}_k^- = \mathbf{f}(\mathbf{x}_{k-1}) \tag{6.18}$$

$$\mathbf{P}_k^- = \mathbf{F}_k \mathbf{P}_{k-1} \mathbf{F}_k^T + \mathbf{Q}. \tag{6.19}$$

In the “correct” procedure, the Kalman gain² \mathbf{K}_k is calculated and the state vector and error covariance matrix are updated with the measured data ϕ_k

$$\mathbf{K}_k = \mathbf{P}_k^- \mathbf{H}_k^T (\mathbf{H}_k \mathbf{P}_k^- \mathbf{H}_k^T + \mathbf{R})^{-1} \tag{6.20}$$

$$\mathbf{x}_k = \mathbf{x}_k^- + \mathbf{K}_k (\phi_k - \mathbf{h}(\mathbf{x}_k^-)) \tag{6.21}$$

$$\mathbf{P}_k = (\mathbf{1} - \mathbf{K}_k \mathbf{H}_k) \mathbf{P}_k^- \tag{6.22}$$

\mathbf{x}_k and \mathbf{P}_k are then used for the next iteration step.

6.2.3 Unscented Kalman Filter (UKF)

Although the Unscented Kalman Filter is an algorithm that estimates the mean and covariance of the Gaussian distributed activation time state-vector \mathbf{x} to the 3rd order Taylor series [9], it doesn’t make use of partial derivatives of 2nd or 3rd order. Instead of calculating partial derivatives it uses a statistical sampling method to generate estimates for the state-vector of the next iteration step. The Unscented Kalman Filter [40] [43] generates a deterministic set of sampling points, stored in the $n \times (2n + 1)$ sigma point matrix \mathcal{X}_{k-1} . The columns of \mathcal{X}_{k-1} are calculated by

²A derivation of the Kalman gain \mathbf{K}_k from the minimization of the error covariance \mathbf{P}_k can be found in [42].

$$\begin{aligned}
(\boldsymbol{\mathcal{X}}_{k-1})_1 &= \mathbf{x}_{k-1} \\
(\boldsymbol{\mathcal{X}}_{k-1})_i &= \mathbf{x}_{k-1} + (\sqrt{(n+\lambda)\mathbf{P}_{k-1}})_{i-1}, \quad i = 2, \dots, n+1 \\
(\boldsymbol{\mathcal{X}}_{k-1})_i &= \mathbf{x}_{k-1} - (\sqrt{(n+\lambda)\mathbf{P}_{k-1}})_{i-1-n}, \quad i = n+2, \dots, 2n+1
\end{aligned} \tag{6.23}$$

where $(\sqrt{(n+\lambda)\mathbf{P}_{k-1}})_i$ is the i th column of the matrix square root and λ is defined by

$$\lambda = \alpha^2(n + \kappa) - n \tag{6.24}$$

where α and κ are scaling parameters that determine the spread of the sigma points. The square root \mathbf{A} of a matrix \mathbf{B} satisfies $\mathbf{B} = \mathbf{A}\mathbf{A}^T$ and for the symmetric and positive definite matrix $\mathbf{B} = (n+\lambda)\mathbf{P}_{k-1}$ it can be calculated using a Cholesky decomposition [44]. In the “predict” procedure the sigma points are propagated by the process function

$$(\boldsymbol{\mathcal{X}}_k)_i = \mathbf{f}((\boldsymbol{\mathcal{X}}_{k-1})_i), \quad i = 1, \dots, 2n+1. \tag{6.25}$$

Then the a priori state estimate is calculated by

$$\mathbf{x}_k^- = \sum_{i=1}^{2n+1} W_i^{(m)} (\boldsymbol{\mathcal{X}}_k)_i \tag{6.26}$$

where $W_i^{(m)}$ are weights defined by

$$W_1^{(m)} = \frac{\lambda}{(n+\lambda)} \tag{6.27}$$

$$W_i^{(m)} = \frac{1}{2(n+\lambda)}, \quad i = 2, \dots, 2n+1 \tag{6.28}$$

and the a priori error covariance matrix is calculated by

$$\mathbf{P}_k^- = \sum_{i=1}^{2n+1} W_i^{(c)} [(\boldsymbol{\mathcal{X}}_k)_i - \mathbf{x}_k^-][(\boldsymbol{\mathcal{X}}_k)_i - \mathbf{x}_k^-]^T + \mathbf{Q} \tag{6.29}$$

with the process error covariance matrix \mathbf{Q} and the following weights

$$W_1^{(c)} = \frac{\lambda}{(n+\lambda)} + (1 - \alpha^2 + \beta) \tag{6.30}$$

$$W_i^{(c)} = \frac{1}{2(n+\lambda)}, \quad i = 2, \dots, 2n+1. \tag{6.31}$$

β is another scaling parameter to adjust the speed of convergence. In the “correct” procedure first the sigma points are transformed by the measurement function

$$(\mathbf{z}_k)_i = \mathbf{h}((\mathbf{x}_k)_i), \quad i = 1, \dots, 2n + 1 \quad (6.32)$$

$$\mathbf{z}_k^- = \sum_{i=1}^{2n+1} W_i^{(m)} (\mathbf{z}_k)_i. \quad (6.33)$$

With the field vector \mathbf{z}_k^- we can now compute the a posteriori state estimate

$$\mathbf{x}_k = \mathbf{x}_k^- + \mathbf{K}_k (\phi_k - \mathbf{z}_k^-) \quad (6.34)$$

where the Kalman gain \mathbf{K}_k of the UKF is defined by

$$\mathbf{K}_k = \mathbf{P}_{\mathbf{x}_k \mathbf{z}_k} \mathbf{P}_{\mathbf{z}_k \mathbf{z}_k}^{-1} \quad (6.35)$$

with

$$\mathbf{P}_{\mathbf{z}_k \mathbf{z}_k} = \sum_{i=1}^{2n+1} W_i^{(c)} [(\mathbf{z}_k)_i - \mathbf{z}_k^-][(\mathbf{z}_k)_i - \mathbf{z}_k^-]^T + \mathbf{R} \quad (6.36)$$

$$\mathbf{P}_{\mathbf{x}_k \mathbf{z}_k} = \sum_{i=1}^{2n+1} W_i^{(c)} [(\mathbf{x}_k)_i - \mathbf{x}_k^-][(\mathbf{z}_k)_i - \mathbf{z}_k^-]^T \quad (6.37)$$

where \mathbf{R} is the measurement noise covariance matrix. In the last step the error covariance matrix has to be updated

$$\mathbf{P}_k = \mathbf{P}_k^- - \mathbf{K}_k \mathbf{P}_{\mathbf{z}_k \mathbf{z}_k} \mathbf{K}_k^T. \quad (6.38)$$

6.2.4 Results: Comparison of EKF and UKF for single pacers

In this section the results of the Kalman Filter calculations for the 12 single pacers of figure 6.1 and for the 3 initial state generators of section 6.1 (smoothed WMN, MUSIC and hybrid) will be presented. The errors shown in the figures 6.23 to 6.28 are errors averaged over the 12 pacer locations. The EKF results are presented in red, the UKF results in blue. The errors are assumed to be converged after $k = 25$ Kalman Filter iteration steps. For the Kalman Filter parameters $(\delta t, \alpha, \dots)$ there have been made parameter tests shown in the appendix C to get an optimized convergence in the iteration step interval $k = 1, \dots, 25$. The results of the convergence tests in appendix C are $\varepsilon = 0.001$, $\delta t = 4 \text{ ms}$, $\alpha = 2$, $\bar{d} = 5.25 \text{ mm}$, $Q = 0.1$ (EKF) and $Q = 1$ (UKF). Because the UKF parameters β and κ only have small influence on the convergence of RE and LE , they have been set to be zero ($\beta = 0 = \kappa$).

Figure 6.23 shows the Kalman Filter convergence of the Relative Error RE and figure 6.24 the converged values of RE at $k = 25$ iteration steps. One can see from figure 6.24 that for all types of initial state generators both Kalman Filters reduce the Relative Error and the UKF generates a smaller Relative Error than the EKF. The combination of initial state generator and Kalman Filter that produces

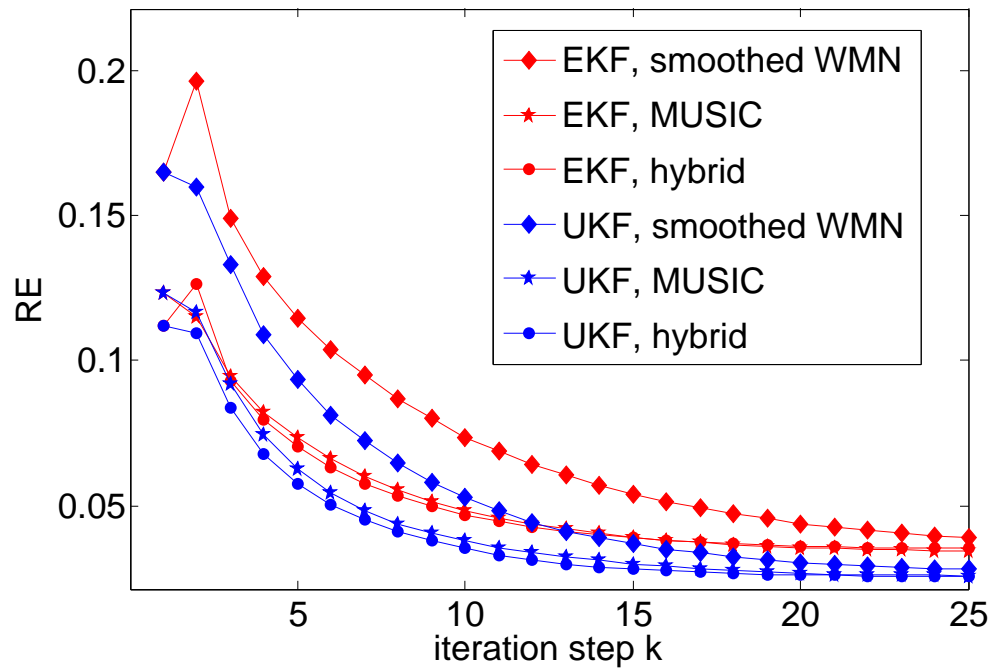


Figure 6.23: Convergence of RE averaged over the 12 pacer locations as a function of the Kalman Filter iteration step k ($SNR = 8.66 \times 10^3$, $\bar{d} = 5.25$ mm, $\varepsilon = 0.001$).

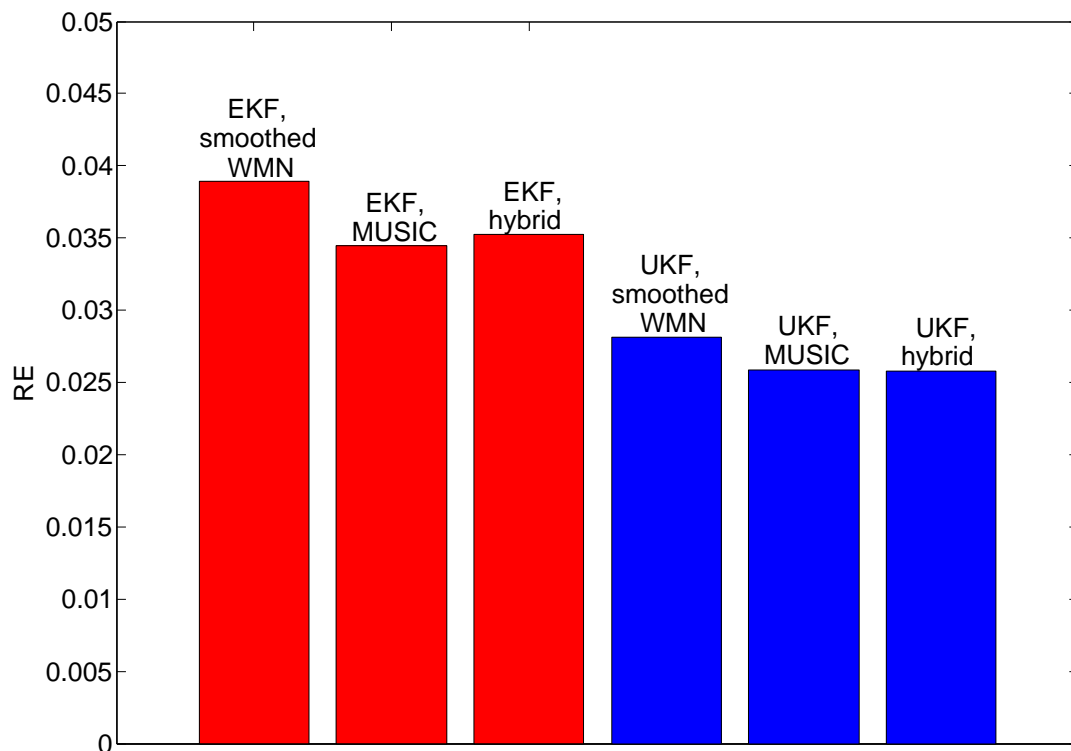


Figure 6.24: Converged RE ($k = 25$) averaged over the 12 pacer locations ($SNR = 8.66 \times 10^3$, $\bar{d} = 5.25$ mm, $\varepsilon = 0.001$).

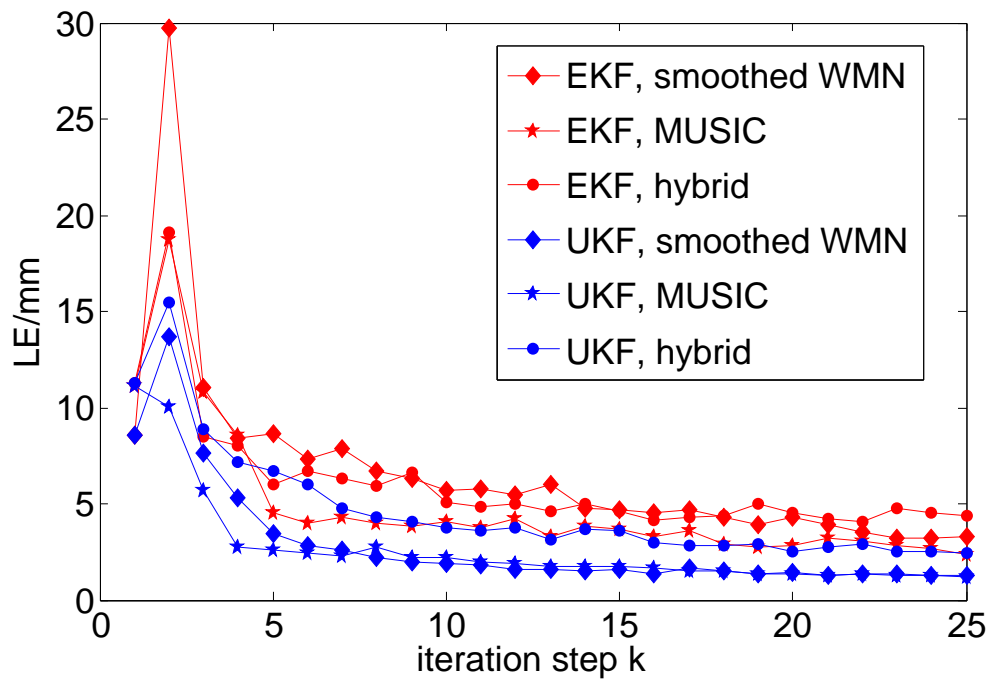


Figure 6.25: Convergence of LE averaged over the 12 pacer locations as a function of the Kalman Filter iteration step k ($SNR = 8.66 \times 10^3$, $\bar{d} = 5.25$ mm, $\varepsilon = 0.001$).

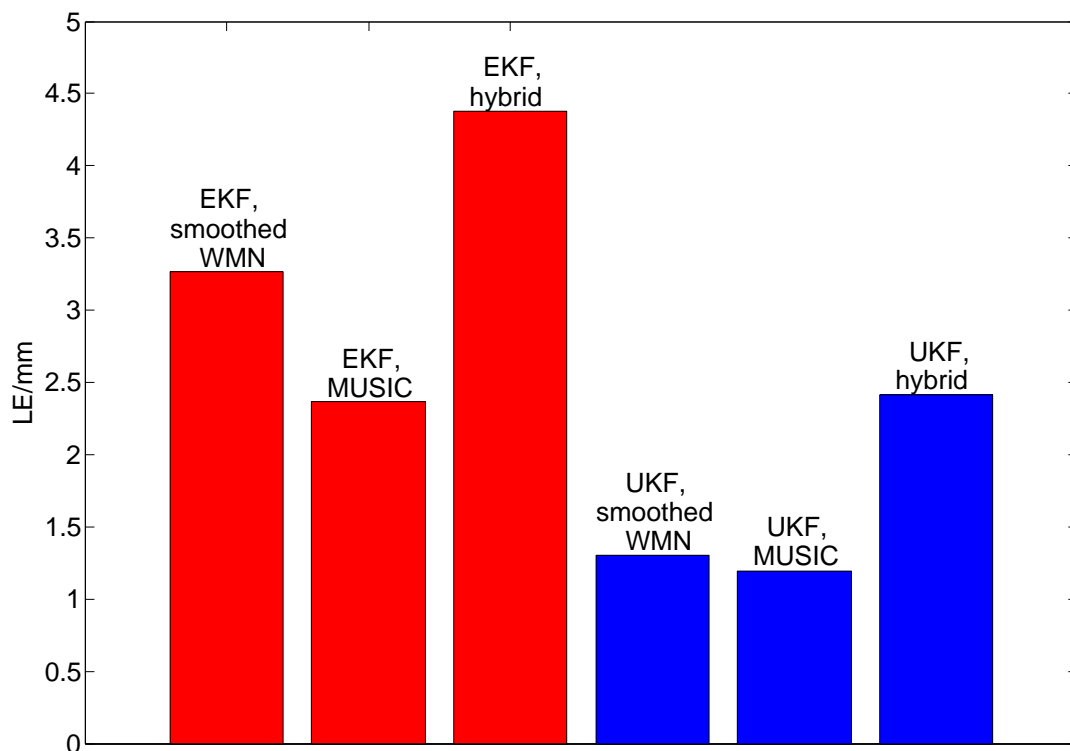


Figure 6.26: Converged LE ($k = 25$) averaged over the 12 pacer locations ($SNR = 8.66 \times 10^3$, $\bar{d} = 5.25$ mm, $\varepsilon = 0.001$).

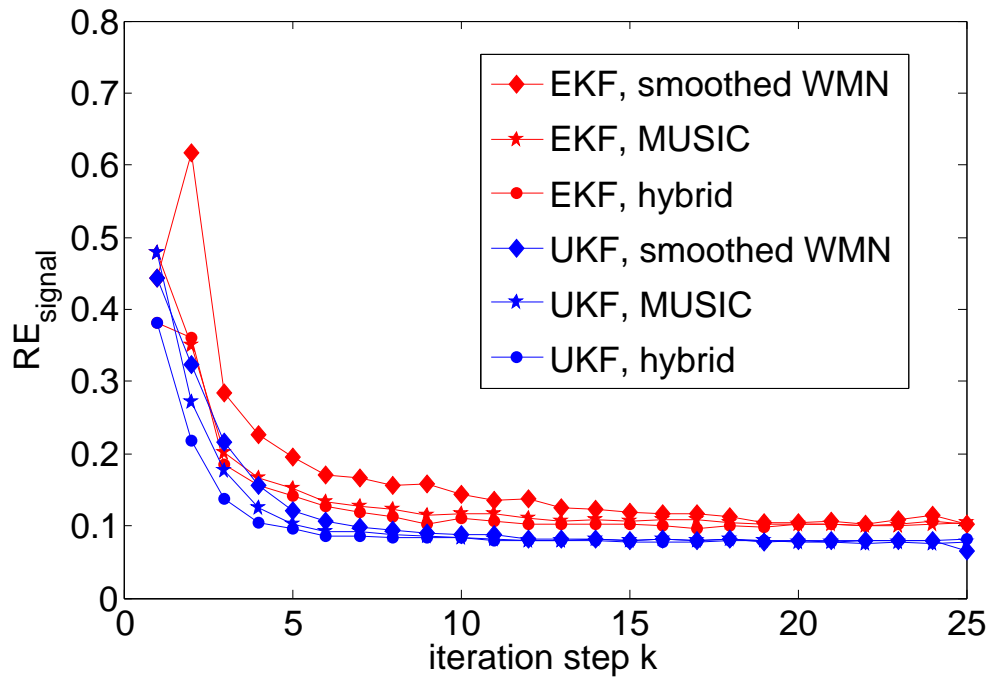


Figure 6.27: Convergence of RE_{signal} averaged over the 12 pacer locations as a function of the iteration step k ($SNR = 8.66 \times 10^3$, $\bar{d} = 5.25$ mm, $\varepsilon = 0.001$).

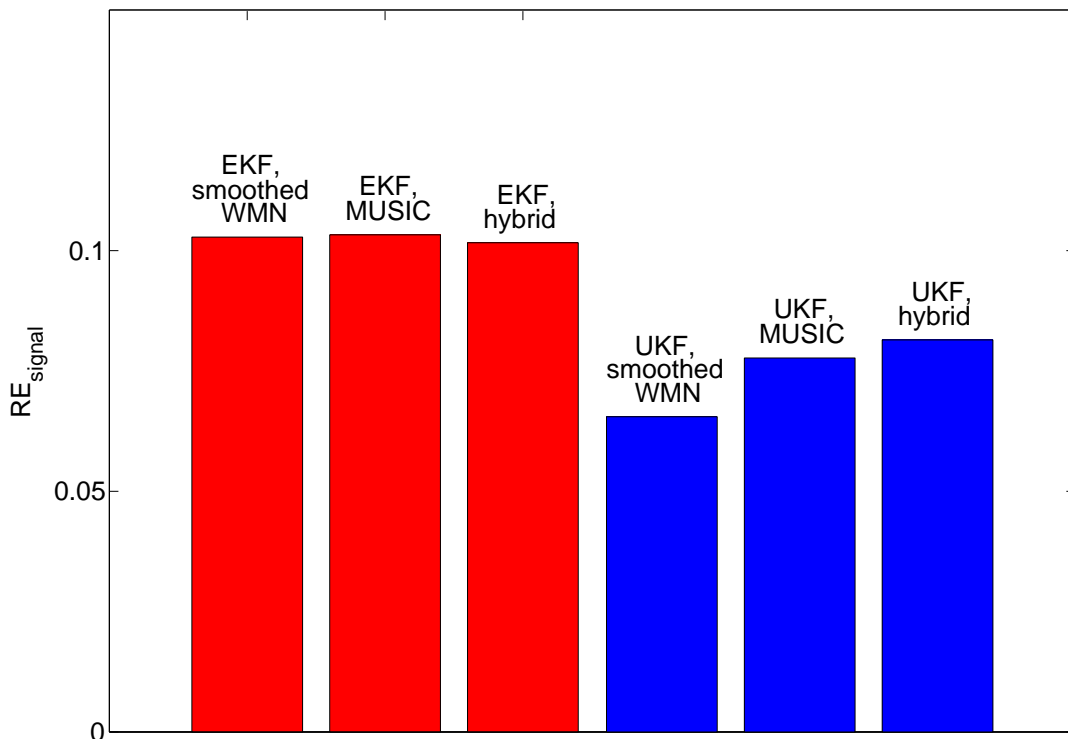


Figure 6.28: Converged RE_{signal} ($k = 25$) averaged over the 12 pacer locations ($SNR = 8.66 \times 10^3$, $\bar{d} = 5.25$ mm, $\varepsilon = 0.001$).

the smallest Relative Error is (UKF,MUSIC).

Figure 6.25 shows the convergence of the Localization Error LE for all types of initial state generators and both Kalman Filters and figure 6.26 the converged values of LE at iteration step $k = 25$. As one can see from figure 6.25 both Kalman Filters reduce the Localization Errors in comparison with the Localization Errors of the initial states. As one can see from figure 6.24 the combination of the Kalman Filter UKF and the initial state MUSIC also produces the smallest converged Localization Error of $LE = 1.19 \text{ mm}$ for accessory pathway localization. The averaged Localization Error of $LE = 3.26 \text{ mm}$ for the combination (EKF,smoothed WMN) is comparable with the EKF-WMN result $LE = 3 \text{ mm}$ of [8].

Figure 6.27 shows the convergence of the Relative Error of the measured signal RE_{signal} calculated with equation (6.8) and figure 6.28 the corresponding converged value of RE_{signal} at $k = 25$ iteration steps. Again for all types of initial states the UKF produces a smaller RE_{signal} than the EKF. The nonlinearity of the measurement function $\mathbf{h}(\mathbf{x})$ can be seen in a change of the order of the converged RE_{signal} with respect to the initial states in figure 6.28: while in figure 6.24 the combination (UKF,MUSIC) produces the smallest RE , in figure 6.28 the combination (UKF,smoothed WMN) produces the smallest RE_{signal} .

In the convergence figures 6.23, 6.25 and 6.27 one can see that the Kalman Filter algorithms, especially the EKF, often seem to have a problem with the first iteration step that shows an increasing error RE/LE . From figure 6.23 one can see that this could be due to properties of the initial state: while the RE for the initial state MUSIC is reduced in the first iteration step for both EKF and UKF, the RE for the initial states hybrid and smoothed WMN are increased in the first iteration step. In the appendix C there will be shown that the choice of the Kalman Filter parameters (e.g. the spread of the sigma points α , figure C.4) can also determine whether RE increases or decreases in the first iteration step.

Figures 6.29 to 6.34 exemplarily show the converged activation times of the pacer location BLW for all investigated inverse algorithms. The improvement of the activation time map due to the application of the Kalman Filters can be seen for instance in the reduced distance between the wavefronts in the septal regions of the smoothed WMN solutions in figure 6.29 and 6.30 in comparison with the initial state of figure 6.5.

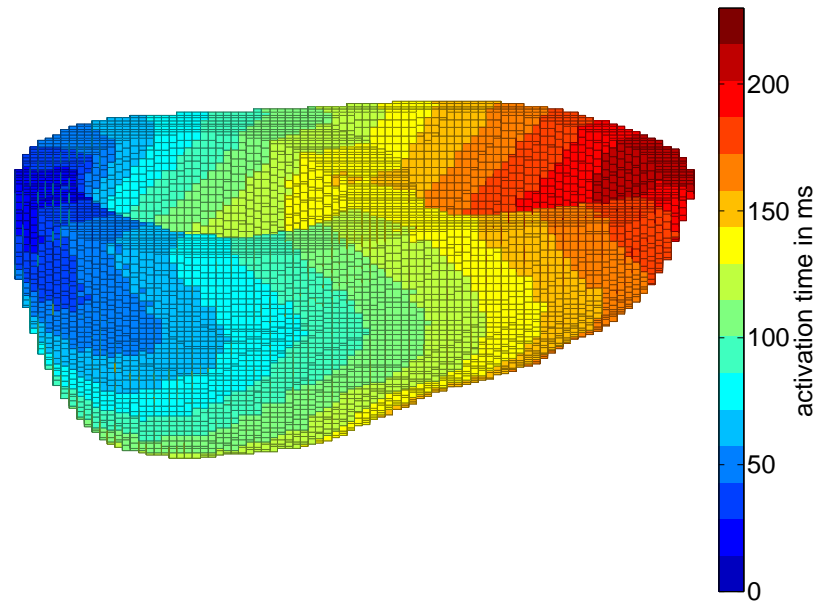


Figure 6.29: (EKF, smoothed WMN) activation times of the pacer location BLW ($\varepsilon = 0.001$, $\bar{d} = 5.25$ mm, $RE = 0.032$, $RE_{signal} = 0.091$, $LE = 2.6$ mm).

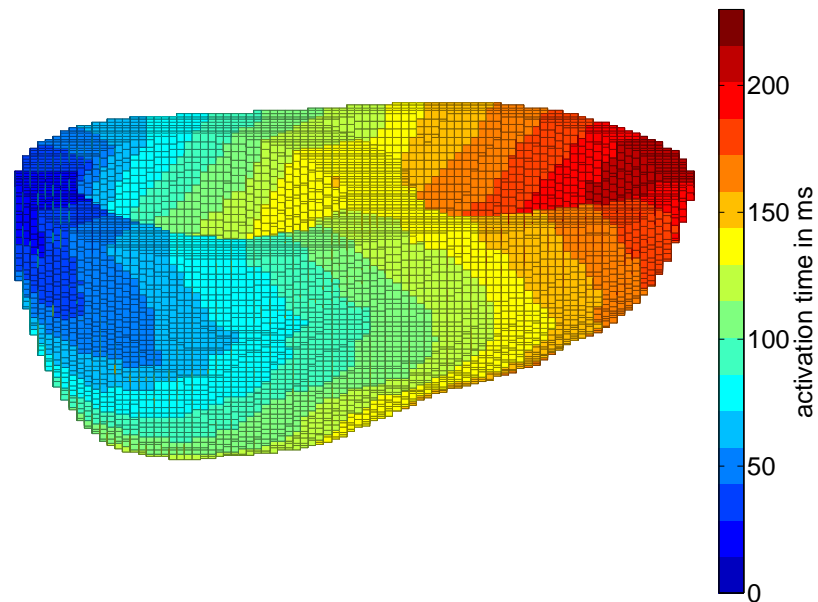


Figure 6.30: (UKF, smoothed WMN) activation times of the pacer location BLW ($\varepsilon = 0.001$, $\bar{d} = 5.25$ mm, $RE = 0.024$, $RE_{signal} = 0.066$, $LE = 1.3$ mm).

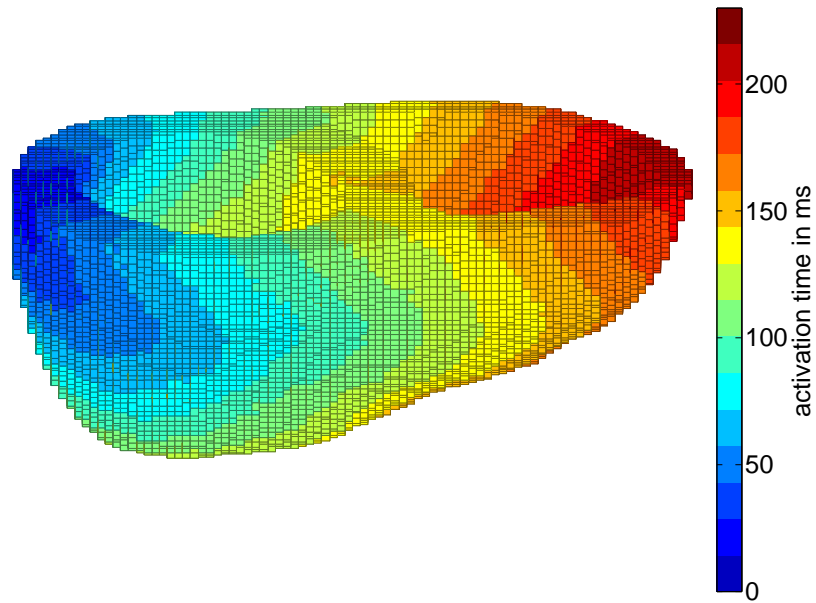


Figure 6.31: (EKF, MUSIC) activation times of the pacer location BLW ($\varepsilon = 0.001$, $\bar{d} = 5.25 \text{ mm}$, $RE = 0.034$, $RE_{signal} = 0.072$, $LE = 1.4 \text{ mm}$).

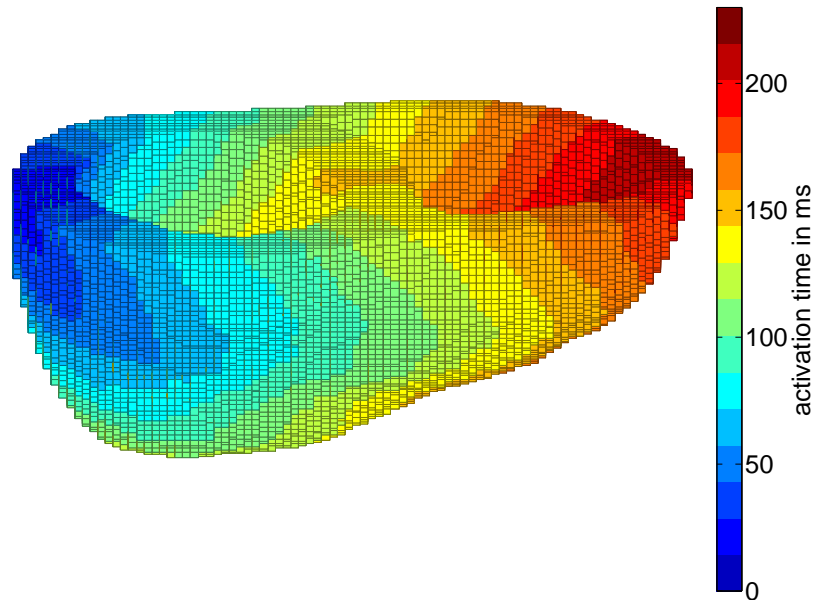


Figure 6.32: (UKF, MUSIC) activation times of the pacer location BLW ($\varepsilon = 0.001$, $\bar{d} = 5.25 \text{ mm}$, $RE = 0.024$, $RE_{signal} = 0.066$, $LE = 1.2 \text{ mm}$).

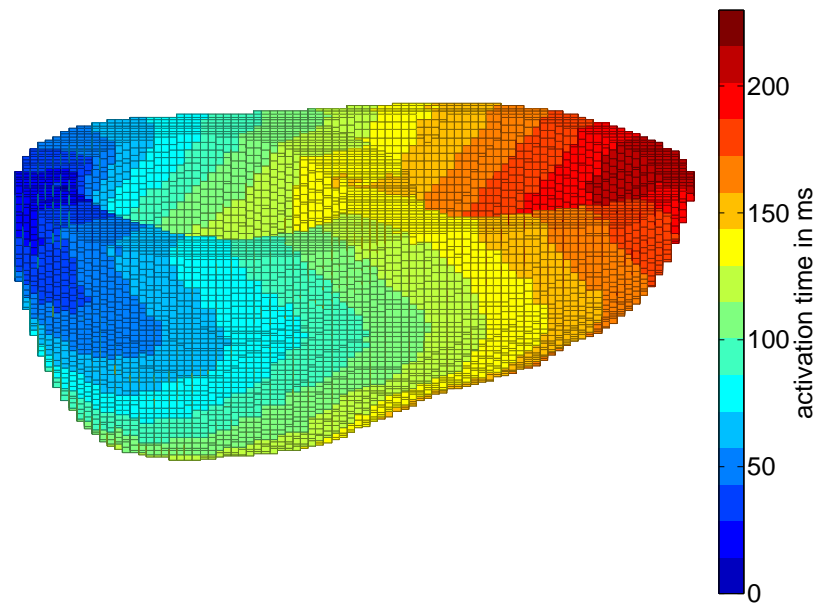


Figure 6.33: (EKF, hybrid) activation times of the pacer location BLW ($\varepsilon = 0.001$, $\bar{d} = 5.25 \text{ mm}$, $RE = 0.033$, $RE_{signal} = 0.081$, $LE = 6.2 \text{ mm}$).

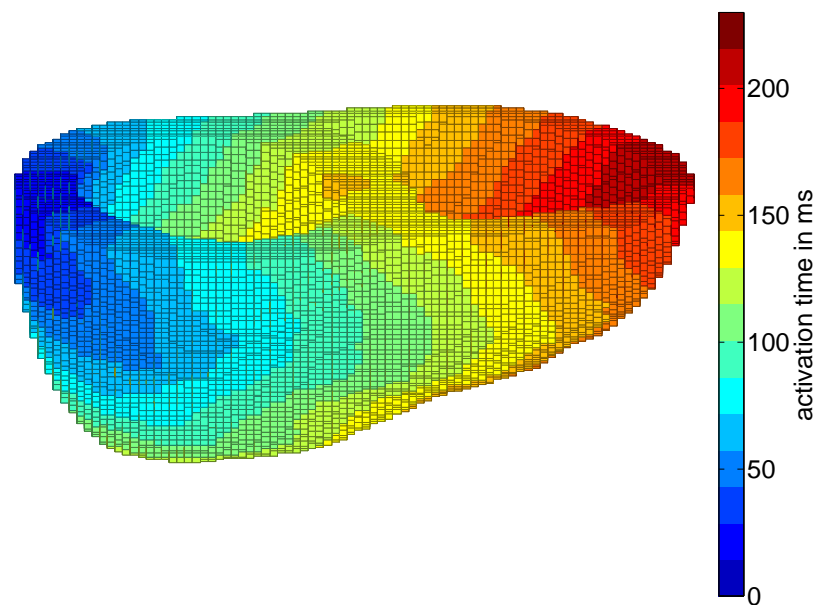


Figure 6.34: (UKF, hybrid) activation times of the pacer location BLW ($\varepsilon = 0.001$, $\bar{d} = 5.25 \text{ mm}$, $RE = 0.025$, $RE_{signal} = 0.066$, $LE = 4.4 \text{ mm}$).

6.2.5 Results: Comparison of EKF and UKF for 2 pacers

In this section the Kalman Filters will be applied to the 7 pairs of pacers denoted in the tables 6.4 and 6.5 with a time delay between the pacers of 0 *ms* and 20 *ms*, respectively. Because an accurate localization of the 2 pacer locations was not possible with the MUSIC technique (section 6.1.5), here only the smoothed WMN technique will be investigated for the cases of 0 *ms* and 20 *ms* time delay between the pacers.

Figure 6.35 shows the convergence of the Relative Error RE averaged over the 7 pairs of pacers denoted in the table 6.4 for the smoothed WMN technique and a time delay of 0 *ms* (diamonds) and 20 *ms* (squares). The converged RE in figure 6.36 shows again that the UKF results in smaller Relative Errors than the EKF both for the case of a time delay of 0 *ms* and a time delay of 20 *ms* between the 2 pacers.

Figure 6.37 shows the convergence of the Localization Error LE averaged over the 7 pairs of pacers denoted in the table 6.4 for the smoothed WMN technique with and without a time delay between the pacers. Because the Localization Error is calculated from the minimum of the activation time map, LE corresponds to the first-mentioned pacer location (starting at $t = 0$ *ms*). In figure 6.38 the converged Localization Error LE at $k = 25$ averaged over the 7 pairs of pacers is shown and one can see that a time delay of 20 *ms* between the pacers reduces LE significantly compared to case of no time delay: For no time delay between the pacers the algorithm in some cases selects the second-mentioned pacer location for the calculation of LE which produces a significantly increased Localization Error. In figure 6.37 one can see that the Kalman Filters even increase the value of LE for the case of no time delay between the pacers.

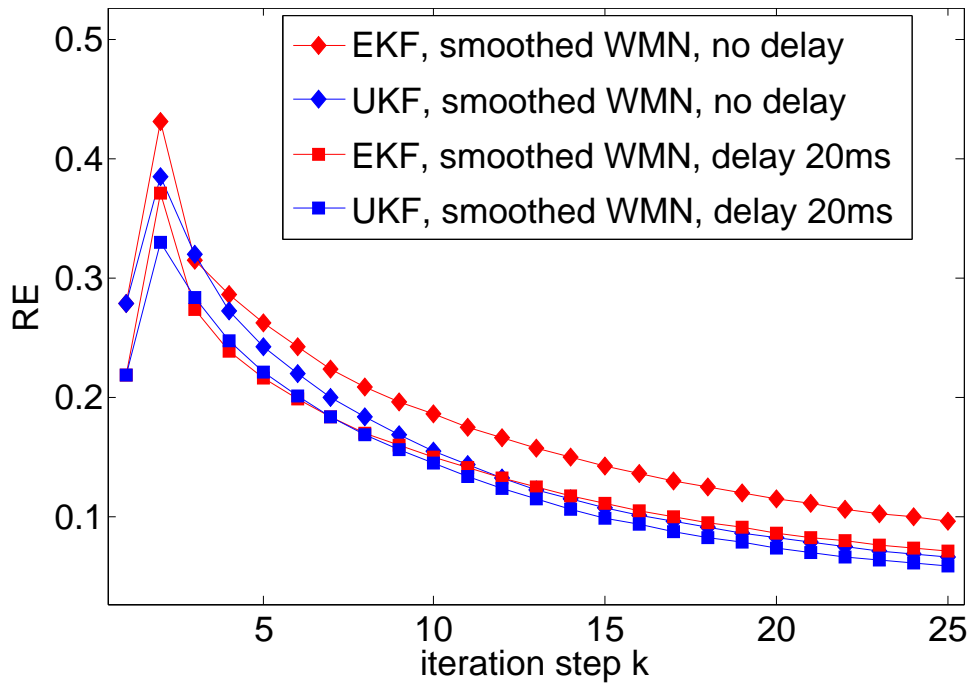


Figure 6.35: Convergence of RE for the 7 pairs of pacers of table 6.4 with and without time delay between the pacers ($SNR = 8.66 \times 10^3$, $\bar{d} = 5.25$ mm, $\varepsilon = 0.001$).

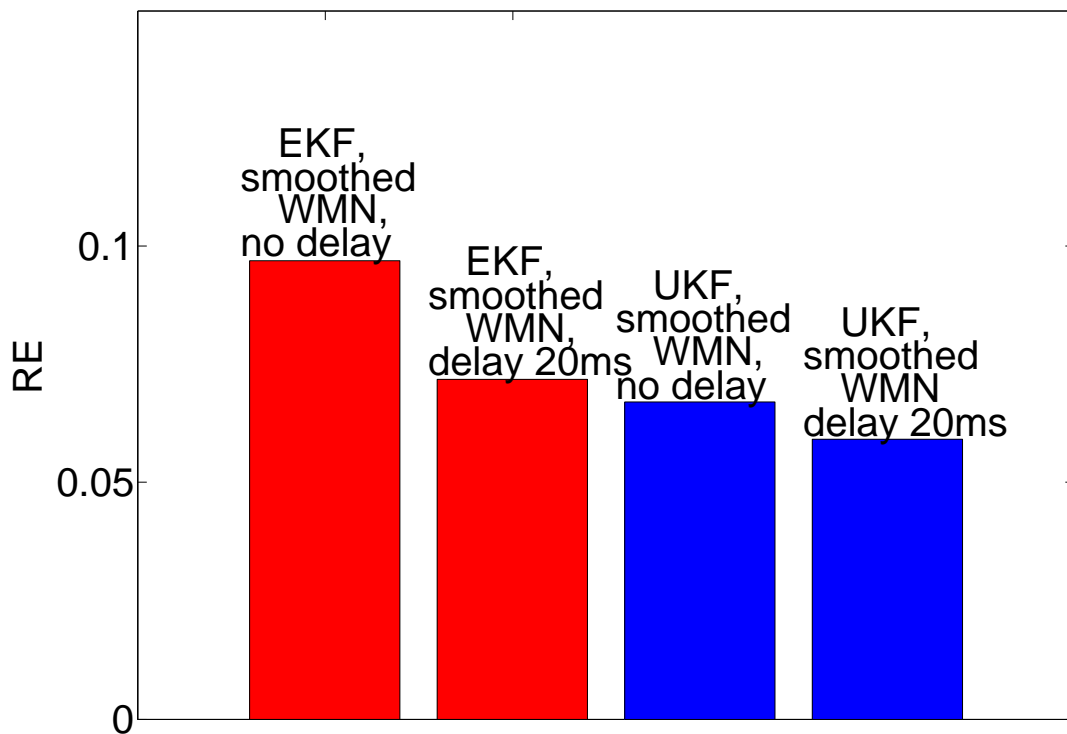


Figure 6.36: Converged RE ($k = 25$) for the 7 pairs of pacers of table 6.4 with and without time delay between the pacers ($SNR = 8.66 \times 10^3$, $\bar{d} = 5.25$ mm, $\varepsilon = 0.001$).

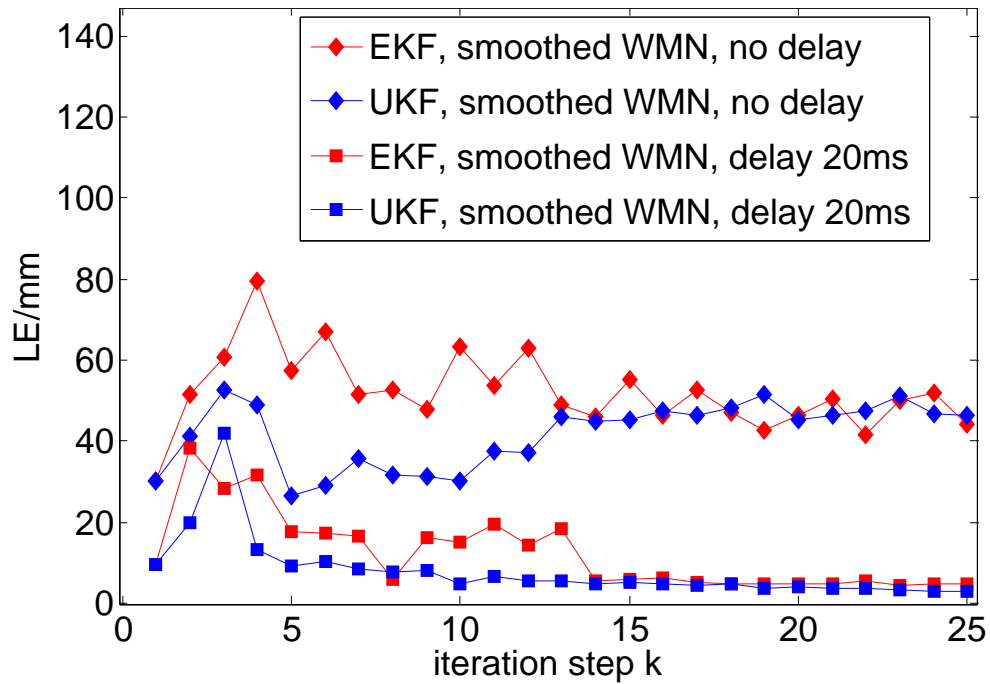


Figure 6.37: Convergence of LE for the 7 pairs of pacers of table 6.4 with and without time delay between the pacers ($SNR = 8.66 \times 10^3$, $\bar{d} = 5.25$ mm, $\varepsilon = 0.001$).

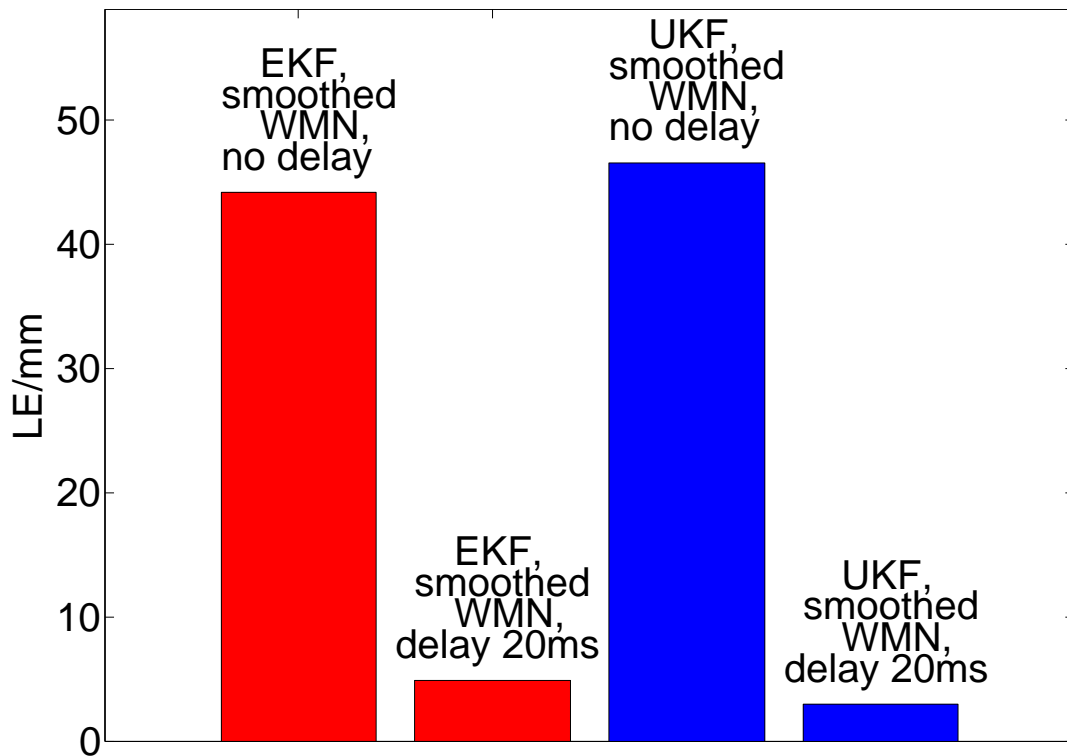


Figure 6.38: Converged LE ($k = 25$) for the 7 pairs of pacers of table 6.4 with and without time delay between the pacers ($SNR = 8.66 \times 10^3$, $\bar{d} = 5.25$ mm, $\varepsilon = 0.001$).

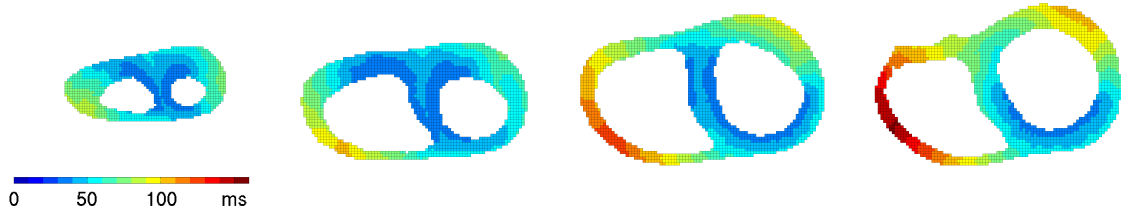


Figure 6.39: Healthy heart activation time model used for the simulations in this section, top views, horizontal planes from apex (left) to base (right) with a distance of 1.5 *cm*.

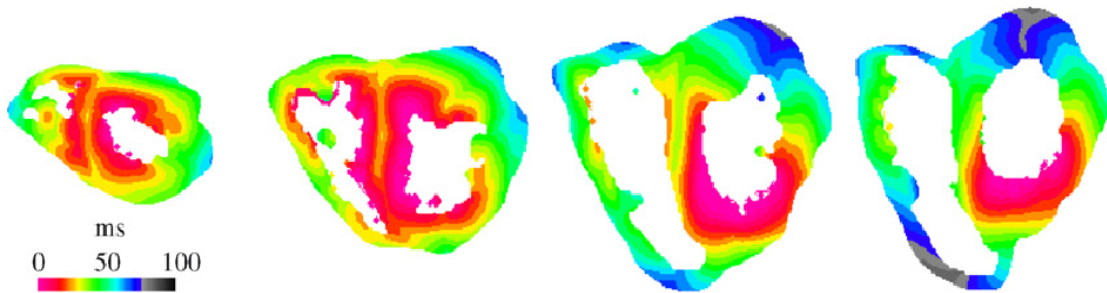


Figure 6.40: Measured healthy heart activation times of [13] [14], top views, horizontal planes from apex (left) to base (right) with a distance of 1 *cm*.

6.3 Healthy heart and fusion beats

6.3.1 Healthy heart depolarization times

In the sections 6.1 and 6.2 only the heart activation starting from a single pacing location has been simulated and reconstructed. In the medical applications the patient has an additional normal healthy heart activation too. The normal healthy heart activation times have been investigated experimentally in [13] with invasive electrode (needle) measurements in isolated human hearts. The results of [13] are that the depolarization of the ventricular muscle cells starts from the endocardial surface in the septum. Then first the apex is activated and the depolarization proceeds in the the direction from endocardium to epicardium and apex to base ([14] and figures 6.40 and 6.42). The experimental healthy heart activation times of 6.40 and 6.42 are used to generate the healthy activation times in the ventricular model with $n = 53476$ voxels: a part of the endocardial surface is activated at the same time ($t = 30$ *ms*), in a way that the activation times of figure 6.40 and 6.39 and also figure 6.42 and 6.41 look similar (the different color schemes have to be considered carefully).

6.3.2 Definition of a fusion beat

The typical time interval of a delta wave in Wolff-Parkinson-White syndrome is 20 – 30 *ms* [2]. After this time interval the activation of the accessory pathway

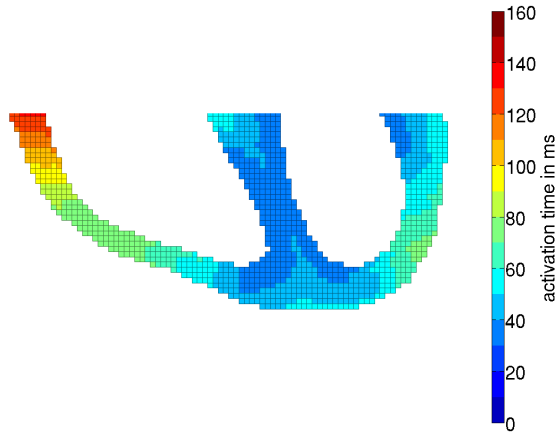


Figure 6.41: Healthy heart activation time model used for the simulations in this section, side view.

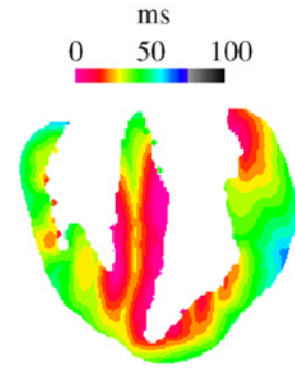


Figure 6.42: Measured healthy heart activation times of [13] [14], side view.

and the healthy activation are mixed. This kind of heart beat will be called a fusion beat. To generate the corresponding activation times of the fusion beat in the cellular automaton model first at $t = 0 \text{ ms}$ one of the pacers of figure 6.1 is activated and then at $t = 30 \text{ ms}$ the initial parts of the endocardial surface of the healthy heart model (figures 6.39 and 6.41) are activated. The rest of the activation times is again calculated with the cellular automaton model. Figure 6.43 exemplarily shows the fusion beat of the pacer location BRW. The depolarization wavefronts of the pacer and the healthy activation reach each other and overlap for instance in the yellow area with activation times $90 \text{ ms} < \tau(\mathbf{r}) < 100 \text{ ms}$ in the right ventricle. Figure 6.44 shows the healthy activation times for the purpose of comparison.

6.3.3 Calculation of the initial states for the fusion beats

In this section the reconstruction of the initial states for the fusion beats will be investigated. The initial states WMN and smoothed WMN are calculated in the same way as in section 6.1. For the parameters of the smoothing process function \mathbf{f} there have been assumed the same optimal values ($\varepsilon = 0.001$ and $\bar{d} = 5.25 \text{ mm}$). Because there is a strong overlap between the depolarization wavefronts of the pacer and the healthy activation for $t > 30 \text{ ms}$, the time interval for the calculation of the Localization Error LE (equation 6.2) has been chosen to be smaller: $\Delta t = 2 \text{ ms}$. This strong overlap between the healthy activation (starting mainly from the endocardium of the left ventricle) and the pacer activation is even visible in the smoothed WMN activation times of the right ventricular pacer location BRW which is shown in figure 6.45: The dark blue area with activation time $40 \text{ ms} < \tau(\mathbf{r}) < 50 \text{ ms}$ is spatially extended over big parts of the left and the right ventricle, although these activation times are only 3 ms above the minimum $\tau_{min} = 37 \text{ ms}$ of this map.

While the smoothed WMN initial state only incorporates information of the measured data and the smoothing process function \mathbf{f} , the MUSIC technique here also

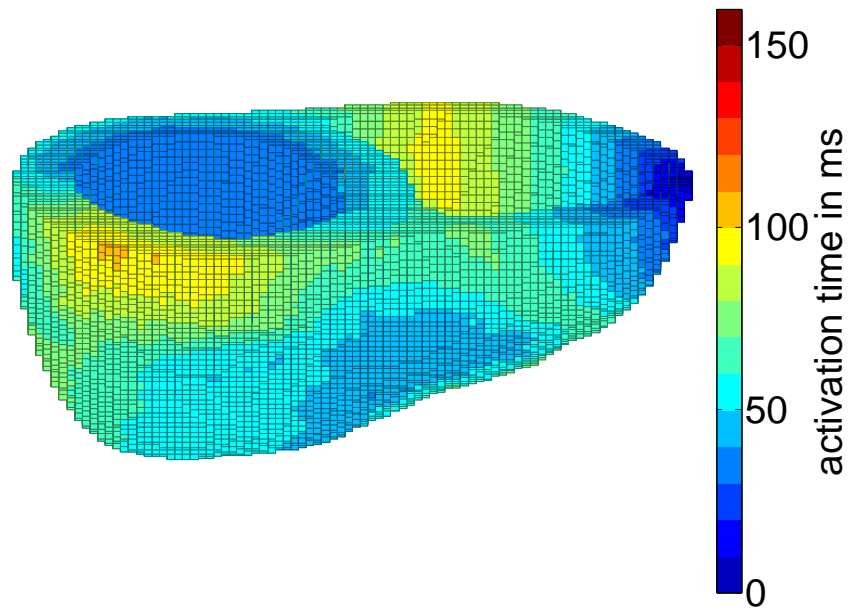


Figure 6.43: True (=simulated) activation times of the fusion beat (BRW + healthy). The pacer BRW starts at $t = 0$ ms, the healthy activation at $t = 30$ ms.

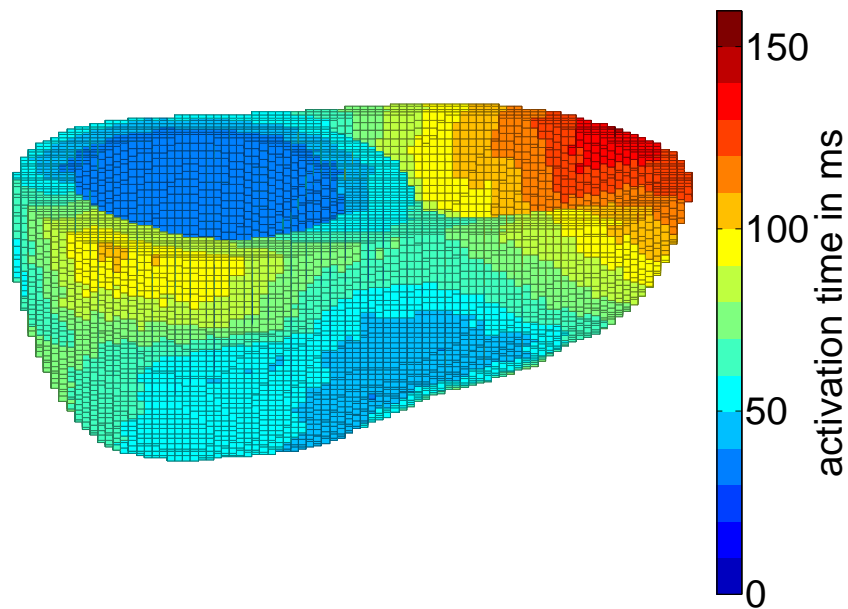


Figure 6.44: True (=simulated) activation times of the healthy heart model. The healthy activation starts at $t = 30$ ms.

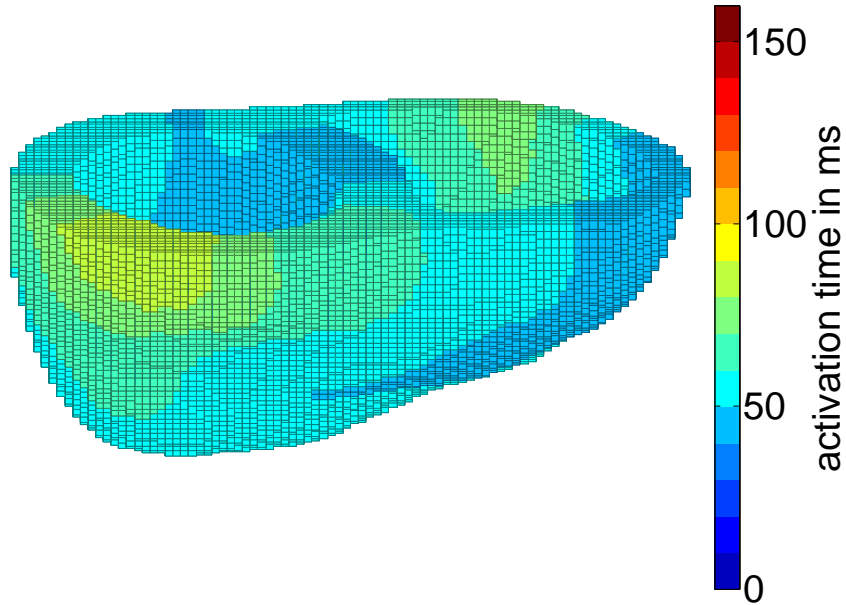


Figure 6.45: Smoothed WMN activation times of the fusion beat (BRW + healthy), $RE = 0.203$.

includes information of the healthy activation times. So the MUSIC initial state is here calculated in the following way: first the pacer is localized as in section 6.1 from the data of the initial time interval $\overline{\Delta t} = 12 \text{ ms}$. Then the calculated MUSIC location is activated at $t = 0 \text{ ms}$ and the endocardial surfaces of the healthy heart model at $t = 30 \text{ ms}$ and in the last step the fused activation times are calculated with the cellular automaton model.

Because there is a lot of information of the healthy heart model included in the MUSIC technique, the MUSIC activation times of figure 6.46 ($RE = 0.052$) are closer to the true fusion beat of figure 6.43, especially in the left ventricular region, than the smoothed WMN times ($RE = 0.203$). This type of MUSIC technique for the activation times of a fusion beat can only be applied if there is only a focal defect (focal ventricular tachyarrhythmia or WPW) in the heart. If the pathological changes of the healthy activation times are more spatially extended, for instance like in cardiac ischemia [45], the activation times of the healthy heart model cannot be included and the MUSIC technique will produce more inaccurate results.

6.3.4 Results: Comparison of EKF and UKF for fusion beats

In this section the Kalman Filters will be applied to the initial states of the fusion beats investigated in the last section. Because [8] doesn't take into account the healthy heart activation in the estimation of the EKF activation times, these are

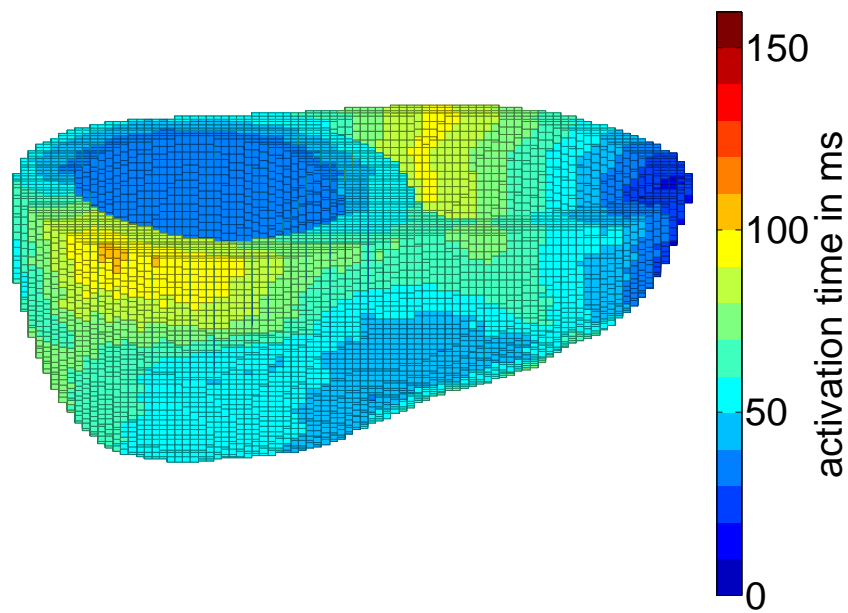


Figure 6.46: MUSIC activation times of the fusion beat (BRW + healthy), $RE = 0.052$.

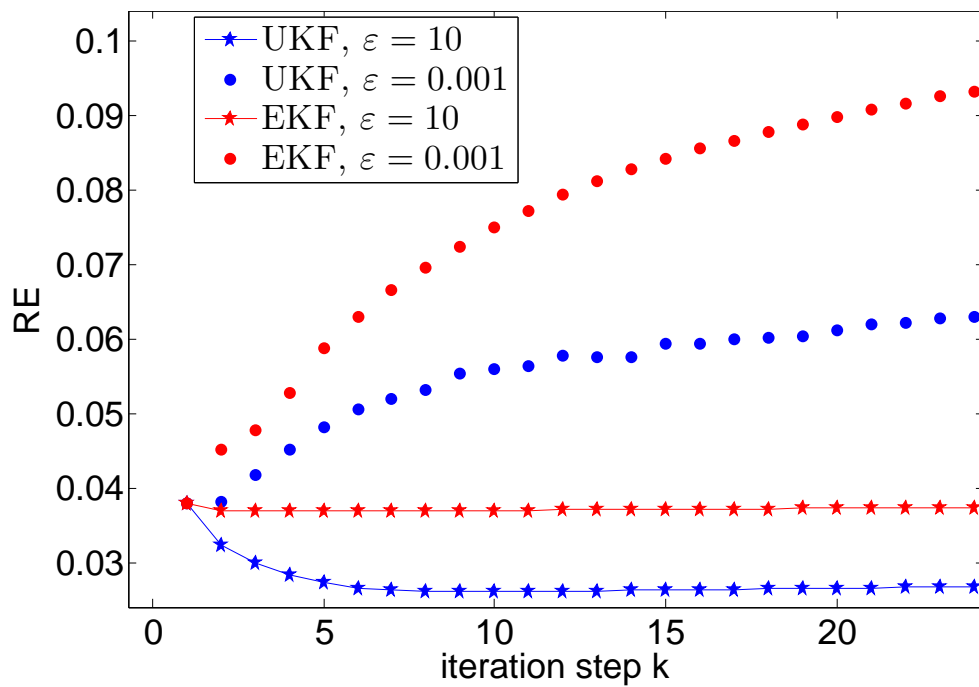


Figure 6.47: Convergence of RE (pacer BP, MUSIC) as a function of the Kalman Filter iteration step k for different smoothing values ε (equation (6.9)). RE is increased for strong smoothing $\varepsilon = 0.001$ and reduced for weak smoothing $\varepsilon = 10$.

new results in the research of 3D activation time estimations using Kalman Filters. The results are averaged over the 12 pacer locations of figure 6.1. Only the initial states smoothed WMN and MUSIC have been investigated, because the hybrid initial state doesn't provide a significant reduction of the errors RE and LE (section 6.2, figures 6.24 and 6.26). In contrast to the single pacer simulations of section 6.2.4, where a strong smoothing $\varepsilon = 0.001$ was used (see appendix C, figures C.1 and C.2), here a weak smoothing $\varepsilon = 10$ produces smaller errors: figure 6.47 shows that both for the EKF and the UKF the Relative Error RE of a fusion beat (BRW, with initial state MUSIC) increases for strong smoothing $\varepsilon = 0.001$ and decreases for weak smoothing $\varepsilon = 10$. Because the activation times of the initial MUSIC state include information of the healthy activation times, they are quite close to the true activation times of the fusion beat, so a too strong smoothing of the activation time map generates a diverging RE^3 .

Figure 6.48 shows the convergence of the averaged Relative Error RE for the fusion beats as a function of the Kalman Filter iteration step k for the Kalman Filters EKF (red) and UKF (blue) and for the initial states smoothed WMN and MUSIC. Figure 6.49 shows the corresponding converged values of RE at the iteration step $k = 25$. Just as in the case of the single pacer simulations (figure 6.24) the inverse technique (UKF, MUSIC) provides the smallest RE . Also as in the case of the single pacer simulations the convergence curves of figure 6.49 show that the Kalman Filters have a problem with the initial states: RE increases at the first iteration step.

Figure 6.50 shows the convergence of the Localization Error LE for the fusion beats as a function of the iteration step k . Figure 6.51 shows the converged values of LE at the iteration step $k = 25$. In contrast to the results for RE the Localization Error LE reaches the smallest value for the inverse technique (UKF, smoothed WMN). In figure 6.50 it can also be seen that the convergence of the Localization Error LE is more stable for the Kalman Filter UKF than for the Kalman Filter EKF. For the case of the technique (EKF, MUSIC) the Localization Error LE even increases, so the technique (EKF, MUSIC) cannot be applied for the localization of accessory pathways in fusion beats.

Figure 6.52 shows the convergence of the Relative Error of the measured MCG signal RE_{signal} . Figure 6.53 shows the corresponding converged value of RE_{signal} at the iteration step $k = 25$. Again the inverse technique (UKF, MUSIC) provides the smallest value of the Relative Error RE_{signal} . Figure 6.53 also shows that the MUSIC initial state provides much better results for the fusion beats than the smoothed WMN initial state: because the MUSIC technique includes much more physiological information of the healthy activation times than the smoothed WMN technique, the MCG signal is much more accurate for the case of the MUSIC state.

³In contrast to the single pacer activation times, the healthy activation times do not fulfil $\mathbf{f}(\mathbf{x}) = \mathbf{x}$ for $\varepsilon = 0.001$.

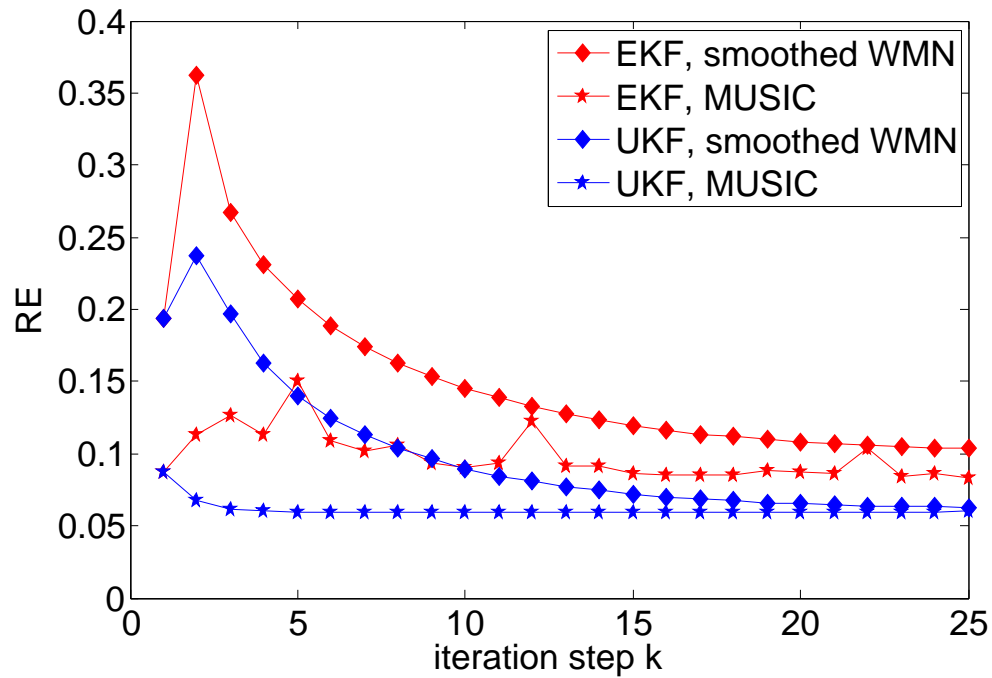


Figure 6.48: RE averaged over the 12 pacer locations as a function of the Kalman Filter iteration step k for the fusion beats ($SNR = 8.66 \times 10^3$, $\bar{d} = 5.25$ mm, $\varepsilon = 10$).

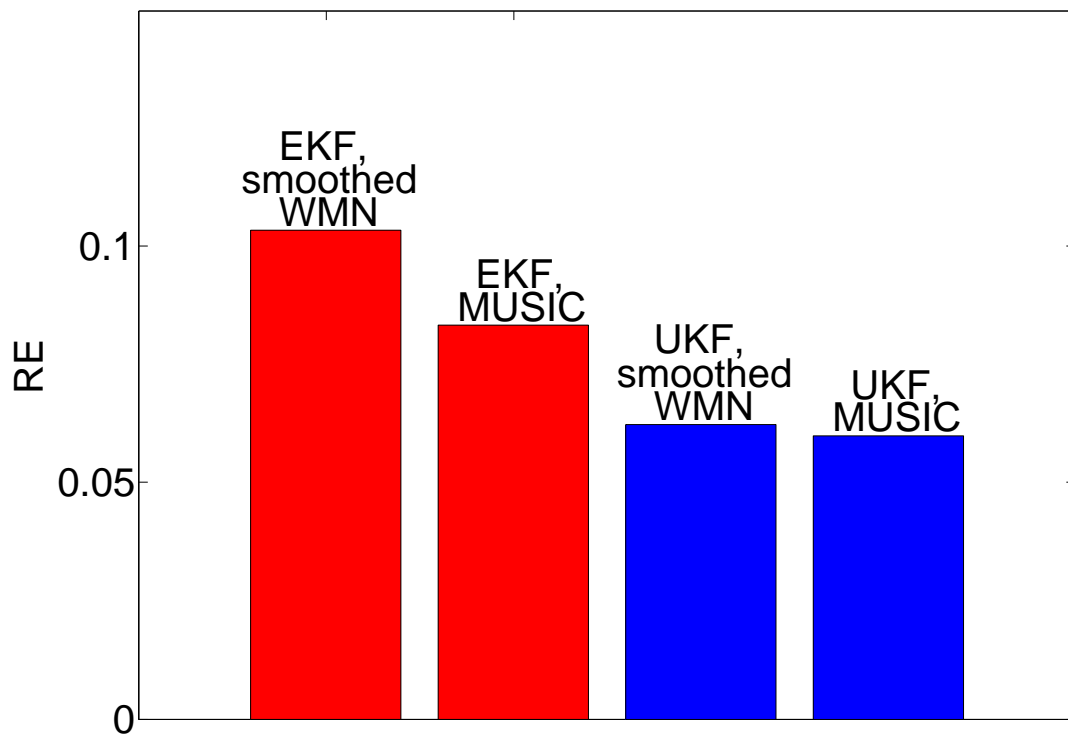


Figure 6.49: Converged RE ($k = 25$) averaged over the 12 pacer locations for the fusion beats ($SNR = 8.66 \times 10^3$, $\bar{d} = 5.25$ mm, $\varepsilon = 10$).

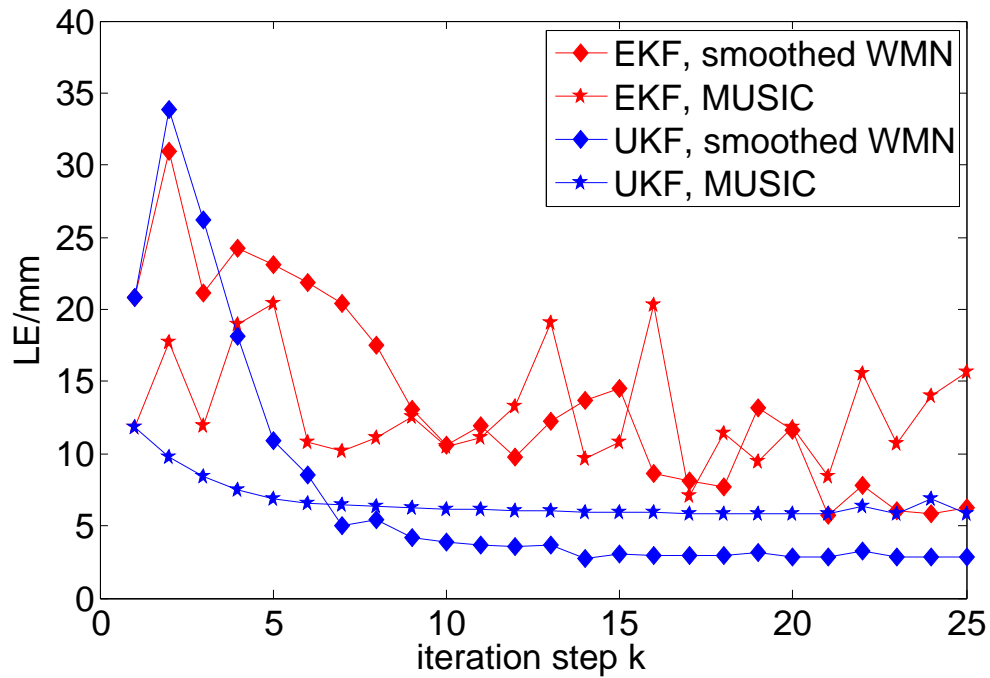


Figure 6.50: LE averaged over the 12 pacer locations as a function of the Kalman Filter iteration step k for the fusion beats ($SNR = 8.66 \times 10^3$, $\bar{d} = 5.25$ mm, $\varepsilon = 10$).

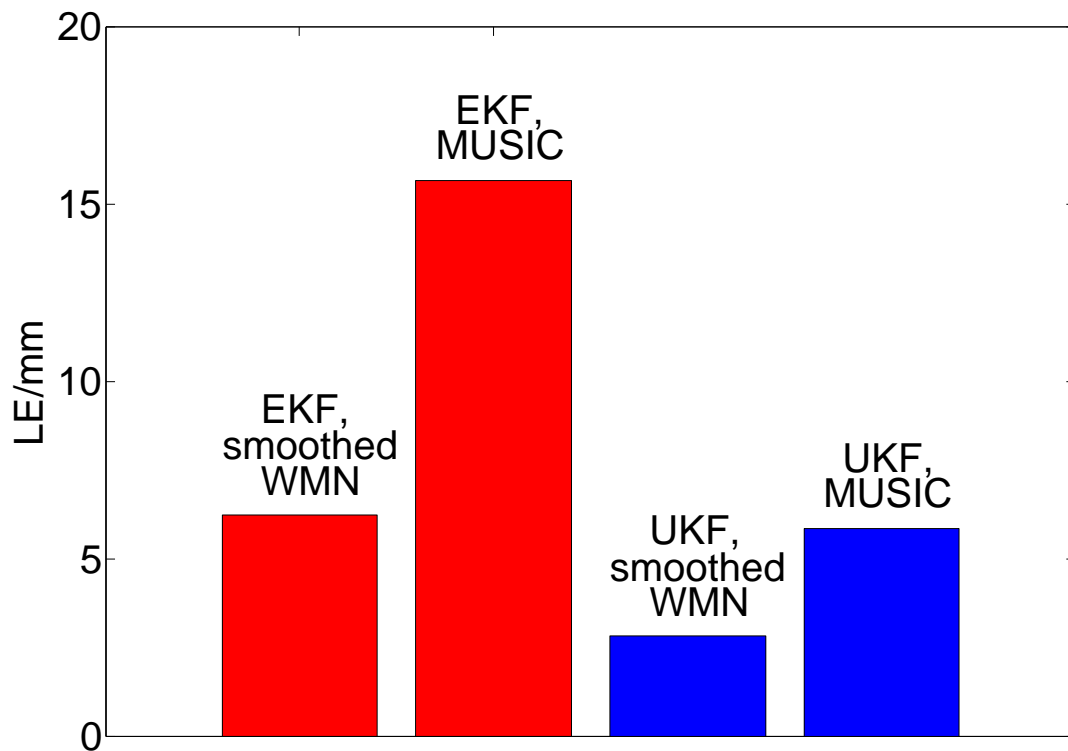


Figure 6.51: Converged LE ($k = 25$) averaged over the 12 pacer locations for the fusion beats ($SNR = 8.66 \times 10^3$, $\bar{d} = 5.25$ mm, $\varepsilon = 10$).

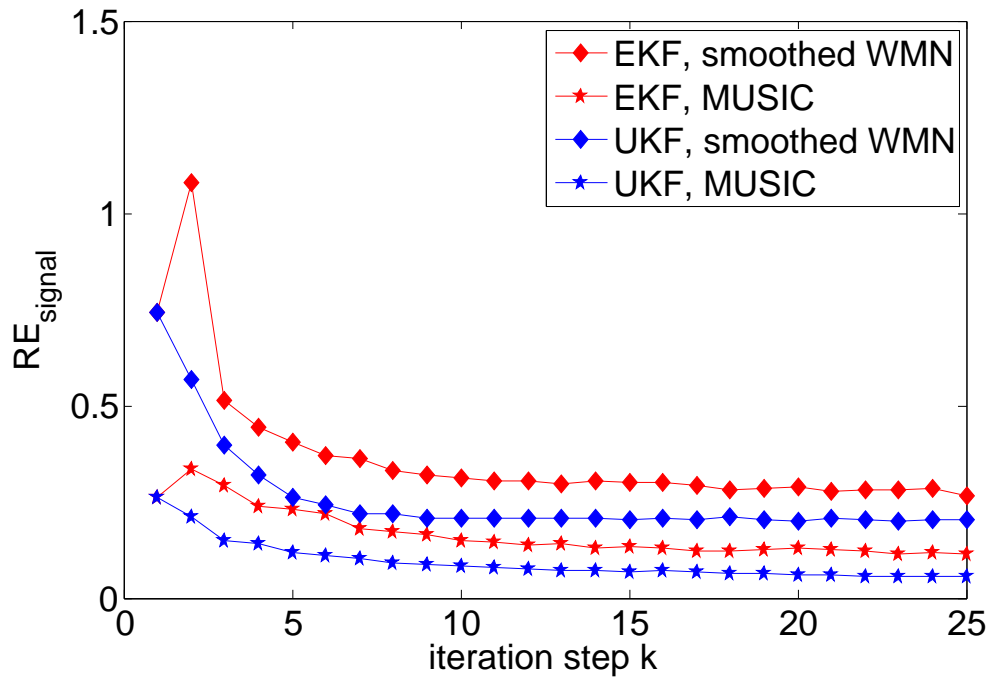


Figure 6.52: RE_{signal} averaged over the 12 pacer locations as a function of the iteration step k for the fusion beats ($SNR = 8.66 \times 10^3$, $\bar{d} = 5.25$ mm, $\varepsilon = 10$).

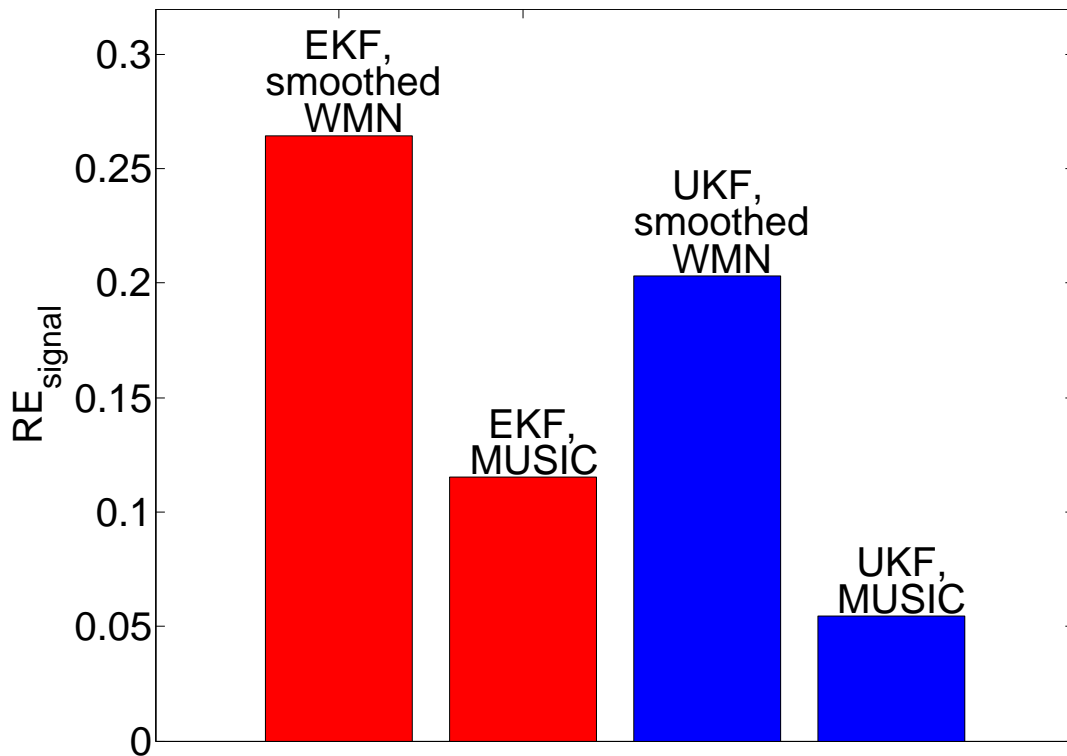


Figure 6.53: Converged RE_{signal} ($k = 25$) averaged over the 12 pacer locations for the fusion beats ($SNR = 8.66 \times 10^3$, $\bar{d} = 5.25$ mm, $\varepsilon = 10$).

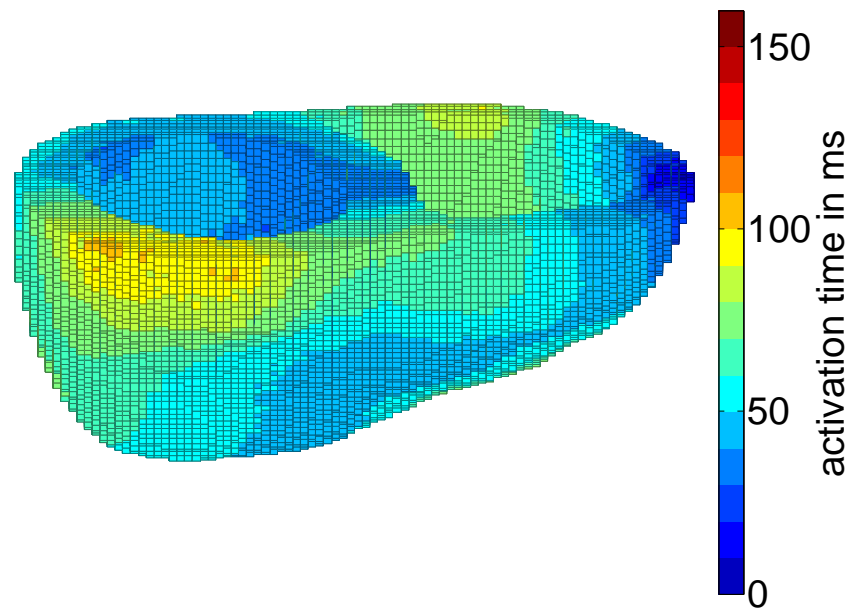


Figure 6.54: (EKF,smoothed WMN) activation times of the fusion beat for the pacer location BRW ($RE = 0.126$).

The figures 6.54 to 6.57 show the converged Kalman Filter activation times at the iteration step $k = 25$ exemplarily for the fusion beat of the pacer location BRW. By comparison of the Relative Errors RE and by comparison with the true activation times of figure 6.43 one can see that also after the application of the Kalman Filters EKF and UKF the activation times of the MUSIC initial state provide a better estimate for the true activation times than the smoothed WMN initial state: The figures 6.54 and 6.55 show that the Kalman Filters with smoothed WMN initial state have problems in estimating the true activation times, especially the healthy activation times in the left ventricular regions.

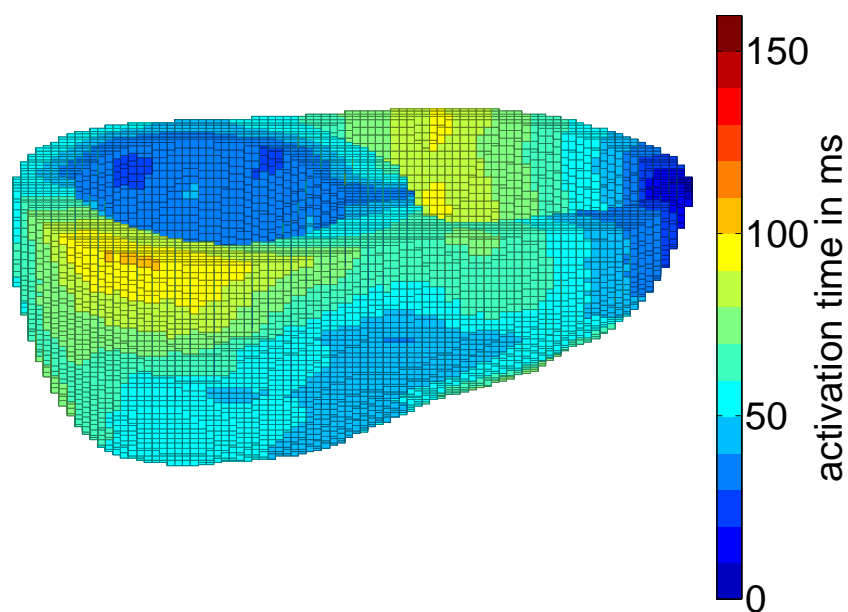


Figure 6.55: (UKF,smoothed WMN) activation times of the fusion beat for the pacer location BRW ($RE = 0.081$).

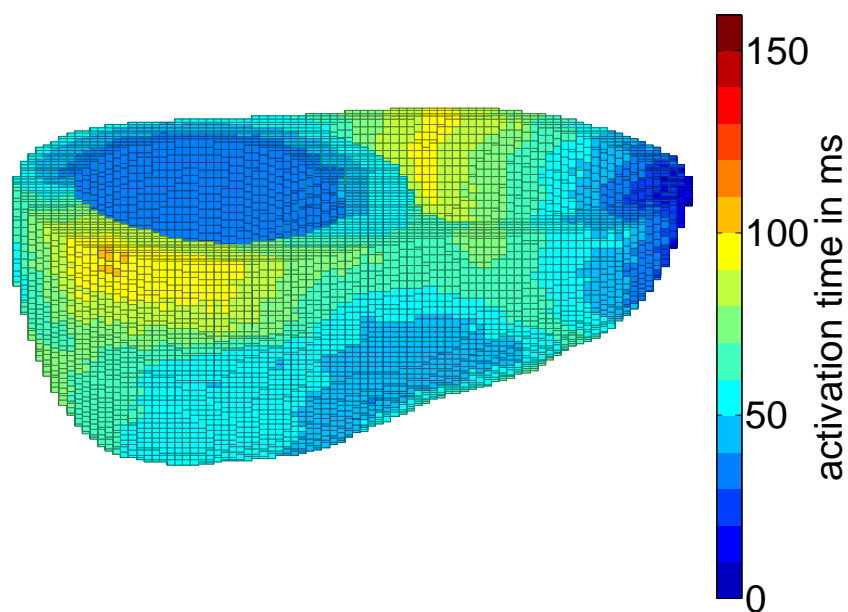


Figure 6.56: (EKF,MUSIC) activation times of the fusion beat for the pacer location BRW ($RE = 0.049$).

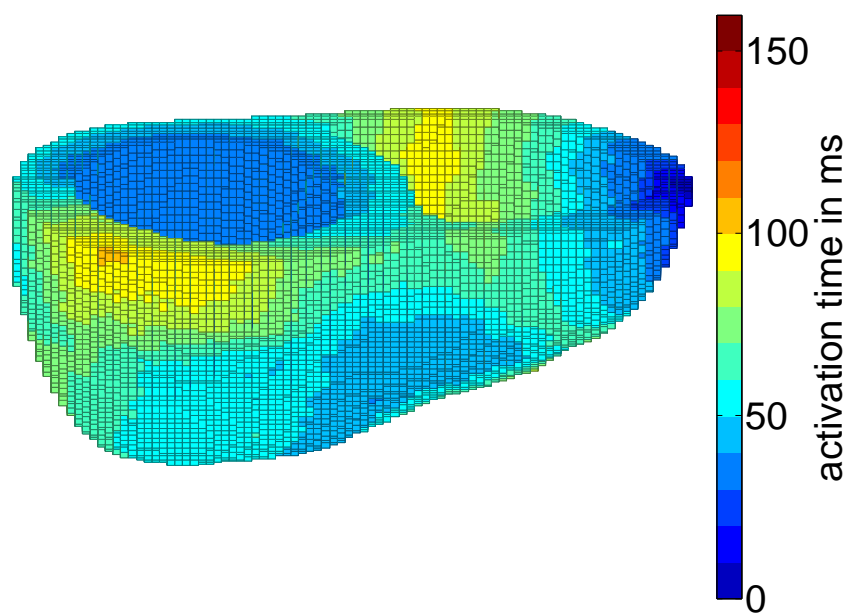


Figure 6.57: (UKF,MUSIC) activation times of the fusion beat for the pacer location BRW ($RE = 0.031$).

Chapter 7

Discussion and outlook

The results shown in chapter 6 clearly demonstrate that the Unscented Kalman Filter is superior to the Extended Kalman Filter in estimating the activation times of the heart: Both the global Relative Errors of the activation times and the Localization Errors of the pacer locations are smaller in case of the Unscented Kalman Filter than in case of the Extended Kalman Filter. E.g. in case of the single pacers stimulations the technique (UKF,MUSIC) provides an averaged Localization Error of $\sim 1.2 \text{ mm}$ (see figure 6.26), while both the averaged Localization Error (EKF,smoothed WMN) in this work and the EKF-WMN result in [8] are of the order $\sim 3 \text{ mm}$. So the new main improvement of this work in comparison to recent works like [8] is the introduction of the UKF for the solution of the nonlinear state-space model of cardiac activation time imaging.

Additionally, the Unscented Kalman Filter provides smaller errors than the Extended Kalman Filter also in more complex stimulation cases (2 pacer stimulation and fusion beats). The reason for this is assumed to be the non-smooth nature of the process and measurement function in the state-space model and the higher order of the Unscented Kalman Filter estimation. Especially the Kalman Filter solutions for the more realistic fusion beats (healthy activation times superimposed with the accessory pathway activation times) have not been investigated in [8], so they represent a further new investigation of this thesis. Nevertheless, it has to be tested whether the UKF is a better approach than the EKF for other types of non-smooth process functions. Because in other applications of electrical engineering¹ it has been shown that the EKF can also be superior to the UKF [43], the performance of the Kalman Filters has to be compared separately for every type of nonlinear state-space model.

In this work the parameters of the Kalman Filters have been estimated with convergence tests. Because of the huge number of cells ($n \approx 50000$) in the ventricular model a statistical estimation of the parameters from the measured data, e.g. with the Expectation-Maximization (EM) method [47], was computationally too expensive and couldn't be investigated in this work: The computational time for the UKF convergence curve of the length $k = 25$ was ~ 1.5 days on 48 processors in parallel for one single pacer. In practice the parameters need to be estimated from the measured

¹The UKF and EKF are also used e.g. in the framework of GPS navigation [46].

data with statistical methods (see appendix C for detailed information on statistically estimating parameters from the data). In order to apply the UKF in practice there need to be done some numerical improvements to increase the computational speed of the algorithm. Suggestions to reduce the computational effort of the UKF without reducing the accuracy of the estimation have been made e.g. in [48] and [49].

In chapter 5 of this work it has been shown that an array with MCG sensors placed at the anterior and at the posterior side of the torso results in the smallest Localization Errors compared with anterior and posterior double layer arrays. These are also new results because in [8] and [34] there were used arrays with anterior and posterior ECG electrodes (Body Surface Potential Mapping, BSPM) instead of MCG sensors, and in [2] the MCG sensors are only located in one plane anterior array. A reasonable extension of the sensor array with anterior and posterior sensors is a cylindrically shaped array with additional sensors placed on the left and the right side of the torso. In the master thesis [50] it has been shown that a cylindrically shaped sensor array provides further improvements, e.g. the suppression of external interference sources via the multipole expansion of the magnetic field [51].

This work was focused on the medical applications accessory pathway localization in Wolff-Parkinson-White syndrome and localization of focal ventricular tachycardia. A second very important medical application of magnetocardiography is the diagnosis of cardiac ischemia: it has been shown [52] that a diagnosis of cardiac ischemia with MCG is much more reliable than the diagnosis with the standard 12-channel ECG. Despite of that an application of activation time imaging to cardiac ischemia is hardly possible, because of the strong electrophysiological changes of the action potential in the ischemic regions (see section 6.3.3). Nevertheless, an application of the investigated Kalman Filters to the spatiotemporal imaging of primary current dipoles on a 2D heart surface could give promising results also in cardiac ischemia, if the underlying state-space model is chosen with enough degrees of freedom. Because of the importance of cardiac ischemia diagnosis in the medical practice this could be a research focus in future works.

Appendix A

Noise simulation

In this appendix it will be explained how the noise of the MCG sensors is simulated. Let m be the number of MCG sensors and N the number of data time samples (t_1, \dots, t_N). The ($m \cdot N \times 1$) MCG data vector

$$\boldsymbol{\phi} = \mathbf{h}(\mathbf{x}) + \mathbf{v} \quad (\text{A.1})$$

includes a ($m \cdot N \times 1$) vector \mathbf{v} representing the measurement error (e.g. due to noise of electronic devices) and the simulated MCG signal $\mathbf{h}(\mathbf{x})$. \mathbf{x} represents the true simulated activation times. In the simulations \mathbf{v} is white Gaussian noise and distributed with the help of normally distributed random numbers

$$\mathbf{v} = \sigma \cdot \mathbf{randn}(0, 1) \quad (\text{A.2})$$

where σ is the standard deviation of the noise and $\mathbf{randn}(0, 1)$ is a computer generated ($m \cdot N \times 1$) vector with normally distributed components with mean 0 and standard deviation 1.

The Signal to Noise Ratio SNR is defined with the help of the maximal signal power $\phi_{max} = \max_i\{|\phi_i|\}$

$$SNR := \frac{\phi_{max}}{\sigma}. \quad (\text{A.3})$$

Figure A.1 shows the noise $v_{p,t}$ of the sensor p at time t as a function of the time exemplarily for 3 different sensors. The standard deviation of the noise is $\sigma = 1$. Figure A.2 validates that the noise of different sensors is not correlated. The correlation between sensor q and sensor p can be described by the matrix elements

$$Corr_{qp} = \langle \mathbf{v}_q \cdot \mathbf{v}_p \rangle := \frac{1}{N} \sum_{i=1}^N v_{q,t_i} v_{p,t_i} \quad (\text{A.4})$$

which is the product of the measurement errors of the sensors q and p averaged over the time. Figure A.2 shows that the nondiagonal elements $Corr_{1p}$ ($p \neq 1$), describing the correlation between different sensors, are significantly smaller than the diagonal elements $Corr_{pp}$.

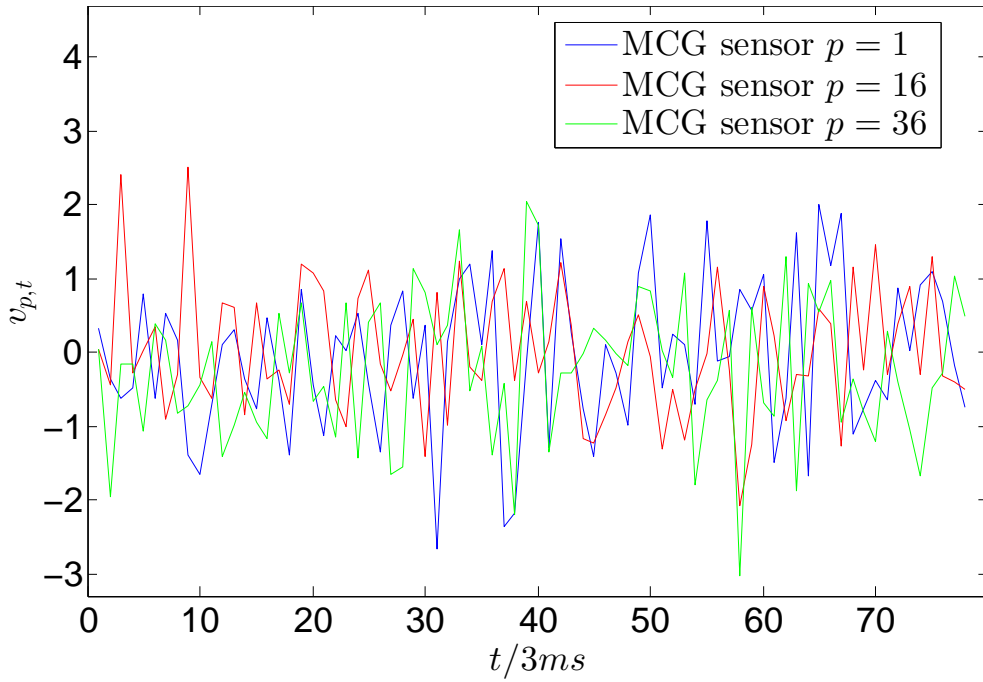


Figure A.1: The noise $v_{p,t}$ for sensor p and time t for 3 exemplarily chosen sensors, as a function of the time t with sampling rate $\delta t = 3 \text{ ms}$ ($\sigma = 1$, $N = 78$, data for pacer location BRW).

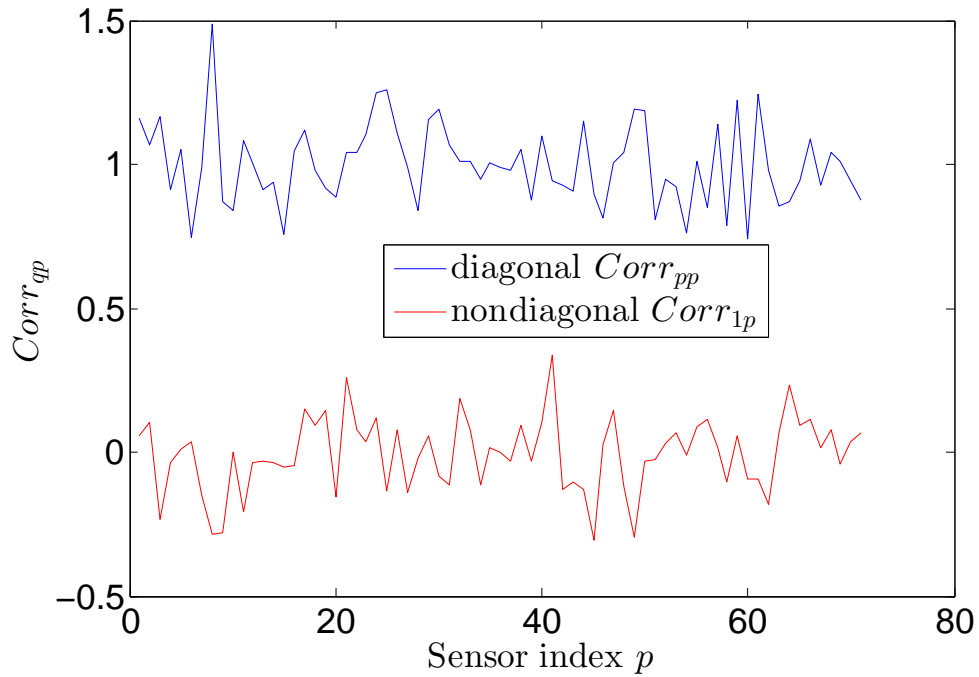


Figure A.2: Correlation $Corr_{qp} = \langle \mathbf{v}_q \cdot \mathbf{v}_p \rangle$ of the noise of sensor q and p (equation (A.4), $\sigma = 1$, $N = 78$, data for pacer location BRW).

Appendix B

Smoothing the WMN activation time maps

In this appendix it will be explained in detail how the initial activation times $\mathbf{x}_{smoothed\ WMN}$ of the smoothed WMN technique (section 6.1.1) are calculated. First the non-smoothed WMN activation times \mathbf{x}_{WMN} are calculated with the help of the equations (6.3) to (6.7). Then the non-smoothed activation times are used as the initial state $\mathbf{x}_{k=0} = \mathbf{x}_{WMN}$ of the recursive smoothing algorithm $\mathbf{x}_k = \mathbf{f}(\mathbf{x}_{k-1}), k = 1, 2, 3, \dots$. As shown in figure B.1 the recursive smoothing algorithm is applied in the interval $k = 1, \dots, 100$ and the minimum of the signal error RE_{signal} (equation (6.8)) is calculated. In figure B.1 the minimum $min(RE_{signal})$ is marked with a red line for the case of the pacer location BLW at iteration step $k = 6$. So for the case of the pacer location BLW the smoothed WMN activation times are $\mathbf{x}_{smoothed\ WMN} = \mathbf{x}_{k=6}$.

As can be seen in figure B.2 the Relative Error of the activation times RE is not in a minimum at $k = 6$. So the described procedure is only an approximation for finding the minimum of RE . A minimization of RE is not possible, because the true activation times \mathbf{x}_{true} , necessary to calculate RE , are not known in praxis. The calculation of RE_{signal} (equation (6.8)) is possible because it is independent of \mathbf{x}_{true} .

The Tables 6.1 and 6.2 show that RE and RE_{signal} both are reduced by the recursive smoothing algorithm for all the 12 pacer locations. Due to outliers some of the Localization Errors LE in table 6.3 (pacer locations BLW, MA, MS) are increased but the average LE is also reduced via the recursive smoothing algorithm.

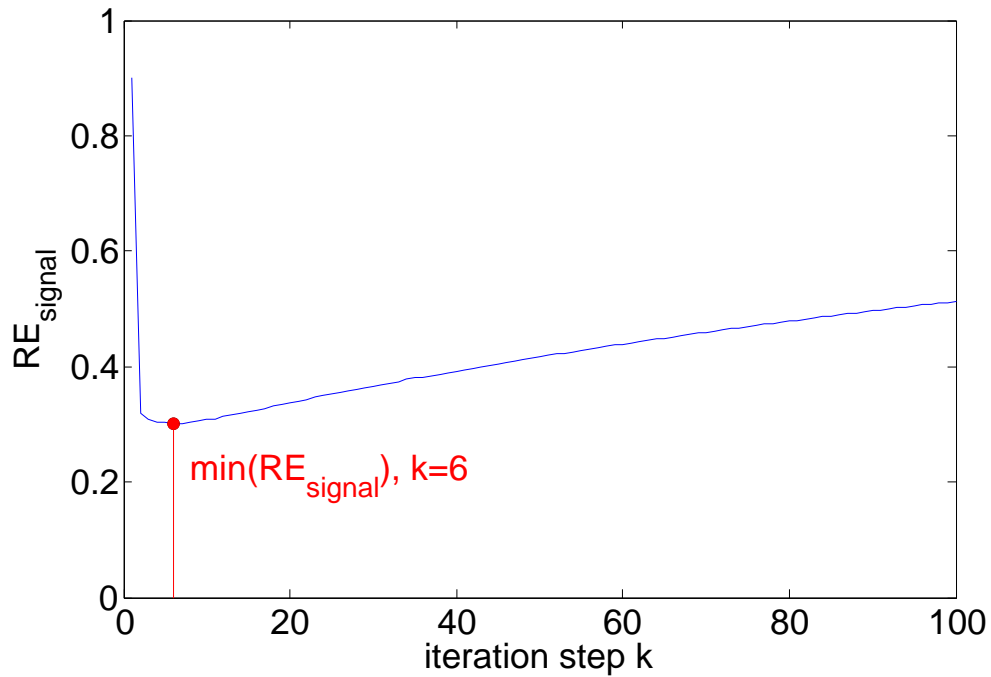


Figure B.1: RE_{signal} for the recursive smoothing algorithm $\mathbf{x}_k = \mathbf{f}(\mathbf{x}_{k-1})$ and the pacer location BLW. The minimum of RE_{signal} is reached at $k = 6$.

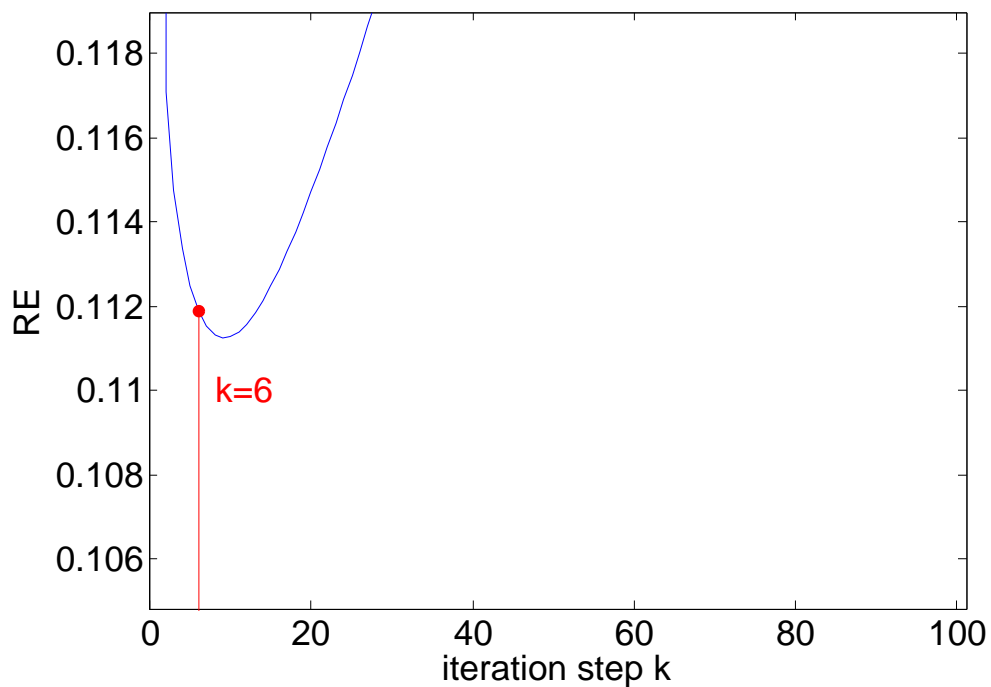


Figure B.2: RE for the recursive smoothing algorithm $\mathbf{x}_k = \mathbf{f}(\mathbf{x}_{k-1})$ and the pacer location BLW. The minimum of RE is reached at $k = 9$ but $k = 6$ is used for the calculation of $\mathbf{x}_{smoothed\ WMN}$.

Appendix C

Kalman Filter parameter tests

In this appendix some parameter tests for the Kalman Filter parameters $\Theta = (\alpha, \delta t, \varepsilon, \bar{d}, \mathbf{Q})$ will be presented. Unlike in other applications where the Kalman Filter parameters are estimated from the measured data with a Maximum Likelihood method, e.g. Expectation-Maximization (EM) [47], here the parameters will be estimated with optimizations of the Kalman Filters over the iteration step interval $k = 1, \dots, 25$. The problem of the parameter estimation with the Maximum Likelihood method here is the computational effort: to calculate the conditioned probability $p(\mathbf{y}|\Theta)$ of the data vector \mathbf{y} an integral over the state-space has to be solved: $p(\mathbf{y}|\Theta) = \int_{\Omega(\mathbf{y})} g(\mathbf{x}|\Theta) d^n \mathbf{x}$. Because the number of state-space variables is $n = 53476$ and g is a highly nonlinear function of \mathbf{x} , the integral could only be solved numerically with a non-acceptable computational time.

Figure C.1 shows the test for the parameter ε of the smoothing process function \mathbf{f} (equation (6.9)) and the UKF. Figure C.2 shows the test for ε and the EKF. A smaller value of ε means a stronger smoothing of the activation time map, so the convergence of RE is improved with decreasing ε . The optimum is $\varepsilon = 0.001$.

Figure C.3 shows the parameter test for the temporal difference δt in the difference quotients for the Jacobians (equation (6.17)) of the EKF. The best convergence of RE in the interval $k = 1, \dots, 25$ is reached for the temporal difference $\delta t = 4 \text{ ms}$. Figure C.4 shows the parameter test for the UKF parameter α that controls the spread of the sigma points (equation (6.24)). For a too big spread of the sigma points the first step increases so the convergence gets unstable. An optimal convergence of RE is reached for $\alpha = 2$.

Figures C.5 and C.6 show the parameter tests for the next neighborhood distance \bar{d} of the smoothing process function \mathbf{f} (equation (6.9)) for the EKF and UKF, respectively. In both cases the optimal convergence of RE is reached for $\bar{d} = 5.25 \text{ mm}$.

Figures C.7 and C.8 show the parameter test for the process covariance matrix $\mathbf{Q} = Q\mathbf{I}$ for the EKF and UKF, respectively. The optimal RE convergence of the EKF is reached for $Q = 0.1$, for the UKF for $Q = 1$.

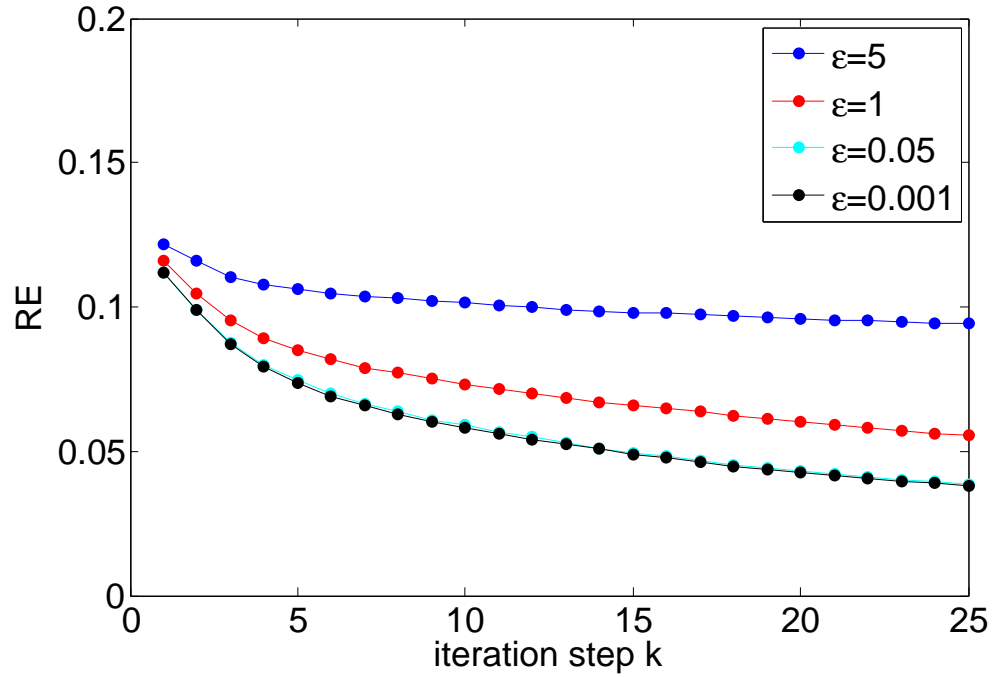


Figure C.1: Tests for smoothing parameter ε (equation (6.9)): UKF for pacer location BLW ($SNR = 8.66 \times 10^3$, $\bar{d} = 5.25$ mm, $\alpha = 2$, $Q=1$).

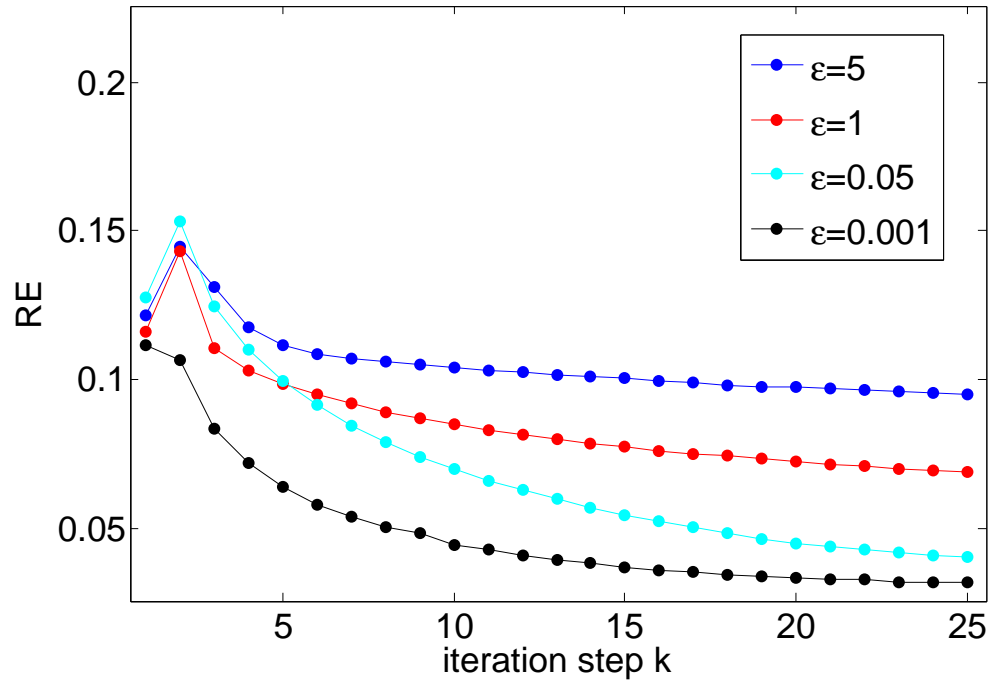


Figure C.2: Tests for smoothing parameter ε (equation (6.9)): EKF for pacer location BLW ($SNR = 8.66 \times 10^3$, $\bar{d} = 5.25$ mm, $\delta t = 4$ ms, $Q=0.1$).

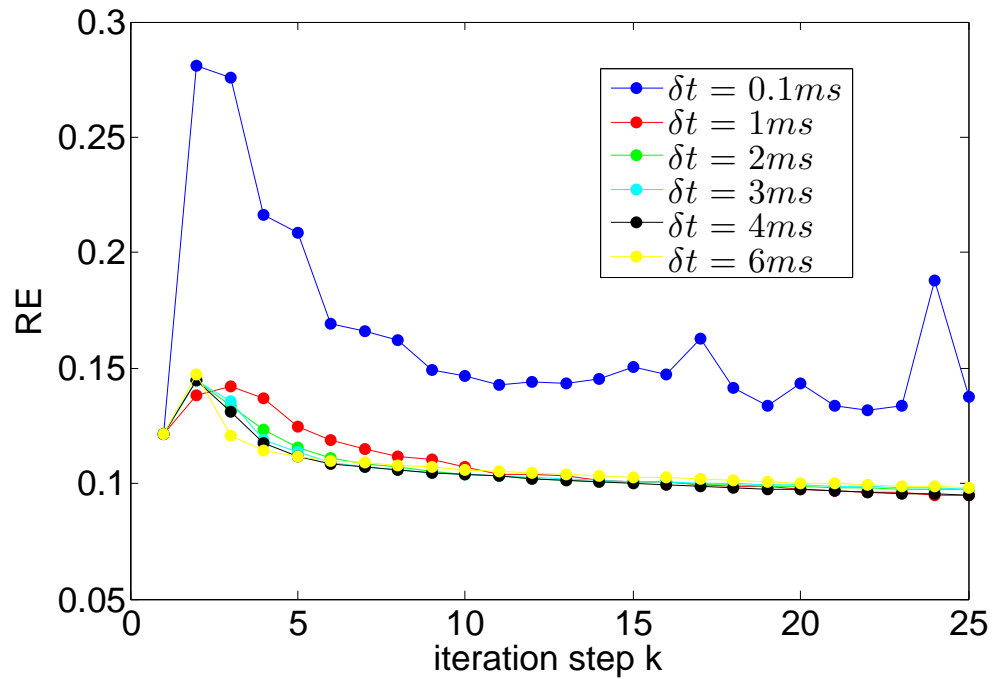


Figure C.3: Tests for the temporal step width δt for the calculation of the Jacobians (equation (6.17)): EKF for pacer location BLW ($SNR = 8.66 \times 10^3$, $\bar{d} = 5.25$ mm, $\varepsilon = 0.001$, $Q=0.1$).

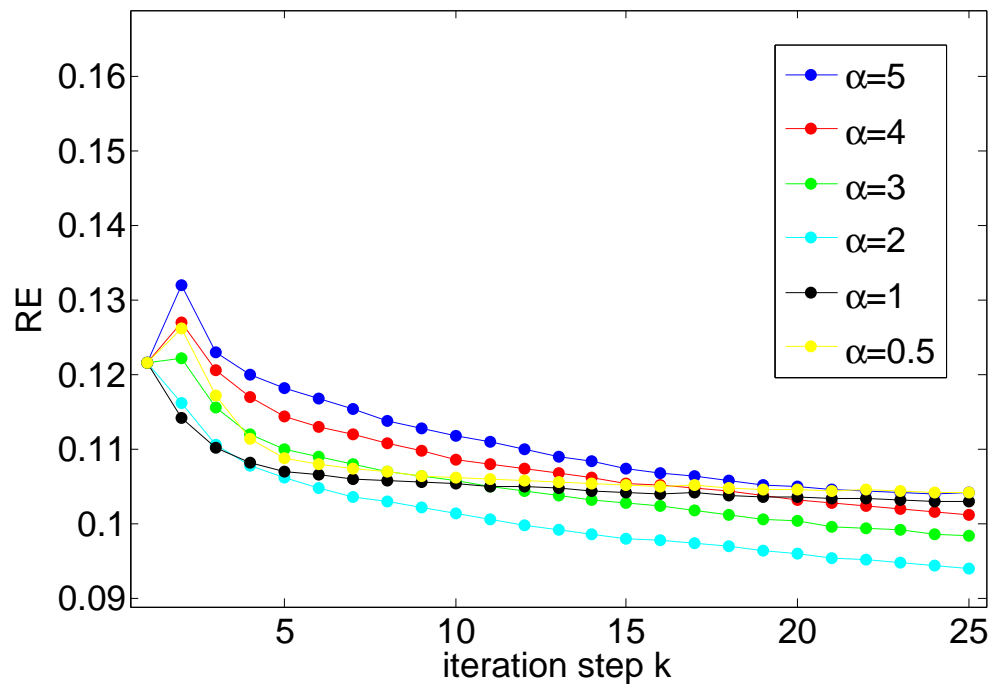


Figure C.4: Tests for the UKF parameter α (equation (6.24)): UKF for pacer location BLW ($SNR = 8.66 \times 10^3$, $\bar{d} = 5.25$ mm, $\varepsilon = 0.001$, $Q=1$).

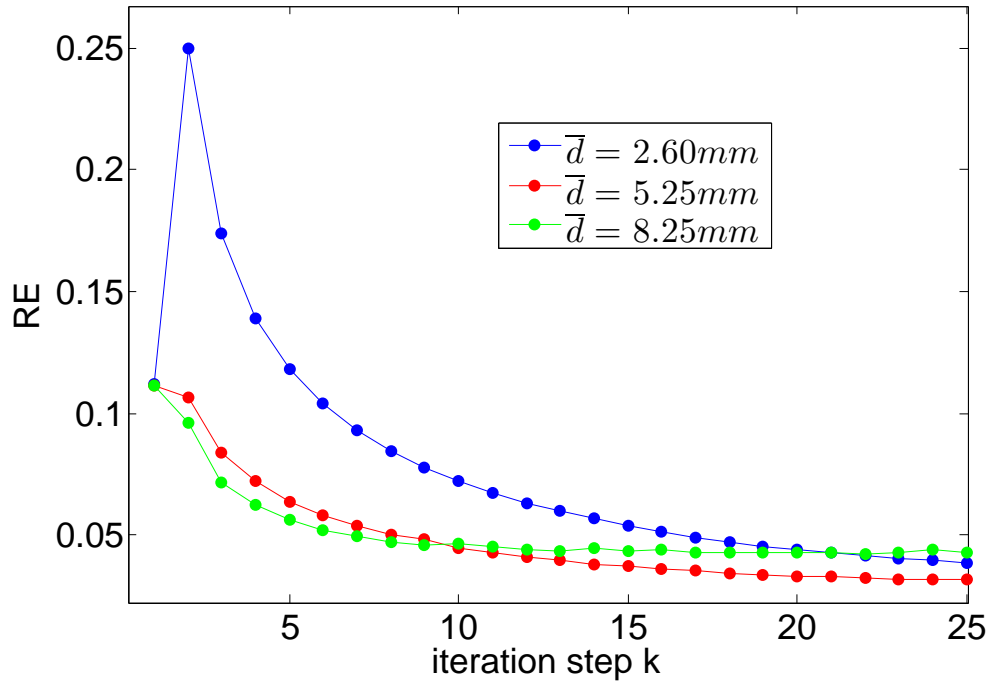


Figure C.5: Tests for the distance \bar{d} to the Z next neighbor voxels in equation (6.9): EKF for pacer location BLW ($SNR = 8.66 \times 10^3$, $\delta t = 4 ms$, $\varepsilon = 0.001$, $Q=0.1$).

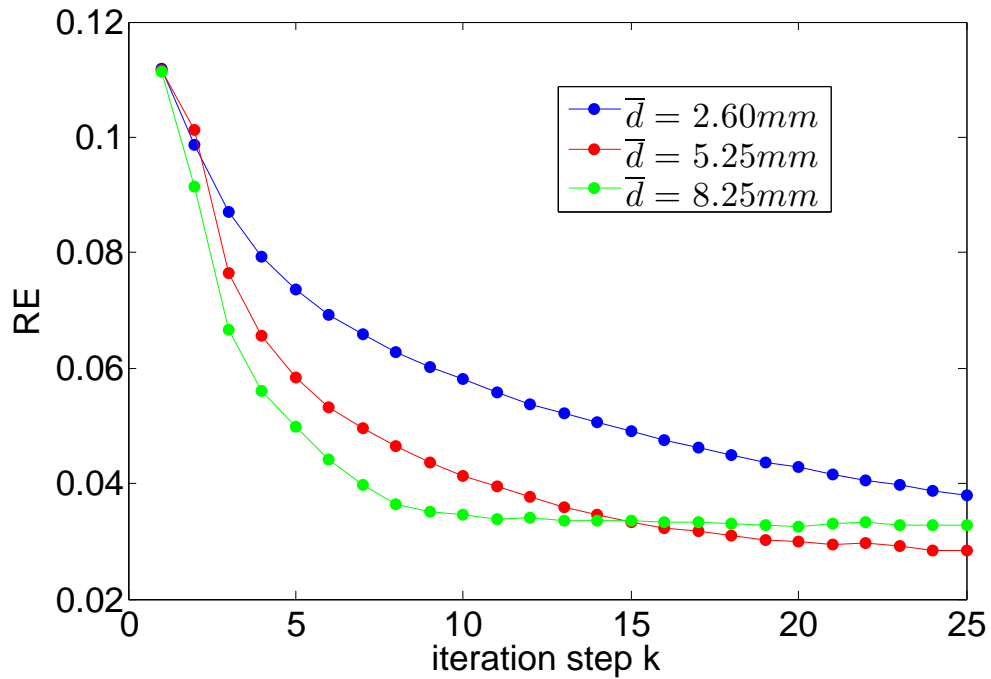


Figure C.6: Tests for the distance \bar{d} to the Z next neighbor voxels in equation (6.9): UKF for pacer location BLW ($SNR = 8.66 \times 10^3$, $\alpha = 2$, $\varepsilon = 0.001$, $Q=1$).

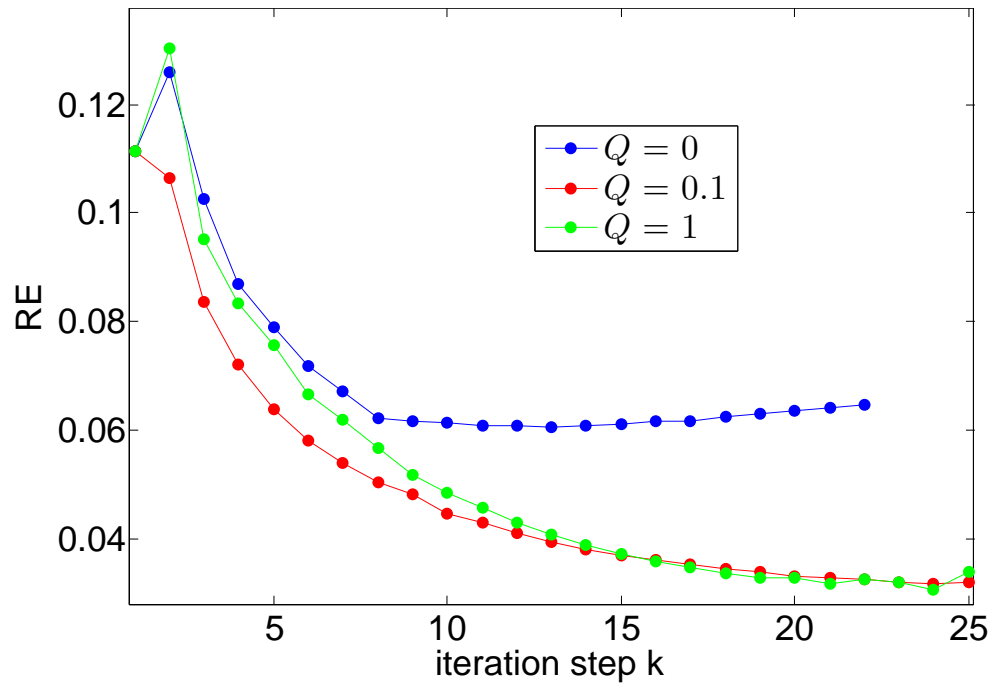


Figure C.7: Tests for the process noise covariance matrix $\mathbf{Q} = Q \cdot \mathbf{I}$ (equation (6.15)): EKF for pacer location BLW ($SNR = 8.66 \times 10^3$, $\delta t = 4 \text{ ms}$, $\bar{d} = 5.25 \text{ mm}$, $\varepsilon = 0.001$).

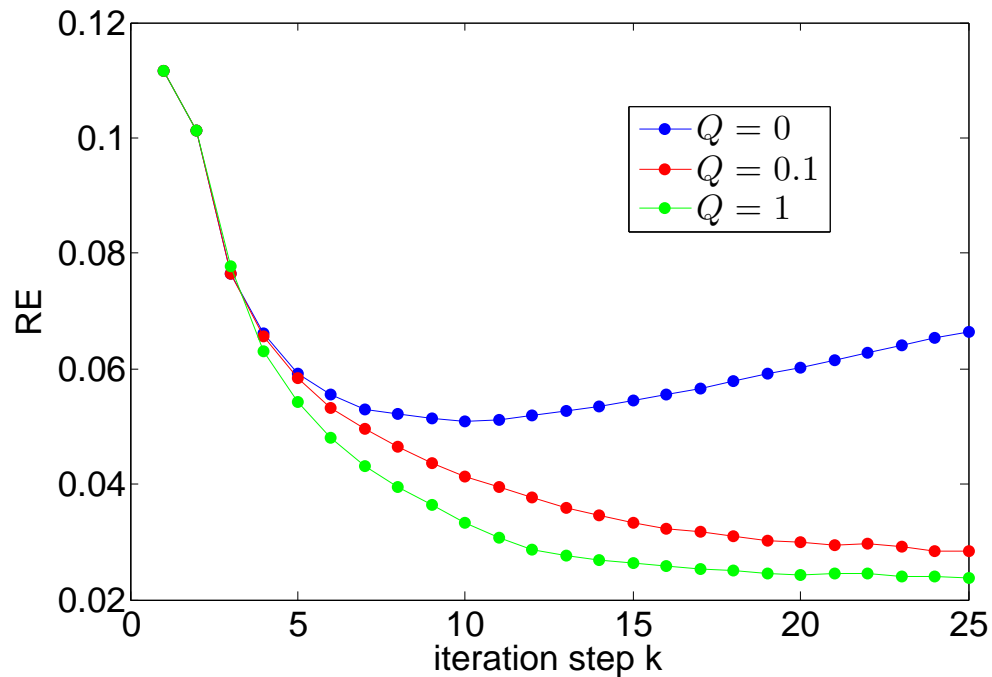


Figure C.8: Tests for the process noise covariance matrix $\mathbf{Q} = Q \cdot \mathbf{I}$ (equation (6.15)): UKF for pacer location BLW ($SNR = 8.66 \times 10^3$, $\alpha = 2$, $\bar{d} = 5.25 \text{ mm}$, $\varepsilon = 0.001$).

Bibliography

- [1] URL <http://www.biomagnetik.de/en/product/cs-mag>, 2013.
- [2] J. Nenonen, C. J. Purcell, B. M. Horacek, G. Stroink, and T. Katila. Magneto-cardiographic Functional Localization Using a Current Dipole in a Realistic Torso. *IEEE T. Bio-Med. Eng.*, 38(7):658–664, 1991.
- [3] J. Kulig and B. A. Koplan. Wolff-Parkinson-White Syndrome and Accessory Pathways. *Circulation*, 122(15):480–483, 2010. doi: 10.1161/CIRCULATIONAHA.109.929372.
- [4] URL <http://www.londonarrhythmiacentre.co.uk/treatments-catheter-ablation-WPW-ablation.html>, 2015.
- [5] L. K. Cheng, J. M. Bodley, and A. J. Pullan. Comparison of Potential- and Activation-Based Formulations for the Inverse Problem of Electrocardiology. *IEEE T. Bio-Med. Eng.*, 50(1), 2003.
- [6] A. Ghodrati, D. H. Brooks, G. Tadmor, and R. S. MacLeod. Wavefront-Based Models for Inverse Electrocardiography. *IEEE T. Bio-Med. Eng.*, 53(9):1821–1831, september 2006.
- [7] T. F. Oostendorp and K. Pesola. Non-invasive determination of the activation sequence of the heart: validation by comparison with invasive human data. *Computers in Cardiology*, 25:313–316, 1998.
- [8] C. Liu and B. He. Noninvasive estimation of global activation sequence using the Extended Kalman Filter. *IEEE T. Bio-Med. Eng.*, 58(3):541–549, 2011.
- [9] E. A. Wan and R. van der Merwe. The Unscented Kalman Filter for nonlinear estimation. *IEEE Adaptive Systems for Signal Processing, Communications and Control Symposium 2000, AS-SPCC*, 2000.
- [10] R. Kandepu, B. Foss, and L. Imsland. Applying the unscented Kalman Filter for nonlinear state estimation. *Journal of Process Control*, 18(7–8):753–768, 2008.
- [11] J. Malmivuo and R. Plonsey. *Bioelectromagnetism - principles and applications of bioelectric and biomagnetic fields*. Oxford University Press, New York, 1995.
- [12] URL <http://commons.wikimedia.org/wiki/User:Yaddah>, 2014.

- [13] D. Durrer, R. Th. van Dam, Freud G. E, M. J. Janse, F. L. Meijler, and R. C. Arzbaecher. Total excitation of the isolated human heart. *Circulation*, 41: 899–912, 1970.
- [14] K. H. W. J. T. Tuschler and A. V. Panfilov. Modelling of ventricular conduction system. *Progress in biophysics and molecular biology*, 96:152–170, 2008.
- [15] T. G. Zhu, C. Patel, S. Martin, X. Quan, Y. Wu, J. F. Burke, M. Chernik, P. R. Kowey, and G. Yan. Ventricular transmural repolarization sequence: its relationship with ventricular relaxation and role in ventricular diastolic function. *European Heart Journal*, 30:372–380, 2009.
- [16] F. H. Netter. *Farbatlantzen der Medizin*, volume 1. Georg Thieme Verlag, 1990.
- [17] D. D. Streeter Jr., H. M. Spotnitz, D. P. Patel Jr., J. Ross, and E. H. Sonnenblick. Fiber orientation in the canine left ventricle during diastole and systole. *Circ. Res.*, 24:339–347, 1969.
- [18] Y. Jiang. *Solving the Inverse Problem of Electrocardiography in a Realistic Environment*. PhD thesis, Karlsruhe Institute of Technology, 2010.
- [19] URL <http://www.ecgsim.org/downloads/other13/downloadgeo.php>, 2014.
- [20] L. Weixue, X. Zhengyao, and F. Yingjie. Microcomputer-based cardiac field simulation model. *Med. Biol. Eng. Comput.*, 31:384–387, 1993.
- [21] A. G. Kleber. The Shape of the Electrical Action-Potential Upstroke. *Circ. Res.*, 97:204–206, 2005.
- [22] B. He, G. Li, and X. Zhang. Noninvasive Imaging of Cardiac Transmembrane Potentials Within Three-Dimensional Myocardium by Means of a Realistic Geometry Anisotropic Heart Model. *IEEE T. Bio-Med. Eng.*, 50(10), October 2003.
- [23] G. R. Li, J. Feng, L. Yue, and M. Carrier. Transmural heterogeneity of action potentials and Ito1 in myocytes isolated from the human right ventricle. *American Journal of Physiology*, 275:369–377, 1998.
- [24] M. V. K. Chari and P. Peter Peet Silvester. *Finite Elements in Electrical and Magnetic Field Problems*. John Wiley & Sons, 1980.
- [25] D. Wang, R. M. Kirby, and C. R. Johnson. Resolution Strategies for the Finite-Element-Based Solution of the ECG Inverse Problem. *IEEE T. Bio-Med. Eng.*, 57(2):220–237, February 2010.
- [26] SimBio Development Group: SimBio: A generic environment for bio-numerical simulations, October 2014. URL <https://www.mrt.uni-jena.de/simbio>.
- [27] C.H. Wolters, H. Koestler, C. Moeller, J. Haerdtlein, L. Grasedyk, and W. Hackbusch. Numerical mathematics of the subtraction approach for the modeling of a current dipole in EEG source reconstruction using finite element head models. *SIAM J. on Scientific Computing*, pages 1–21, 2007.

- [28] C.H. Wolters, H. Koestler, C. Moeller, J. Haerdtlein, and A. Anwander. Numerical approaches for dipole modeling in finite element based source analysis. *International Congress Series, ICS-07008*, 2007.
- [29] M. Schulte, B. Höfl, T. Demming, B. Leithäuser, N. Frey, and J.-W. Park. Measurements with the MCG system CS-MAG of the company Biomagnetik Park, physician's praxis of Dr. Leithäuser, Gorch-Fock-Wall 1, 20354 Hamburg. *UKSH Kiel*, 2013.
- [30] J. C. Mosher, P. S. Lewis, and R. M. Leahy. Multiple Dipole Modeling and Localization from Spatio-Temporal MEG Data. *IEEE T. Bio-Med. Eng.*, 39(6):541–557, June 1992.
- [31] E. W. Cheney and D. R. Kincaid. *Numerical Mathematics and Computing*. Thomson Brooks/Cole, 6 edition, 2008.
- [32] D. Budker and M. Romalis. Optical magnetometry. *Nature Physics*, 3:227–234, 2007.
- [33] B. A. Steinberg, A. Roguin, S. P. III Watkins, P. Hill, D. Fernando, and J. R. Resar. Magnetocardiogram Recordings in a Nonshielded Environment - Reproducibility and Ischemia Detection. *A.N.E.*, 10(2):152–160, april 2005.
- [34] Z. Liu, C. Liu, and B. He. Noninvasive Reconstruction of Three-Dimensional Ventricular Activation Sequence From the Inverse Solution of Distributed Equivalent Current Density. *IEEE T. Med. Imag.*, 25(10), October 2006.
- [35] P. C. Hansen. The discrete Picard condition for discrete ill-posed problems. *BIT*, 30:658–672, 1990.
- [36] R. Grech, T. Cassar, J. Muscat, K. P. Camilieri, S. G. Fabri, M. Zervakis, P. Xanthopoulos, V. Sakkalis, and B. Vanrumste. Review on solving the inverse problem in EEG source analysis. *Journal of NeuroEngineering and Rehabilitation*, 5(25), nov 2008.
- [37] P. C. Hansen. Analysis of discrete ill-posed problems by means of the L-curve. *SIAM Rev.*, 34:561–580, 1992.
- [38] P. Iturralde, M. Guevara-Valdivia, L. Rodriguez-Chavez, A. Medeiros, and L. Colin. Radiofrequency ablation of multiple accessory pathways. *Europace*, 4:273–280, July 2002.
- [39] J. C. Mosher and R. M. Leahy. Recursive MUSIC: A framework for EEG and MEG Source Localization. *IEEE T. Bio-Med. Eng.*, 45(11):1342–1354, 1998.
- [40] S. J. Julier and J. K. Uhlmann. Unscented filtering and nonlinear estimation. *Proceedings of the IEEE*, 92(3):401–422, March 2004.
- [41] M. S. Grewal and A. P. Andrews. *Kalman Filtering Theory and Practice Using MATLAB*, volume 2. New York: Wiley, 2001.

- [42] URL http://www.academia.edu/1512888/Introduction_to_the_Kalman_Filter_and_its_Derivation, 2012.
- [43] J. J. Jr. LaViola. Comparison of Unscented and Extended Kalman Filtering for Estimating Quaternion Motion. *P. Amer. Contr. Conf.*, 3:2435–2440, 2003.
- [44] M. Rhudy, Y. Gu, J. Gross, and M. R. Napolitano. Evaluation of Matrix Square Root Operations for UKF within a UAV GPS/INS Sensor Fusion Application. *International Journal of Navigation and Observation*, 2011. doi: 10.1155/2011.
- [45] A. G. Kleber, M. J. Janse, F. J. Wilms-Schopmann, A. A. Wilde, and R. Coronel. Changes in conduction velocity during acute ischemia in ventricular myocardium of the isolated porcine heart. *Circulation*, 73:189–198, 1986.
- [46] M. St-Pierre and D. Gingras. Comparison between the unscented Kalman filter and the extended Kalman filter for the position estimation module of an integrated navigation information system . *IEEE Intelligent Vehicles Symposium*, pages 831–835, June 2004.
- [47] A. P. Dempster, N. M. Laird, and D. B. Rubin. Maximum Likelihood from Incomplete Data via the EM Algorithm. *J. R. Stat. Soc. Ser. B (Methodological)*, 39(1):1–38, 1977.
- [48] J. Chandrasekar, I.S. Kim, A.J. Ridley, and D.S. Bernstein. Reduced-Order Covariance-Based Unscented Kalman Filtering with Complementary Steady-State Correlation. *IEEE Proceedings of the 2007 American Control Conference*, pages 4452–4457, july 2007.
- [49] A.C. Charalampidis and G.P. Papavassilopoulos. Computationally Efficient Kalman Filtering for a Class of Nonlinear Systems. *IEEE Transactions on Automatic Control*, 56(3):483–491, march 2011.
- [50] A. Gocht. *Die zylindrische Multipolentwicklung und ihre Anwendung bei der Magnetokardiographie*. Master Thesis, University of Kiel, 2014.
- [51] S. Taulu and M. Kajola. Presentation of electromagnetic multichannel data: The signal space separation method. *Journal of applied physics*, 97, june 2005.
- [52] J-W Park and F. Jung. Qualitative and Quantitative Description of Myocardial Ischemia by means of Magnetocardiography. *Biomed. Technik*, 49:266–272, 2004.

Lebenslauf

Persönliche Daten

Name: Henning Ahrens
Familienstand: ledig
Geburtstag: 07.12.1984
Geburtsort: Eckernförde
Staatsangehörigkeit: deutsch

Berufserfahrung

03/2011–12/2014 Wissenschaftlicher Mitarbeiter am Institut für Elektrotechnik und Informationstechnik der Christian-Albrechts-Universität zu Kiel, Lehrstuhl Prof. Dr.-Ing. Ludger Klinkenbusch, Numerische Feldberechnung

Ausbildung

10/2005–01/2011 Diplom-Physik-Studium an der Christian-Albrechts-Universität zu Kiel, Anzahl der Studiensemester: 11
10/2004–08/2005 Zivildienst im Kindergarten Domänental Kiel-Kronshagen
08/1995–08/2004 Gymnasium Max-Planck-Schule Kiel

Erklärung

Hiermit versichere ich, dass ich die vorliegende Dissertation

The inverse problem of Magnetocardiography

Activation time imaging with the Extended Kalman Filter and the Unscented Kalman Filter

selbstständig und ohne unzulässige fremde Hilfe angefertigt habe und dass ich alle von anderen Autoren wörtlich übernommenen Stellen wie auch die sich an die Gedankengänge anderer Autoren eng anlehnenden Ausführungen meiner Arbeit besonders gekennzeichnet und die entsprechenden Quellen angegeben habe. Weiterhin wurde die Arbeit bisher nicht im Rahmen eines Prüfungsverfahrens vorgelegt, jedoch wurden Teile in Form von Beiträgen in Fachzeitschriften und Tagungsbänden veröffentlicht, sowie auf Konferenzen präsentiert. Diese Arbeit ist unter Einhaltung der Regeln guter wissenschaftlicher Praxis der Deutschen Forschungsgemeinschaft entstanden.

Ort

Datum

Unterschrift